Formation mechanisms of heterostructures and polytypes in III-V nanowires

Giacomo Priante

Université Pierre et Marie Curie

Ecole doctorale 397

Formation mechanisms of heterostructures and polytypes in III-V nanowires

Présentée par Giacomo PRIANTE

Thèse de doctorat de Physique

Présentée et soutenue publiquement le 21 Octobre 2016

Devant un jury composé de :

Lucia SORBA Directrice de recherche CNR, NEST et SNS (Pise, Italie)	Rapporteure
Joël CIBERT Directeur de recherche CNRS, Institut Néel	Rapporteur
Vladimir G. DUBROVSKII Professeur, SPAU, ITMO et Institut Ioffe (Saint-Pétersbourg, Russie)	Examinateur
Jean-Noël AQUA Maître de conférences HDR, UPMC et INP	Examinateur
Sébastien PLISSARD Chargé de recherches CNRS, LAAS	Examinateur
Frank GLAS Directeur de recherche CNRS, C2N	Directeur de thèse
Jean-Christophe HARMAND Directeur de recherche CNRS, C2N	Co-directeur de thèse membre invité

Formation mechanisms of heterostructures and polytypes in III-V nanowires

Giacomo Priante

Friday 18th November, 2016

A Martina, per quel che abbiamo fatto e per quel che faremo.
Orsay, Francia, Ottobre 2016

Acknowledgements

Alles hat ein Ende, nur die Wurst hat zwei. These three years I have spent as a PhD student, at the LPN, have been filled with many new experiences and learning moments that I will carry with me forever. I am very grateful to my supervisor Frank Glas and my co-supervisor Jean-Christophe Harmand for a list of reasons that is too long to fit into this page: thank you! I thank each single member of the thesis committee for the time and effort spent in evaluating my work: the referees Joël Cibert and Lucia Sorba, the examiners Vladimir G. Dubrovskii, Jean-Noël Aqua and Sébastien Plissard.

Clearly, in today's science it is just impossible to work alone: I thank all my ELPHYSE colleagues for their help, in particular Gilles Patriarche for the spectacular TEM images on which this work is largely based.

I wish to thank Dagou Zeze and Andrew J. Gallant from Durham University for creating the NanoEmbrace network, which has been a fantastic experience. I acknowledge the financial support from the European Union's 7th Framework Programme, without which none of this would have been possible. I wish all the best to my fellow colleagues in the network, in particular to Andrés Aldana, for all the *soft skills* training we had.

I would like to thank the people with whom I moved my first steps in the world of molecular beam epitaxy and nanowires: Silvia Rubini and Faustino Martelli. Working together for over one year in Trieste has been an invaluable opportunity. I also thank Stefano "Filo Extremo" Ambrosini for having shown me how to take a farmer's approach to nanowire growth.

The continued moral support of my family and friends cannot be overstated, I am very lucky. Finally, I wish good luck to all the people (present and past) of the lunch and fun group: Vishnu Kumaresan, Théo Jegorel, Nicolas Jamond, Vivek Panapakkam, Juan "El Presidente" Castro, Dimitris "Sexy" Kazasis, Carme Gomez, Konstantinos Papatryfonos, Vincent Brac, Quentin Gaimard, Cosimo Calo, Andrea Scaccabarozzi, Konstantinos Pantzas, Niccolò Somaschi, Carlos Anton, Jonathan Lee, Valerio Piazza, Lu Lu... and all the others I forgot to mention.

Thesis overview

This thesis, as a *partial fulfillment* of the requirements for the doctoral degree, condenses two years and a half of the author's scientific activity at the LPN (now C2N) in Marcoussis, France. The main objective of the present work is to deepen the knowledge of some fundamental mechanisms of nanowire growth, a topic to which our group has largely contributed in the past and still does today.

Semiconductor nanowires (NWs) are structures with a diameter less than 100 nm and unconstrained length, and are nowadays fabricated from a wide variety of materials and methods. Thanks to their reduced footprint, NWs have less stringent requirements of lattice matching as compared to thin films. This opens the way for new material combinations and allows for the monolithic integration of high-performance III-V semiconductors on silicon. In the last decade, substantial progress has been made in controlling and understanding of III-V NW growth. However, the remarkable properties of the NWs cannot be fully exploited if some critical aspects are not addressed. Specifically, it is important to understand which factors influence the crystal structure, which is often found to be different from that of the bulk and sometimes even a more or less random mixture. A mixed crystal phase is extremely detrimental for the electronic properties of the NWs. The other important point is to control interface abruptness in axial heterostructures, which is pivotal for the fabrication of many useful structures (quantum wells, superlattices, etc.).

In this thesis, a number of novel results on crystal phase selection and the formation of axial heterostructures are presented. Whenever possible, the experiments have been accompanied with quantitative modeling, allowing for the identification of key parameters. The manuscript is structured as follows. In **Chapter 1**, we introduce the growth of III-V NWs, starting from the definition of what a NW is and how NWs are formed via the vapor-liquid-solid mechanism. We highlight the role of nucleation in determining growth rates and crystal phase selection. We introduce the self-catalyzed GaAs NWs, a particularly interesting system that will be used extensively for our investigations. We review the interest, advantages and disadvantages of NW heterostructures, emphasizing that the liquid droplet assisting the growth may (severely) limit interface abruptness in axial heterostructures. In **Chapter 2**, we

describe the technique used in this work to grow NWs, Molecular Beam Epitaxy (MBE) and those used for NW characterization. We discuss how the NW composition can be measured with monolayer resolution. Thanks to high-resolution transmission electron microscopy, in **Chapter 3** we study the stacking sequence of InP NWs with mixed crystal phase, finding spatial correlations which we describe in terms of conditional probabilities. Our probabilistic treatment is combined with nucleation theory to build a quantitative model of inter-layer interactions. This reveals the role of the nucleus edge at conveying the interaction. In **Chapter 4** we demonstrate that is possible to obtain self-catalyzed GaP NWs using growth conditions compatible with those of self-catalyzed GaAs NWs. This result is exploited to fabricate ternary and quasi-binary GaP/GaAs/GaP axial heterostructures with sharp interfaces. The compositional profiles of interfaces are analyzed and the experimental difficulties specific to MBE are discussed. In **Chapter 5** we study the growth of heterostructured self-catalyzed GaAs nanowires using another group III metal, Al. Such mixed group III heterostructures are generally assumed to produce broader interfaces than those obtained using group V elements. We show that the interfaces are surprisingly sharp, about ten times sharper than for similar gold-catalyzed NWs. We formulate a quantitative model which is able to reproduce the composition of each single interfacial monolayer. Finally, in **Chapter 6** we try to answer new questions that arise in light of the results of the preceding chapters. The growth of thin, self-catalyzed GaAs and GaP NWs is attempted, and we show that it is possible to obtain NW diameters in the 20 nm range without any substrate preparation procedure. Moreover, making use of numerical simulations, we investigate growth conditions that can reduce the stochastic character of nucleation, hence improving thickness control. The possibility of achieving controlled growth of single monolayers is discussed.

Table of contents

List of figures

List of tables

Chapter 1

Vapor-liquid-solid growth of III-V nanowires

The aim of this chapter is to provide a general introduction to the topic of III-V nanowires growth by the vapor-liquid-solid method. Special attention will be paid to growth mechanisms, elucidating what are the driving forces for nanowire growth, how growth rates are affected by the growth parameters and what influences crystal phase selection. We will review the advantages and disadvantages of nanowires for heteroepitaxy. A vast literature on each of these subjects is available, but we will limit our discussion to the concepts necessary for the developments presented in the next chapters.

1.1 What are nanowires?

At the time of writing this manuscript, research on nanowires has been going on for some 20 years. Nowadays, the field has reached a good degree of maturity and nanowires are fabricated out of a wide range of materials (metals, semiconductors, insulators, oxides, etc.). Devices having nanowires as key components have been demonstrated as well, especially in photonics [34, 69, 76], transistors [17, 56, 138], batteries [20, 77] and other applications such as chemical sensing [141]. However, despite these remarkable demonstrations, the "killer application" of nanowires is still lacking. Before discussing the advantages and disadvantages of nanowires, let us define what a nanowire is.

Definition. Nanowires (NWs) are quasi-unidimensional structures, having a diameter less than $\approx$100 nm and an unconstrained length.

Note that this definition refers only to their shape and size, and says nothing about their internal structure or the way they are obtained. In fact, it is indeed their geometry

that makes them special, in particular their high surface/volume ratio and the possibility of having diameters small enough for quantum effects to become important. The fabrication of structures of high aspect ratio *and* small diameters is not an easy task, and two complementary approaches are employed: the top-down approach, in which the starting bulk material is masked and selectively etched, leaving behind the desired nanostructures; the bottom-up approach, where the constituents of the NWs are supplied in conditions which are suitable for the NW to self-assemble.

The top-down approach has the advantage to allow one to precisely define the size and position of the desired NWs. However, the chosen lithographic technique may limit the smallest achievable NW diameter, and anisotropic etching may limit the aspect ratio. Although the control of positions and sizes is generally harder to achieve compared to top-down methods, the bottom-up approach offers a higher number of possibilities. For example, it allows one to fabricate high-quality complex structures with alternating compositions by changing the materials supplied during NW growth. This could be difficult to realize by the top-down approach, because such high-quality structure may not exist in "bulk" form (*i.e.* as 2D layered structure), in particular if they involve lattice-mismatched materials. This is especially true for semiconductors where high material quality is essential to ensure optimal opto-electronic properties. For this reason, the bottom-up (or self-assembly) of semiconductor NWs is of particular interest, and the rest of the discussion will be restricted to this class of materials.

From an historical point of view, NWs are not a recent discovery. Wagner [139] reported the formation of crystalline structures of high aspect ratio by the vapor-liquid-solid method (VLS, which will be discuss in the next section) of several semiconducting materials during the 1960s. Due to their micrometric size and by analogy with their metallic counterparts, these structures were commonly referred to as *whiskers*. The theoretical basis of VLS growth was developed during the 1970s by Givarzov [47], who identified the fundamental mechanisms of whisker growth. However, it is not before the 1990s that very thin structures of GaAs and InAs (diameters between 15 and 40 nm) were realized at Hitachi by Hiruma and coworkers [66], who also demonstrated the growth of p-n junctions in NWs and their ability to emit light. By the end of that decade, demonstrations of NW growth of elemental and compound semiconductors by the Lieber's group [35] showed that the VLS mechanism is indeed a general growth technique and research on VLS-grown NWs took off. In the next sections, we are going to describe how the VLS mechanism works and what are the properties of the so-obtained NWs.

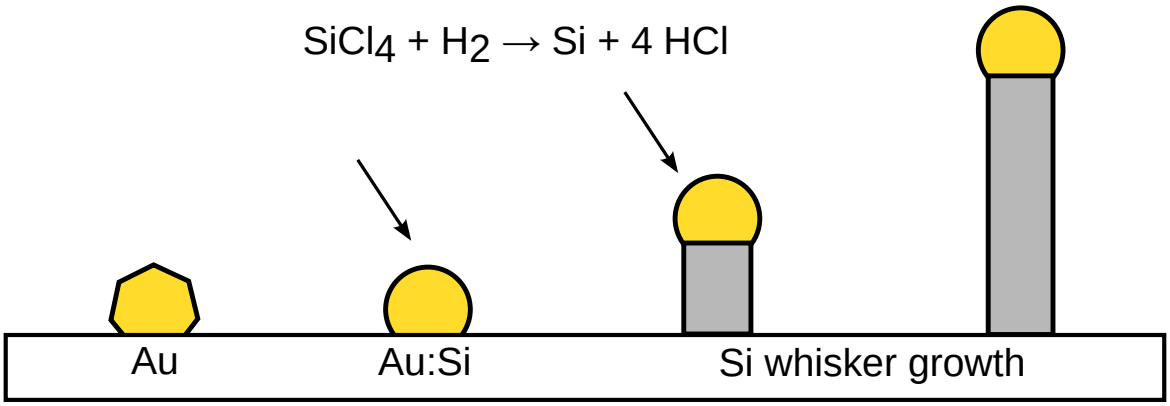

Fig. 1.1 Schematic representation of the VLS mechanism as originally proposed by Wagner and Ellis [140].

1.2 The vapor-liquid-solid mechanism of nanowire growth

The VLS mechanism was proposed by Wagner and Ellis in 1964 [140] to explain the growth of single-crystal silicon whiskers on Si (111), with diameters from 100 nm to hundreds of microns. Whisker growth was performed in a chemical vapor deposition reactor after the deposition of a thin film of gold followed by an annealing step at 950 °C. During the annealing step, Si from the substrate mixes with Au to form Au:Si droplets (Fig. 1.1). The Au-Si alloy has an eutectic point located at 363 °C for a Si atomic fraction of 18.6%. Therefore, the alloy may be liquid at temperatures considerably lower than the melting point of the constituents (Si: 1414 °C, Au: 1064 °C) and is liquid at standard growth temperatures.

Upon exposure to the gaseous reactants $SiCl_4$ and H_2, the liquid droplet becomes supersaturated with Si atoms. This is possible, despite the low temperature, because the decomposition reaction is catalyzed by the gold droplet. For this reason, the droplet is referred to as the *catalyst*, and NWs obtained by the VLS method are often called metal-*catalyzed* or *catalyst-assisted*. This terminology is retained even when no chemical catalysis occurs, as in the case of molecular beam epitaxy (MBE). In MBE, the NW constituents are supplied in their elemental form and no complex precursors are used: the droplet acts as a collector and reservoir of material, which thus may be seen as a "physical" catalyst, in the sense that solid phase condensation via the droplet is more favorable than direct vapor-solid deposition.

Sustained supersaturation in the droplet causes the continuous precipitation of Si at the solid-liquid interface, which results in the elongation of the whisker (or NW). The droplet

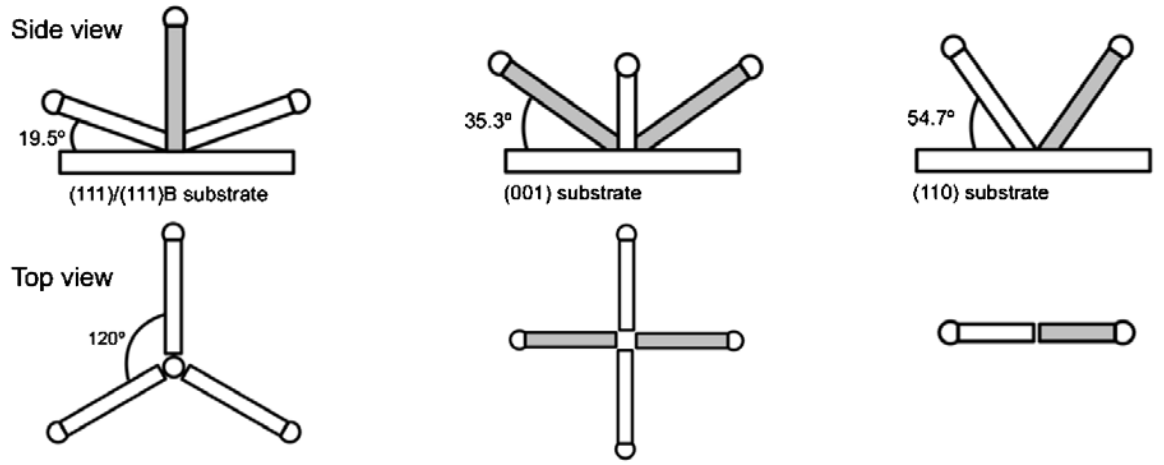

Fig. 1.2 Orientations of III-V NWs growing along the <111> direction on common low-index substrates. Shaded NWs indicate the <111>B direction and non-shaded NWs indicate the <111>A direction. Adapted from Ref. [44]

sticks to the NW top, where it is eventually found after the end of the growth. Since growth occurs at the liquid-solid interface, the droplet size determines the diameter of the NW.[1]

1.2.1 Growth directions

Broadly speaking, NWs grow along the direction that minimizes the total free energy. The total free energy is the sum of the bulk contribution, of the catalyst-vapor interface energy, the catalyst-NW interface energy and the vapor-NW interface energy, the latter two depending on the crystalline orientation of the interfaces. At the formation of the first NW monolayer, the dominant contribution is represented by the catalyst-NW interface energy. For III-V materials with cubic crystal structure, (111)B facets have the lowest surface free energy, while for III-Vs with hexagonal structure the lowest free energy is that of the (0001) surface [44]. As a result, cubic and hexagonal NWs grow preferentially along the <111>B and <0001> directions, respectively.[2] Hence, when NWs are grown on a crystalline substrate, the NW orientation with respect to it will depend on the crystal orientation, as sketched in Fig. 1.2.

If a (111)B substrate is used, III-V NWs will grow vertically. Verticality is generally desirable for integration, as it makes it easier to process and contact the NWs with conventional fabrication methods. On the other hand, if the substrate is a (111)-oriented elemental

[1] Note that this is not the same as the initial droplet size. The droplet may slightly inflate or deflate as Si is added or removed. Moreover, a droplet sitting on the substrate and a droplet at the top of the NW have generally different contact angles, which implies different sizes of the liquid-solid interface at constant droplet volume.

[2] Nevertheless, growth conditions and strain may alter this preference.

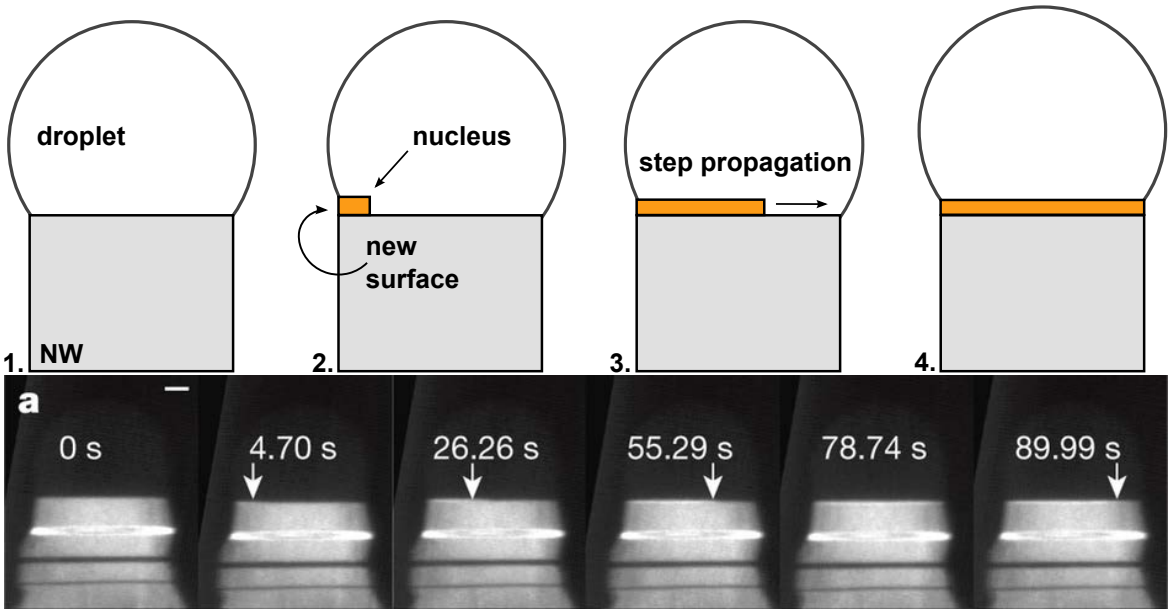

Fig. 1.3 Schematic representation of the layer-by-layer mechanism of NW growth. A supersaturated dropet sits on top of the NW (1); nucleation occurs preferentially at the triple phase line (2), as the cost of creating a new surface there may be lower compared to the case in which the nucleus is completely sourrounded by the liquid; after nucleation, the step propagates quickly to complete the monolayer; after monolayer completion, the cycle repeats (4). Bottom panel: in situ TEM experiment showing the step flow in a wurtzite gold-catalyzed GaAs NW, adapted from Ref. [73].

semiconductor, *e.g.* Si(111), NWs can grow along any of the the four equivalent <111> directions, as there is no <111>B direction (Fig. 1.2).

1.2.2 Nanowire growth dynamics

NW growth under the droplet is generally assumed to occur in a layer-by-layer fashion mediated by the formation of a 2D nucleus, as schematized in Fig. 1.3. The nucleus is assumed to form preferentially at the vapor-liquid-solid boundary (this point will be detailed in the next sections). Once the nucleus is formed, it rapidly expands to fill the whole monolayer.

This mechanism has been verified experimentally in *in situ* chemical vapor deposition studies: growth occurs inside a transmission electron microscope (TEM), which allows one to watch the NWs as they grow.[3] Direct observation of step propagation has been reported in

[3] However, due to technical limitations of electron microscopes, the precursors pressure are much lower than those employed in typical NW growth experiments.

Si NWs, both for VLS and vapor-solid-solid (VSS) growth modes [67, 143] and very recently for VLS GaAs NWs [73].

In this scheme, the elongation rate will be given by nucleation rate, which in turn is set by the temperature and by the thermodynamic force for solidification, which is the difference of chemical potentials between the species in the liquid and in the solid, $\Delta\mu_{LS} > 0$. Clearly, there should be a driving force to fill the droplet as well, so that $\Delta\mu_{VL} > 0$. In some cases, filling of the droplet also occurs by surface diffusion of the species adsorbed on the NW sidewalls.

The actual morphology of VLS-grown NWs will depend on the competition between axial and radial growth rate, the latter being a vapor-solid process, without any involvement of the droplet. A variety of competing processes are possible: the impinging species can be directly absorbed into the droplet, desorb, or diffuse out of it; atoms impinging on the substrate may re-evaporate, or diffuse to be eventually incorporated on the substrate itself, leading to the formation of a parasitic layer. Alternatively, they can diffuse to be incorporated into the NW sidewalls or into the NW via the droplet. All these processes make it impossible to construct a unified model of NW growth based on purely thermodynamic considerations, and growth kinetics must be taken into account in each specific case.

1.3 Understanding NW growth with nucleation theory

We have seen that NW growth is described as the addition of individual monolayers. This occurs in a cyclic fashion and is limited by nucleation on the NW top surface. In order to understand which factors influence the rate at which the nuclei appear we need a theory of nucleation. However, the problem is not an easy one and nucleation theory is still an active field of research. Our discussion will be limited to the essential concepts of classical nucleation theory, presenting some formulas that will be used later in this work.

1.3.1 Calculation of the 2D nucleation barrier

Imagine having a perfectly flat surface surrounded by a supersaturated environment and let $\Delta\mu$ be the difference of chemical potential between the liquid and solid. The nucleation process can be seen as the spontaneous (random) aggregation of the supersaturated species to form a cluster. The stability of this cluster is determined by the ability of the thermodynamic force for solidification $\Delta\mu$ to overcome the energy cost of creating a new surface bounding the cluster.

We want to evaluate the energy barrier for the formation of a nucleus sitting on the top (111)B facet of a III-V nanowire. The height of the barrier is given by the maximum work needed to form the nucleus. The work ΔG is the sum of the energy cost of forming the nucleus surface and edges, minus the gain due to the thermodynamic drive for solidification $\Delta\mu$ and to the destruction of the nucleus-NW interface. We suppose that the nucleus has the shape of an equilateral triangle of side length l. This is justified by the fact that nuclei on (111) surfaces have such shape. Other shapes are possible, affecting the final result only for a geometric pre-factor. Here we are taking the surface energies of the cluster to be the same as the surface energies of the equivalent macroscopic surfaces, an approach known as the *capillary approximation*. Introducing σ and Γ, with σ the energy cost per unit area of replacing the substrate surface with the nucleus top surface and Γ the energy cost per unit length of creating the nucleus edge, we write:

$$\Delta G = -Ah\Delta\mu + A\sigma + 3lh\Gamma \tag{1.1}$$

where $A = \frac{\sqrt{3}}{4}l^2$ and h are the area and height of the nucleus, respectively. Note that $\sigma = 0$ if the substrate and nucleus top are of the same nature (*e.g.* in the case of homoepitaxy).

The sum of these volume and surface terms results in ΔG to be a concave function of l with a maximum ΔG^* for some l^*, which is known as the *critical size* of the nucleus (Fig. 1.4a). Nuclei with a size smaller than the critical one will dissolve and nuclei bigger than the critical size will grow indefinitely.

Since ΔG is concave for all values of l, the maximum is located where $\partial\Delta G/\partial l = 0$:

$$\frac{\partial\Delta G}{\partial l}\Big|_{l=l^*} = \frac{\partial}{\partial l}\Big|_{l=l^*}[\frac{\sqrt{3}}{4}l^2(\sigma - h\Delta\mu) + 3lh\Gamma] = \frac{\sqrt{3}}{2}l^*(\sigma - h\Delta\mu) + 3h\Gamma = 0 \tag{1.2}$$

which yields the critical size l^*:

$$l^* = 2\sqrt{3}\frac{h\Gamma}{h\Delta\mu - \sigma} \tag{1.3}$$

Substituting into Eq. 1.1, we get the corresponding critical energy ΔG^*:

$$\Delta G^* = 3\sqrt{3}h\frac{\Gamma^2}{\Delta\mu - \sigma/h} \tag{1.4}$$

This expression will be useful in the next sections to understand where the nucleation takes place and why different crystal phases are observed in VLS-grown III-V NWs.

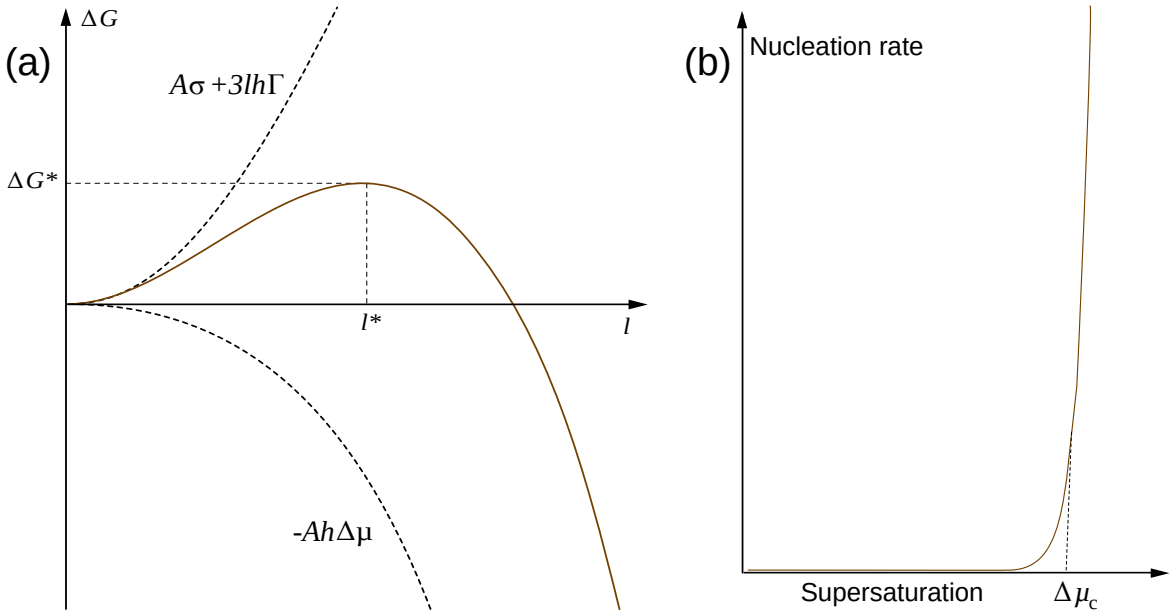

Fig. 1.4 a) Free energy change ΔG as function of the nucleus size l (continuous line), which is the sum of the volume and surface terms (dashed lines). b) Qualitative dependence of the nucleation rate as function of the supersaturation $\Delta\mu$: the nucleation rate is practically zero until a critical value of supersaturation $\Delta\mu_c$ is reached, increasing steeply afterwards. Adapted from Ref. [93].

1.3.2 The classical nucleation rate

According to Ref. [92] the classical nucleation rate (per unit area) is given by:

$$J_0 = \omega^* Z N_0 \exp\left(-\frac{\Delta G^*}{k_B T}\right) \tag{1.5}$$

where ω^* is the atoms attachment frequency to the nucleus and N_0 is the density of adsorption sites. $Z = (\Delta G^*/3\pi k_B T i^{*2})^{1/2}$, where i^* is the the number of atoms in the critical nucleus, is referred to as the Zeldovich factor. However, the main dependence of J_0 on the supersaturation is in the exponential term, with the Zeldovich factor changing very slowly compared to it. The consequence is remarkable and reflects a characteristic feature of nucleation: when the supersaturation $\Delta\mu$ is lower than some critical $\Delta\mu_c$, pretty much nothing happens (Fig. 1.4b). As we approach $\Delta\mu_c$, the nucleation rate increases abruptly by many orders of magnitude. In fact, nucleation on a perfect crystalline surface can take extremely long to happen for typical values of ΔG and $k_B T$ [29]. For nucleation events to happen in a laboratory time scale $\Delta G/k_B T$ should be no larger than ≈ 30 [93]. On a macroscopic surface, steps and defects are always present and growth proceeds by simple attachment of the adatoms (although nucleation on terraces can still occur under certain growth conditions). On the other hand,

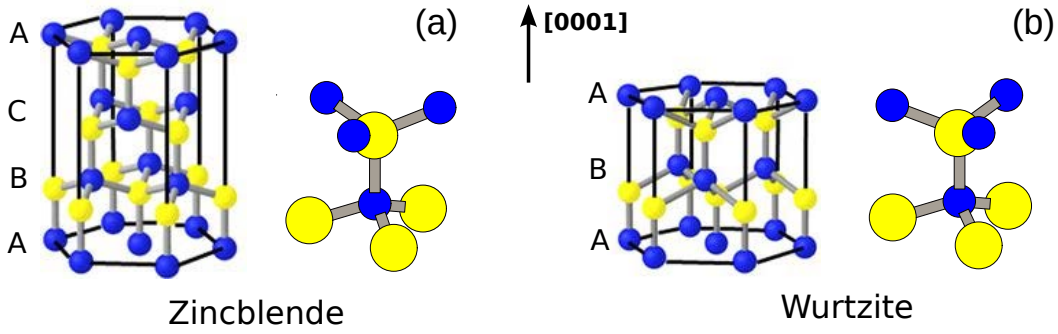

Fig. 1.5 ZB and WZ structures, distinguished by the lateral position of the atoms along the [0001] direction or by the relative orientation of III-V bonds. a) ZB structure represented with an hexagonal cell; b) WZ structure.

because of its size, the NW top surface is indeed a perfect one, and nucleation plays a dominant role.

1.3.3 Polytypism in III-V nanowires

Bulk III-V semiconductors crystallize in the cubic zincblende (ZB) form, except for nitrides, which adopt the hexagonal wurtzite (WZ) structure. Along the <111> direction (which is also the typical NW growth direction), the two structures differ only for the stacking sequence, the ZB sequence being ABCABCA... and the WZ being ABABA..., where each letter indexes one of the three possible lateral positions of the ML (Fig. 1.5). Alternatively, the two structures can be distinguished by the relative orientations of the III-V bonds. In the ZB structure the III-V bonds are parallel to each other, while in WZ they are arranged in a staggered configuration (using the language of chemistry, we would say that they are in "trans" and "cis" configuration, respectively).

Interestingly, materials that are ZB in their bulk form are often found to crystallize as WZ in NWs. This behavior has been observed in a number of III-V materials grown by different techniques, especially in arsenides [62, 99, 112, 113, 125, 128, 135]. For many III-V materials the energy difference between the two crystal structures is only a few meV/atom [146], and theoretical calculations predict that the WZ structure is thermodynamically favorable for very thin NWs (diameters <10 nm) because of the lower number of dangling bonds on the NW sidewalls and edges compared to ZB [1, 46, 90]. However, this cannot explain the observation of the WZ phase in the works cited above, where the diameters are much larger.

Besides being interesting *per se*, understanding what drives crystal phase selection is pivotal for possible NW applications, since a mixed crystal phase degrades the electronic

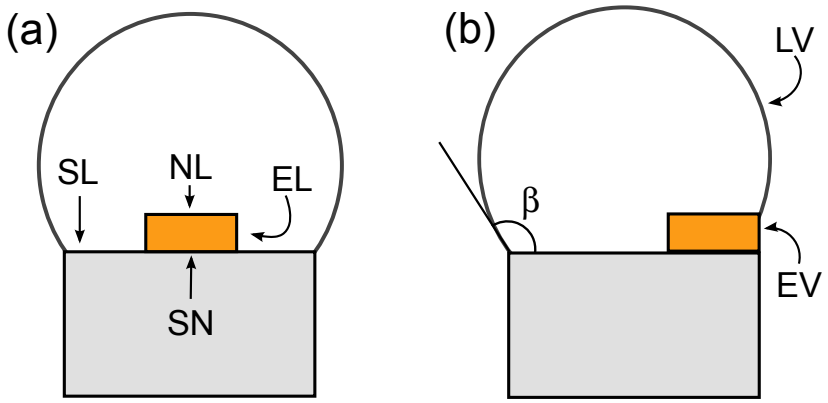

Fig. 1.6 a) Nucleation away from the TPL; b) Nucleation at the TPL. Arrows indicate the relevant interfaces: SN for solid-nucleus, NL for nucleus-liquid, SL for solid-liquid, LV for liquid-vapor and EL and EV the nucleus edge with liquid and vapor, respectively. β is the droplet contact angle.

properties of the NW significantly [137]. On the other hand, since the crystal structure affects the electronic structure, control of the former opens the way for new developments. For example, WZ GaAs has been predicted to have a direct band gap slightly larger than ZB, the two giving a type II band alignment [13], as demonstrated experimentally in a GaAs *crystal phase heterostructure* [129]. Another possibility is that a material with indirect band gap in ZB form becomes direct band gap in WZ form, which is the case of GaP for example [9].

An explanation of why the WZ phase is often found in NW of materials which are normally ZB was given by Glas and coworkers [52], of which we summarize here only the main points. Given that growth occurs in a layer-by-layer fashion limited by nucleation, if the formation of each layer is mediated by only one nucleus (this is called the *mononuclear regime*), then the relative orientation of the new layer with respect to the preceding one will be determined by the orientation of the nucleus (ZB or WZ). Therefore, to obtain a pure ZB or WZ phase, all nuclei must form in either ZB or WZ position (orientation) with respect to the previous one.

With reference to Fig. 1.6, we assign a surface energy γ to each of the relevant interfaces. Let us consider the case in which nucleation occurs away from the triple-phase line (TPL) (Fig. 1.6a). Given that the atomic structure of a single layer does not depend on its position (ZB or WZ), all the interface energies are the same in both configurations, except for the nucleus-solid energy (marked as SN in Fig. 1.6). The nucleus-solid energy will be zero for nucleation in ZB position and will be some $\gamma_F > 0$ (the cost of creating a stacking fault) for nucleation in WZ position. Therefore, the difference in free energy change (Eq. 1.1) between the two cases is $\Delta G^{WZ} - \Delta G^{ZB} = A\gamma_F > 0$ and nucleation away from the TPL always favors ZB nucleation.

Let us now consider nucleation at TPL (Fig. 1.6b). According to the authors of Ref. [52], nucleation occurs at the TPL provided that:

$$\gamma_{EV} - \gamma_{EL} - \gamma_{LV} \sin\beta < 0 \tag{1.6}$$

where β is the droplet contact angle. The condition expressed by Eq. 1.6 is typically satisfied in gold-catalyzed NWs. At the TPL the situation is different from nucleation at the center, because creation of the nucleus-vapor interface has eliminated some of the liquid-vapor interface. A portion x of the nucleus perimeter is in contact with the vapor, therefore the total edge energy of the nucleus is reduced by a factor $x\gamma_{LV}\sin\beta$ and the total edge energy of the nucleus will be [52]:

$$\Gamma_i = (1-x)\gamma_{EL} + x(\gamma_{EV,i} - \gamma_{LV}\sin\beta) \tag{1.7}$$

where i can be ZB or WZ, as the edge energy of the nucleus in contact with the vapor is different for the two nucleus positions [52]. From this, we can derive a criterion for WZ formation at the TPL. Let us write the nucleation barrier (Eq. 1.4) for WZ and ZB positions:

$$\Delta G^*_{WZ} \propto \frac{\Gamma^2_{WZ}}{\Delta\mu - \gamma_F/h}, \Delta G^*_{ZB} \propto \frac{\Gamma^2_{ZB}}{\Delta\mu} \tag{1.8}$$

WZ nucleation is favored if $\Delta G^*_{WZ} < \Delta G^*_{ZB}$, which requires $\gamma_{EV,WZ} < \gamma_{EV,ZB}$ and:

$$\Delta\mu > \frac{1}{1 - \left(\frac{\Gamma_{WZ}}{\Gamma_{ZB}}\right)^2} \frac{\gamma_F}{h}. \tag{1.9}$$

In summary, nucleation of WZ cannot occur away from the TPL. If nucleation occurs at the TPL, WZ nucleation is possible provided the edge energy of the WZ nucleus is smaller than the ZB one *and* the supersaturation $\Delta\mu$ is large enough to overcome the cost of creating a stacking fault. We must however recall that this model is based on an ideal situation in which the droplet sits on the NW top (without wetting the sidewalls) and the NW top facet and sidewalls are perpendicular to each other, which may not always be the case. Moreover, other factors may come into play, such as those that will be uncovered in Chapter 3.

1.4 Self-catalyzed GaAs NWs: a model system

We saw that gold is commonly used to induce the growth of both elemental and III-V NWs. In fact, the vast majority of works on VLS NWs use Au, which is quite surprising given the variety of materials and growth techniques, but means that Au is suitable to seed NW growth

in a very broad material and temperature window ranges. An interesting discussion of why gold is probably the most effective metal to induce NW growth can be found in Ref. [98].

On the other hand, the presence of Au in Si is extremely detrimental even at dopant concentrations. It has long been known that Au introduces both acceptor and donor states in the band gap, causing a significant reduction of carrier lifetimes, an effect detectable at concentrations as low as 10^{12} cm^{-3} [26].

While III-V NWs grown with gold still exhibit excellent electronic properties, use of Au must be avoided if integration with silicon is sought. Because of its low chemical reactivity, removal of Au surface contamination is difficult. This incompatibility with the Si platform stimulated the research for alternatives to gold. One alternative is to avoid the catalyst droplet altogether, which usually involves selective area growth, with long and expensive substrate preparation procedures. Furthermore, compared to VLS growth, the temperature/flux rate growth window is reduced and high aspect ratios are more difficult to obtain (with some notable exceptions [100]). Growth of III-V NWs using alternative foreign catalysts was explored, with examples including noble metals (Pd, Pt, Ag) and other metals (Ni, Mn, Cu and Fe) [32] each of them with unique advantages and drawbacks. For example, Mn has been exploited to grow spontaneously Mn-doped GaAs NWs [94]. The interested reader may refer to a recent review by Dick and Caroff on gold-free NW growth [32].

Finally, a third option is to exploit the VLS mechanism using a group III metal as catalyst *e.g.* In for InAs [57]. In this case we speak of a *self-catalyzed* growth mechanism. Gallium-assisted GaAs NWs is, by far, the most investigated system for self-catalyzed growth. The first report of GaAs whiskers grown using liquid gallium dates back to 1965 [11] and the first example of Ga-catalyzed GaAs growth by MBE was reported by Arthur and LePore in 1969 [8] when MBE was still in its infancy. In the attempt of achieving perfect two-dimensional growth, the authors described whisker growth as a parasitic effect induced by the presence of scratches and other surface defects. Since MBE was developed with the objective of realizing high-quality epitaxial films, the formation of such peculiar structures did not stimulate much interest.

The interest revamped in recent years, when the synthesis of epitaxial high purity Ga-seeded GaAs NWs was achieved [43, 71]. Ga-assisted growth has been reported first on GaAs [4, 43] and shortly afterwards on cleaved Si(100) [71] and Si(111) [103]. In both cases, a thin layer of Si oxide was deposited or spontaneously formed on the substrate. However, the role of the oxide is not yet completely clarified: Plissard et al. [114] found that NW growth can occur on both oxidized and oxide-free Si, although with different growth conditions. On one hand, the presence of oxide enhances the NW yield and reduces the formation of parasitic crystallites, but it reduces NW verticality [114]. In another paper,

Plissard et al. [115] showed that a SiO_2 mask with oxide-free openings can provide a high degree of verticality and suppress the growth of parasitic structures.

Whatever the actual role of the oxide,[4] in the self-catalyzed scheme it is essential that Ga droplets are formed and maintained throughout the growth, which usually involves higher temperatures compared to gold-catalyzed NWs [130]. The growth mechanism of self-catalyzed NWs is very similar to the classic VLS mechanism presented in the previous sections. However, the fact that the droplet is made mainly of Ga makes NW nucleation and morphology very sensitive to the As/Ga flux ratio: if the As/Ga flux ratio is too high, Ga droplets cannot form and GaAs islands grow instead. Conversely, if the As/Ga ratio is too low, the Ga droplet inflates during NW growth, leading to an inverse-tapered shape [27]. At intermediate flux ratios, the NW length is reported to increase linearly with growth time [27] and does not depend on the Ga flux. This implies that, as long as the droplet is preserved on the NW top, the stationary growth rate is limited by the As flux. The growth rate has been found to be proportional to the As flux [27, 120], provided that As/Ga ratio remains such that Ga droplets do not get consumed. However, the observed growth rates are significantly higher than those expected from the direct As flux impinging on the droplet, an observation that Ramdani et al. [120] interpreted as evidence of a re-emitted As flux scattered by the substrate and neighboring NWs, since As surface diffusion is negligible [120].

The fact that the droplet is made mainly of Ga also offers unique possibilities. For example, VLS growth can be stopped by simply reducing or interrupting the supply of Ga while keeping the As one, which leads gradually to the consumption of the droplet. Then growth can continue in vapor-solid mode to form a shell around the NW. The process is also reversible, and a new Ga droplet can be selectively restored on the NW top to resume VLS growth [116]. Selective Ga deposition on the top of crystals obtained by droplet epitaxy was suggested as a strategy to control diameter and density of self-catalyzed NWs [126].

Self-catalyzed GaAs NW growth is interesting as it can be seen as a toy model to test the basic principles of III-V NW growth. Since there are only two elements at play, Ga and As, the state of the droplet is completely defined by the As atomic fraction and by temperature. For example, Glas et al. [54] compared the NW elongation rate expected from mass balance with the rate from the nucleation theory (Eq. 1.5). Since the chemical potentials for the Ga-As system are known, the comparison enabled the authors to extract the nucleus edge energy Γ and the pre-exponential factor in Eq. 1.5. Knowledge of these two model parameters allows to predictively calculate all quantities of interest for NW growth,*e.g.* growth rates as functions of temperature and fluxes. In this way, Glas et al. were also able to estimate the As

[4] For a recent investigation on this subject, refer to the work of Matteini et al. [95, 96]

fraction in the droplet during growth, a quantity which is not accessible by experiment, to be of the order of 1%.

1.4.1 Crystal structure

In contrast to gold-catalyzed NWs, self-catalyzed GaAs NWs are typically found to have ZB structure occasionally affected by twinning [4, 24, 82, 129]. However, formation of WZ segments was observed in Ref. [129] and at the top of NWs of which the droplet has been consumed [5, 116]. In particular, several authors (Plissard et. al [114], Ambrosini et al. [5], Priante et al. [116] and Kim et al. [78]) found that consumption of the droplet leads systematically to the formation of a ZB-WZ-ZB sequence. The formation of ZB in self-catalyzed NWs was explained by Cirlin et al. [24] using the model of Glas [52] (Sect. 1.3.3). The authors estimate the relevant surface energies and conclude that the condition for nucleation at the TPL (expressed by Eq. 1.6) is not satisfied during stationary growth (where the contact angle β is about 130°) because of the low surface energy of liquid Ga, hence nucleation is away from the TPL and the structure is ZB. The ZB-WZ-ZB sequence may thus qualitatively explained by the change of contact angle experienced the droplet, which changes between at least 110° (all references above) to 0, passing through 90° where $\sin\beta$ has a maximum.

1.5 Heterostructure formation in nanowires: advantages and challenges

Epitaxy refers to the growth of a single crystal on top of another (usually semiconductors) with the same or fixed relative crystal orientation. We speak of *homoepitaxy* if the two crystals are of the same material and of *heteroepitaxy* if they are not. Epitaxial layers of two different materials are referred to as *heterostructures*. Heterostructures widely expand the range of application of semiconductor materials beyond simple doping. High quality heterostructures allowed for major developments, such as quantum wells and superlattices. Nevertheless, as mentioned previously, the quality of NW heterostructures obtained by top-down methods may be limited by the degradation of the starting bulk material (or thin film) upon etching. Actually, the advantage of bottom-up NWs is to grow structures that cannot be obtained in planar form. In the two-dimensional case (except for homoepitaxy), the epilayer and its substrate have generally different lattice parameters. Let a_s and a_e be the lattice parameters

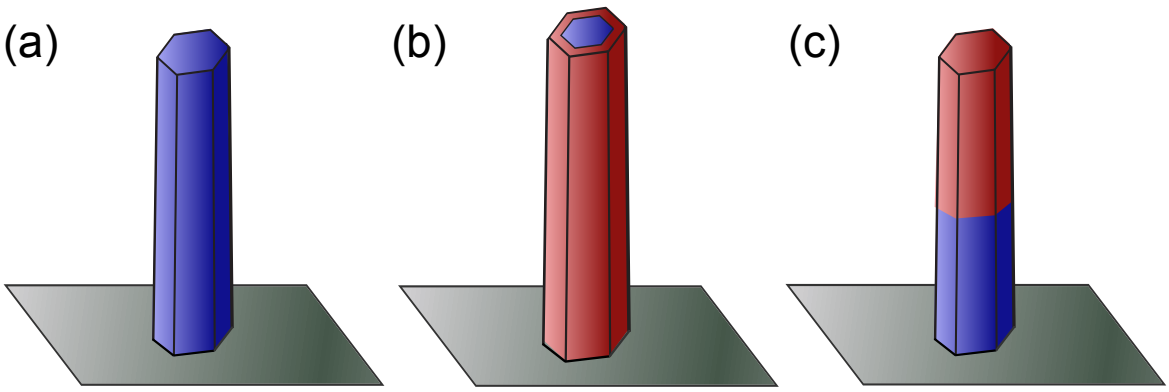

Fig. 1.7 The simplest nanowire heterostructures. a) NW-substrate; b) core-shell; c) axial.

of the relaxed substrate and epilayer, respectively, the *lattice mismatch* is:

$$f = \frac{a_e - a_s}{a_e}. \tag{1.10}$$

Since the substrate is much thicker than the epilayer, only the latter can deform laterally to accommodate the lattice mismatch. This induces stress in the epilayer. If $f > 0$ the stress is said to be compressive and if $f < 0$ the stress is said to be tensile.

In the case of growth, an epilayer of increasing thickness is deposited on the bulk substrate. As the thickness of the epilayer increases, the elastic energy stored in the crystal increases as well. At a certain point, called the *critical thickness*, it is energetically favorable for the strained epilayer to relax plastically by introducing misfit dislocations. Dislocations are known to degrade the electronic properties of the epilayer. The critical thickness is typically very small, even if the mismatch is only a few percent. Therefore, the choice of materials available to fabricate high-quality heterostructures is greatly reduced by the constraint of lattice matching.

Before discussing how NWs can palliate this problem, let us consider the basic heterostructures that is possible to realize in NWs, schematically depicted in in Fig. 1.7. The simplest NW heterostructure is the one with its own substrate. Then we have the core-shell, or radial heterostructure: this configuration is often motivated by the need to passivate the NW surfaces, or to realize radial quantum wells for example. However, growth of a NW shell is not very different from the vapor-phase growth of planar structures and, due to the typically large area of the NW sidewalls, one normally finds the same problems as encountered in planar heteroepitaxy.[5] Finally, we have the axial heterostructure, which is similar to the

[5]For a discussion of strain in the core-shell case, see Ref. [41].

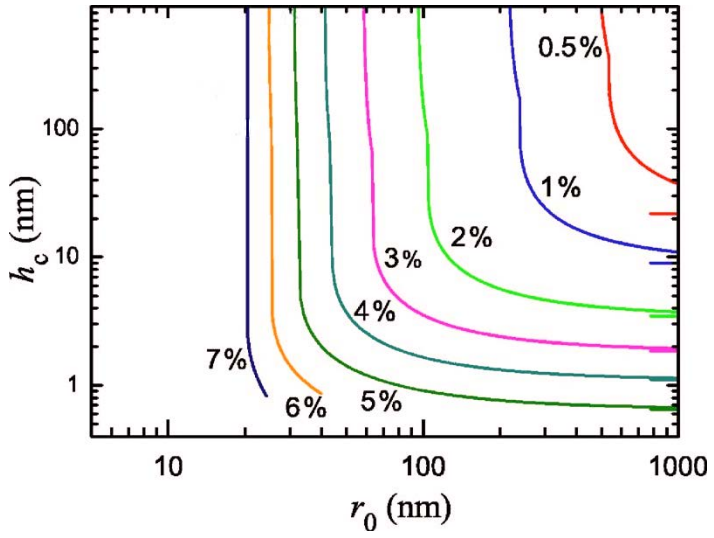

Fig. 1.8 Calculated critical thickness for a cylindical NW axial heterostructure as function of the NW radius, for several values of lattice mismatch. Adapted from Ref. [48]

NW-substrate heterostructure, with the important difference that in this case both materials can relax laterally.

This unique feature of NWs has stimulated theoretical efforts to quantify how efficient the mechanism of stress relaxation via lateral deformation can be. Glas [48] calculated the critical thickness as function of the NW radius, showing that it exist a radius, for a given lattice mismatch, below which the critical thickness becomes infinite. The results of the analytical model of Glas for a cylindrical NW are shown in Fig. 1.8.

The possibility of growing long NW segments without defects, even for large lattice mismatch, is one of the main advantages of axial NW heterostrucutures. It makes possible the growth of (virtually) any semiconductor heterostructure on (virtually) any substrate, solving a problem as old as epitaxy itself. However, this is not enough. A high quality axial heterostructure should have no dislocation, but it should also be straight (no kinking) and should have abrupt interfaces. Kinking is a change of growth direction when the junction is formed, which is often observed. For example, the InAs/GaAs NW interface is likely to kink [104] although the GaAs/InAs does not [33, 105]. Finally, there is the issue of interface abruptness, the control of which is essential for many applications and that we will investigate in detail in Chapters 4 and 5. In the next section, we are going to discuss the limitations of the VLS mechanism at obtaining sharp interfaces or graded interfaces with the desired compositional profile.

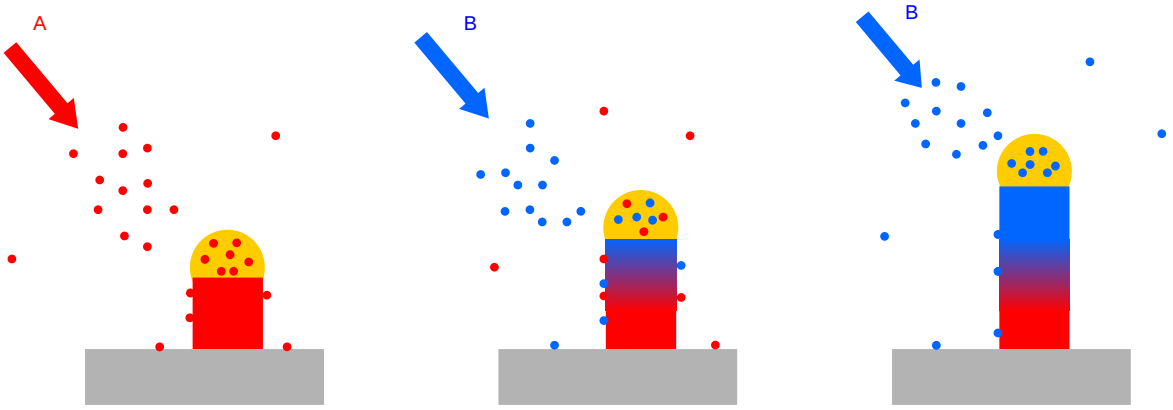

Fig. 1.9 Schematic representation of the switch between two materials A and B during NW growth, and its impact on the composition profile.

1.5.1 The reservoir effect

In the previous section we have seen that the easy strain accommodation in NWs allows for combinations of materials which are not possible to obtain without defects in two-dimensional structures. However, there is a major obstacle to the realization of perfectly abrupt interfaces: the droplet and its *reservoir effect* (or memory effect), schematically depicted in Fig. 1.9. Suppose we grow a NW of material A and want to perform a switch to a material B in order to produce an heterostructure (or a doping profile). If material A has accumulated in the droplet at the moment of the switch, and the wire continues to grow, a region of compositional gradient will be produced. The thickness of this region, hence the junction abruptness, will depend on the speed at which material A is purged from the droplet.

The effect was noted in an early demonstration of Si/SiGe superlattice in NWs, where the Ge and Si contents were found to change gradually rather than abruptly [145]. This point was addressed in a later work by Clark et al. [25], again in the case of Si/SiGe NWs, where some important observations were made: i) the compositional transition region is of the order of the NW diameter; ii) the compositional profile is asymmetric; iii) the widths of both leading and trailing transition regions scale with the NW diameter and iv) the leading and trailing profiles can be fitted with an exponential and an error function, respectively (Fig. 1.10a,b).

Observations i) and iii) imply that the reservoir effect should be reduced in thin NWs. The reason for this can be understood simply by considering that the number of atoms stored in the droplet is proportional to the droplet volume ($\propto R^3$, where R is the NW radius) while the size of the growth front is proportional to R^2. Hence, the length of the transition region will be proportional to R.

Let us now discuss some attempts that were made to circumvent or suppress the reservoir effect. One strategy is to reduce the solubility of the semiconductor material by changing

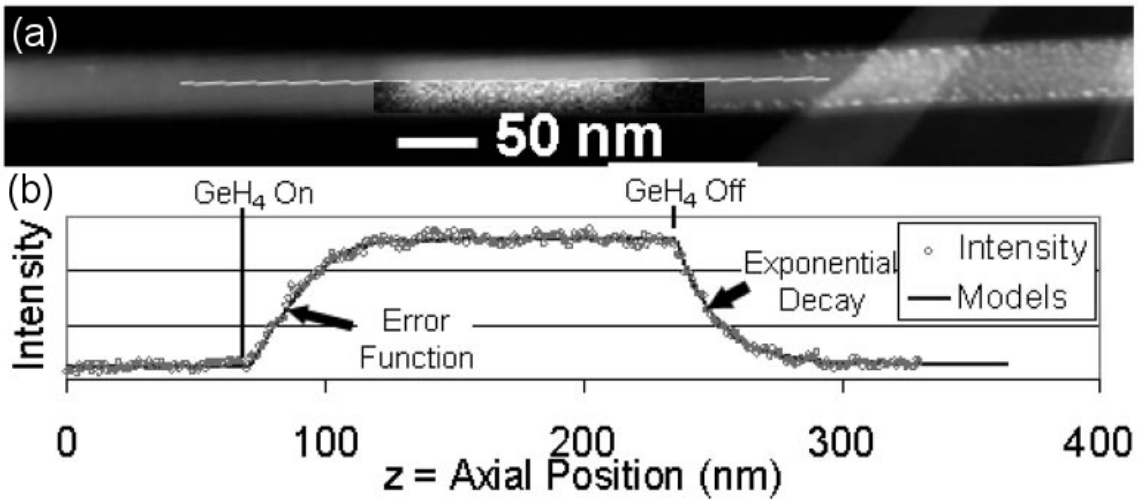

Fig. 1.10 a)Annular dark-field transmission electron microscopy image of a Si NW with a Ge insertion. In this imaging mode, the intensity is sensitive to the compostion and roughly proportional to the Ge concentration; b) intensity profile along the white line in a) and its fit. Adapted from Ref. [25].

the main constituent of the droplet, for instance by replacing Au with In for Si/Ge NWs. A similar approach consists in alloying the catalyst droplet with another metal which has a low solubility in the target solid. An interesting example was provided by Perea et al. [110] for Si/Ge NWs: at the end of the Ge segment, the droplet is exposed to gallium. Ga alloys preferentially with Au, reducing Ge solubility and pushing it into the solid.

Another interesting albeit sophisticated example of catalyst engineering was given by Dick et al. [31] for the optimization of gold-catalyzed GaAs/InAs NWs. The technique consists in pulsing small amounts of Ga at the end of the InAs segment. In such way, the addition of Ga to the liquid promotes InAs precipitation; however, by carefully adjusting the Ga pulses, the concentration of Ga is kept below the critical value at which precipitation of GaAs occurs. Dick et al. also found experimentally that the width of the transition region scales with the NW radius R, and that In concentration tail decays exponentially along the NW axis.

A more exotic approach consists in using a solid catalyst, thus growing the NWs in the so-called vapor-solid-solid mode (VSS). In general, for a given substance, its solubility in a solid is much lower than that in a liquid. In the *in situ* growth experiment performed by Wen et al. [143] it was clearly shown that it is possible to obtain sharp interfaces (≈ 1 nm for a NW diameter of 17 nm). On the other hand, the low diffusivity of the impinging species through the solid catalyst slows down the growth rate of at least one order of magnitude [80]. Finally, for III-V semiconductors, the naturally low solubility of group V elements can

be expolited to fabricate III-V-V heterostructure with very sharp interfaces, with examples mainly with GaP/GaAs [58, 72].

In this work we are going to study the impact of the reservoir effect on the synthesis of axial heterostructures in Ga-catalyzed NWs, using a second group V element (Chapter 4) or a second group III element (Chapter 5). We present and discuss possible strategies to fight against the reservoir effect, with surprising results in both cases.

Chapter 2

Experimental methods

2.1 Molecular beam epitaxy

Molecular Beam Epitaxy (MBE) is a technique for the epitaxial deposition of semiconductors, and it is widely utilized in modern technology. The source materials are converted in their gaseous form (usually by heating), resulting in an atomic or molecular *beam* that travels in vacuum and condenses on a hot substrate. Despite its conceptual simplicity, MBE was not developed until the late 1960s because of a low degree of purity and control, mainly caused by low vacuum quality. Progress in ultra-high vacuum (UHV) technology, as well as the availability of monocrystalline semiconductor substrates, eventually allowed for epitaxy of high quality films. Epitaxial growth occurs when the crystalline order of the deposited material is related to the one of the substrate crystal. Homoepitaxy refers to the growth of an overlayer on a substrate made of the same material. All other cases are referred to as heteroepitaxy. Characteristic aspects of MBE growth are:

- Relatively low growth temperature. Substrates are heated at a temperature high enough to grow ordered films, but low enough to minimize unwanted thermally-activated processes.

- Slow and precisely controlled growth rate. The typical MBE growth rate is about 1 ML/s, which corresponds to approximately 1 μm/h. This ensures surface migration, hence improving surface smoothness. In addition, a slow growth rates enables precise (sub-monolayer) thickness control.

- Flexibility. Growing compounds or alloys is relatively easy: it is sufficient to add a suitable vapor source, enabling compositional and dopant control.

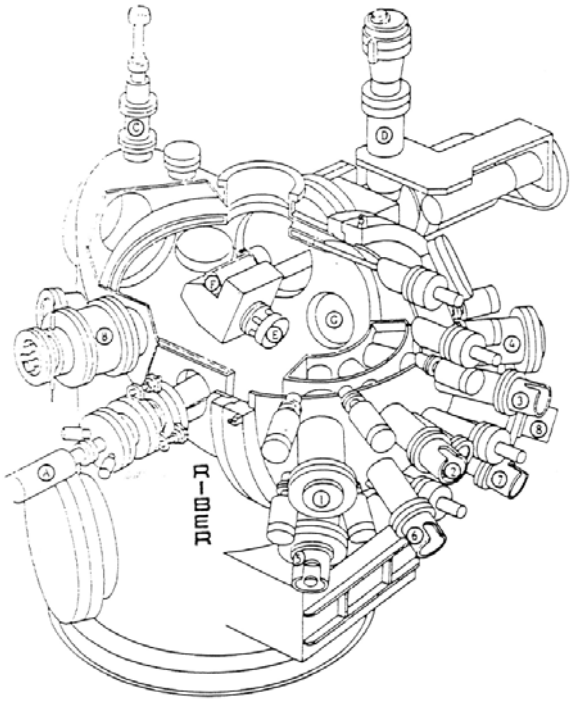

Fig. 2.1 Cutaway drawing of the Riber 32 MBE growth chamber. A: RHEED gun; B: quadrupole; C: transfer port shutter; D: manipulator; E: sample holder, F:manipulator ion gauge; G: RHEED screen; 1-8: effusion cells.

- UHV conditions. Ultra-high vacuum is necessary to avoid beam scattering and to reduce impurity incorporation. Such vacuum requirements for MBE allow the grower to use in situ characterization techniques, for example reflection high energy electron diffraction (RHEED), X-ray photoemission spectroscopy, mass spectrometry, etc.

A drawing of the MBE growth chamber used in this work, a Riber model 32, is shown in Figure 2.1. The growth chamber is made of UHV-compatible stainless steel and is connected to a load-lock module - for sample transfer from UHV to atmosphere and vice versa - through a preparation chamber, where samples are degassed.

UHV is achieved using a combination of an ion pump, a cryogenic pump and a Ti sublimation pump. The source materials are evaporated toward the substrate holder by a number of Knudsen-like effusion cells, which we will describe in the next section. Each cell is equipped with its own shutter to switch on and off the beam. In addition, a main shutter is placed between the cells and the substrate holder to allow interruption of all beams at the same time. A liquid nitrogen-cooled panel (cryopanel) is placed between the cells and on chamber walls. The cryopanel prevents the evaporation of atoms which are not coming directly from the sources, it thermally insulates the cells, and provides additional pumping. The substrate holder is placed on a manipulator capable of rotation around the

axis perpendicular to the substrate (for better deposition uniformity) and is fitted with an ion gauge for experimental flux determination. It can translate in the three spatial directions and rotate for sample transfer in and out of the growth chamber. The chamber is also equipped with a RHEED apparatus for structural surface analysis and a quadrupole for mass spectrometry. The substrate holder is designed to be fitted with molybdenum supports called molyblocs, on which samples are mounted. The substrate holder is heated by a filament embedded in a pyrolytic boron nitride (PBN) disk which can operate in a wide range of temperatures (0-800 °C). Molyblocs are heated radiatively, and the temperature is tracked with a thermocouple. However, temperature reproducibility is not guaranteed if only filament current and thermocouple temperature are used, because the emissivity of the molybloc-substrate changes between different substrates and different molyblocs. For this reason, temperature is typically evaluated by optical pyrometry, which essentially measures the irradiance j of the sample and converts it into a temperature via the Stefan-Boltzmann law: $j = \varepsilon\sigma T^4$, where T is the absolute temperature, σ is the Stefan-Boltzmann constant, and ε is the emissivity of the substrate, the latter determined by calibration with a reference (such as changes in surface reconstructions, melting point or desorption of a known material, etc.)

2.1.1 Effusion cells and flux measurements

Effusion cells are pivotal in MBE. Growth of compound semiconductors, especially for device applications, require excellent film uniformity and reproducibility. Uniformity is mostly determined by the geometry of the sources-substrate system, while reproducibility depends on the stability of the beam fluxes. Effusion is an evaporation phenomenon characterized by flow through a hole without inter-molecular collisions. This is only possible if the molecules mean free path is much longer than the orifice size. An ideal Knudsen cell is, by definition, an isothermal effusion cell with an orifice small compared to the evaporation area, which walls are so thin that they cannot scatter or absorb the evaporating molecules. Major drawbacks of Knudsen cells are the extremely low flux and the lack of collimation. In practice, real cells are equipped with elongated crucibles with large apertures at the top, to enhance the evaporation rate and to obtain a more directional flux. Consequently, the emitted flux is hard to predict from thermodynamics and it is determined experimentally in most cases. Such measurement is carried out by means of an ion gauge, or by measuring directly crystal growth rates as discussed in the next section.

Although the ion gauge is designed to measure a pressure (or better, a number density which is converted into pressure of a reference gas), a proportionality between pressure and flux is established in the steady state, by placing a nude gauge in front of the cells. The pressure reading obtained this way is commonly referred to as *beam equivalent pressure*

(BEP). Clearly, the same BEP for two different materials corresponds to different fluxes, because the ion gauge current depends on the ionization cross section. A ratio of different atomic or molecular BEPs can also be defined (for instance, As/Ga for GaAs), and it is called the beam equivalent pressure ratio (BPR). BPRs are less dependent on the experimental geometry than BEPs, therefore growth conditions are often expressed in terms of BPR.

The cells used in our system are composed of a PBN crucible heated by a Ta filament. PBN is extremely resistant to chemical attack and to thermal shock, and it also has very good thermal conductivity. A feedback thermocouple system controls the filament current and allows for a thermal stability better than 0.1 °C. However, in order to compensate for the change of evaporation area in the crucible during usage, a gradual increase of the cell temperature may be necessary ($\sim$1 °C/day).

2.1.2 RHEED

Reflection high-energy electron diffraction (RHEED), is one of the surface analysis techniques based on scattering of electrons. A high energy electron beam (between 5 and 40 keV) is directed on the surface at grazing incidence (1°-3°) and it is reflected toward a fluorescent screen. In contrast with LEED (low energy electron diffraction) where back-scattered intensity is measured and surface sensitivity is attained by using low energy electrons, RHEED attains its surface sensitivity thanks to the low incidence angle, so that the perpendicular component of the electron momentum relative to the surface plane is small, although the energy is not. RHEED allows one to distinguish between several types of surfaces, the diffraction pattern being given by the intersection of the surface reciprocal lattice and the Ewald's sphere. Without going into details, in practice we can have the following scenarios:

- Diffraction from a crystalline, atomically flat surface. The diffraction pattern is made of streaks.
- Polycrystalline surface. The randomly oriented surfaces give rise to a powder-like pattern (Laue circles)
- Rough surface. If the surface is rough, transmission through the asperities takes place, resulting in a spotty pattern. The aspect ratio of the asperities impacts the shape of the pattern spots, which elongate along the direction where the crystalline symmetry is broken. This allows one to distinguish between short, wide asperities (such as quantum dots) and tall, narrow ones (such as NWs).
- Amorphous materials. If no order is present, only a diffuse background is produced.

For NWs, the in situ diffraction pattern given by RHEED allows one to determine at a glance whether NWs have formed on the surface or not, and what is their dominant crystal structure (ZB, WZ, or twinned/mixed). Another important use of RHEED is to measure directly the crystal growth rate. In 1981, it was discovered that when MBE growth is initiated, the intensity of RHEED lines oscillates in time [63]. The phenomenon is directly related to the growth rate and since then it has been widely used to calibrate beam fluxes and alloy compositions. The existence of RHEED oscillations is explained as follows: when the surface is atomically flat, the RHEED diffracted intensity is maximum. As growth starts, random nucleation on terraces occurs, and the diffracted amplitude originating from different layers can interfere destructively, causing a reduction of the total intensity. The minimum is reached for a coverage value of 0.5. Then, when the new layer is completed, the intensity recovers its initial value. Therefore the oscillation period is the time required to the formation of a new layer, from which growth speed is readily obtained. However, RHEED intensity oscillations are not seen if the growth is not layer-by-layer, for example in the case of 3D island (or NW) growth. Another example is in the case of step flow growth, in which adatoms do not form nuclei on the surface, but diffuse to the nearest step where they get incorporated. In this case the crystal preserves its smoothness, and no oscillations are seen.

2.1.3 Absolute calibration of the vapor fluxes

Knowing the direction and magnitude of the atomic fluxes is important for NW growth modeling, in order to quantify the amount of material reaching the NW growth front and to identify the possible material pathways. The orientation of the vapor sources with respect to the substrate is known and fixed by the geometry of the growth chamber. We calibrated the fluxes of Ga, Al and As by performing RHEED oscillations on GaAs(001) substrates at 590 °C. In presence of an excess of As, thus with an atomic V/III ratio greater than 1, growth speed is limited by the flux of group III elements. By opening the shutter of Ga and measuring the oscillation period, the deposition rate in ML/s is obtained. Since the surface atomic density of GaAs(001) is known ($2/a_0^2$, where a_0 is the GaAs lattice parameter) the number of atoms per unit surface and unit time is easily obtained. Similarly, the Al flux is measured by growing an AlGaAs layer on GaAs(001) using the same Ga BEP used for the Ga calibration, so that the Al deposition rate is obtained by subtracting the Ga rate from the total growth rate. Alternatively, one can measure the AlAs growth rate directly.

On the other hand, calibration of the As_4[1] flux is done at V/III ratios < 1, so that the growth rate is As-limited. This condition can be achieved by growing in group III excess and

[1] Free evaporation of solid As, without cracking, produces As tetramers.

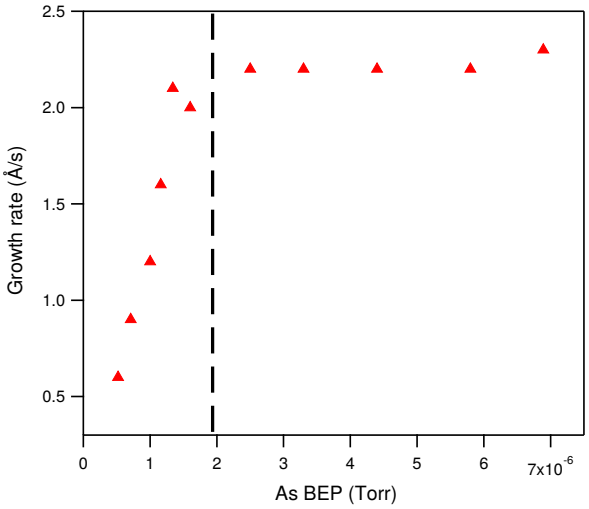

Fig. 2.2 Dependence of the GaAs(001) growth rate on the As_4 BEP, for a fixed Ga deposition speed of 2.2 Å/s. The dashed line indicates the approximate position of the As_4 BEP corresponging to stoichiometry.

changing the As BEP (Figure 2.2). As seen in Fig. 2.2 the growth rate increases linearly with the As BEP, until it saturates. The turning point correspond to a stoichiometric flux ratio, that is a V/III ratio equal to 1.

2.2 Electron microscopy characterization

2.2.1 Scanning electron microscopy

The scanning electron microscope (SEM) exploits electrons to produce images of a sample. A focused electron beam (with a diameter of about 1 nm) is scanned over the sample surface, where it interacts with matter, producing electrons and radiation that are collected by suitable detectors. A typical SEM column is composed by a cathode (either a hot filament or a field emission cathode) and by focusing magnetic lenses. Coils are used to deflect the beam to produce a scan in the directions perpendicular to the beam. The column is usually operated at between 1 and 40 kV. Because of the high electron kinetic energy, a large number of signals are produced in an SEM: backscattered electrons, secondary electrons, Auger electrons, Bremsstrahlung X-rays, characteristic X-rays and cathodoluminescence. However, most SEM are only equipped with detectors for backscattered and secondary electrons. The energy spectrum of the outgoing electrons contains an intense component made of elastically backscattered electrons, a component at slightly lower energy of electrons inelastically scattered by plasmons or interband transitions, followed by a long, flat region that extends

to energies down to 50 eV. The last region, at low energies, is that of the so-called "true" secondary electrons. These electrons underwent multiple scattering, thus they do not have any particular directionality and they are not material-sensitive, and for this reason are suitable for sample topography.

Images produced by primary and secondary electrons are substantially different. The images produced by the backscattered electrons show a strong compositional contrast, because the scattering probability is higher for higher atomic number Z, that is, regions with high average Z appear brighter than regions with low average Z. The spatial resolution of such images is limited by the long mean free path of backscattered electrons within the solid. Conversely, the images generated by secondary electrons allow for higher resolutions. For secondary electrons, the origin of image contrast is topographic and it is explained as follows: when the beam impinges orthogonally to the surface, secondary electrons with a certain escape depth are produced. When the incidence angle is varied, emission of secondary electrons (which still have the same escape depth) occurs closer to the surface, resulting in an intensity increase. Thus, steep regions and edges appear brighter than flat regions.

Modern SEMs are often equipped with an energy dispersive X-ray (EDX) detector. This enables one to obtain compositional maps of a surface, through identification of characteristic X-rays. Main limitations of EDX technique are the spacial resolution, determined by the electron beam interaction volume, and the low sensitivity at detecting light elements.

In this work, we imaged the samples using a FEI Magellan 400L, at a typical acceleration voltage of 10 kV. NW samples have been observed either as-grown or after mechanical transfer on a host substrate. The latter technique is very useful when long and thin NWs are observed, as otherwise the electron beam induces vibrations at the NW tips, making imaging difficult, if not impossible. The transfer is done by simply sliding the host substrate across the NW sample, the NW spontaneously adhering parallel to the surface. The Magellan 400L is also equipped with a detector under the sample holder, allowing for scanning transmission electron microscopy (STEM), both in bright-field and dark-field modes, which we occasionally used for preliminary NW structural and compositional analyses, before performing high-resolution transmission electron microscopy (TEM) as described in the next section.

2.2.2 Transmission electron microscopy

In contrast with SEM, where the image is formed using the secondary electrons generated in a volume close to the sample surface, in TEM a high energy beam (typically in the 100-300 keV range) is passed *through* a sample, the thickness of which is of the order of 100 nm or less. Since NWs are inherently thin, their observation by TEM requires no special preparation.

Generally speaking, TEM is capable of much higher resolutions compared to SEM. However, image interpretation is more complicated for TEM than for SEM and depend on the TEM *imaging mode*, which are mainly bright-field TEM, dark-field TEM and high-resolution (HRTEM).

In all cases, a detector is placed below the sample. In bright-field imaging, the electrons along the beam axis are collected. The contrast in bright-field mode results from beam losses, which are related to a number of factors such as thickness, density, composition, and crystal structure. In dark-field imaging, only some diffracted electrons are collected. This is achieved by introducing an aperture in the focal plane. Dark-field contrast is sensitive to crystal orientation. HRTEM, as suggested by the name, is performed at magnifications high enough to give atomic resolution, allowing for the study of the crystal structure and defects. However, while HRTEM images may look like pictures of the atomic lattice, the spots are actually generated by interference of various diffracted beams and HRTEM images must be interpreted with caution.

Finally, most modern TEMs can be operated in STEM mode as well. STEM is different from conventional TEM as the beam is focused into a very narrow spot. Similarly to SEM, the beam is scanned over the sample and the electrons are collected either along the beam axis (bright-field STEM) or by excluding it, using a ring-shaped detector (high-angle annular dark field, HAADF). The electrons collected by the annular detector have been scattered by Coulomb interaction with the atomic nuclei and electrons. The scattered intensity increases with Z and, as discussed in the next section, this imaging mode has high chemical sensitivity. Another advantage of the STEM mode is the ability to perform spatially-resolved spectroscopies such as electron energy-loss spectroscopy or EDX, allowing one to combine them with TEM images. The TEM used in this work is a FEI Titan Themis operated at 200 keV, equipped with an EDX detector.

2.2.3 Quantification of composition using medium and high-resolution HAADF contrast in scanning transmission microscopy

For the study of NW heterostructures it is of interest to measure the chemical composition with high spatial resolution. However, while EDX does provide good compositional measurements (typically within 1 atomic percent), its spatial resolution is typically limited to a few nanometers. Moreover, chemical mappings require long exposure times, increasing the risk of beam-induced damage of the sample. In the previous section we have seen that in modern TEMs Z-sensitive HAADF images and EDX measurements can be acquired on a given area of interest. If the function connecting the HAADF intensity and the composition

measured by another technique was known, then compositional mappings with high spatial resolution could be obtained from HAADF images. Let us write the HAADF intensity[2] I as [19, 79, 109, 123]:

$$I \propto d\langle Z^{\alpha} \rangle \tag{2.1}$$

where the exponent $\alpha \leq 2$ accounts for deviations from Rutherford nucleus scattering due to electron screening, and d is the sample thickness. The exact value of α generally depends on the material and on imaging conditions. Let us consider a binary III-V alloy, which is fully characterized by one parameter x, $Al_xGa_{1-x}As$ for instance. The average in Eq. 2.1 is:

$$\langle Z^{\alpha} \rangle = \frac{1}{2}\left[xZ_{\mathrm{Al}}^{\alpha} + (1-x)Z_{\mathrm{Ga}}^{\alpha} + Z_{\mathrm{As}}^{\alpha}\right] \tag{2.2}$$

If the thickness of the sample is constant, the proportionality factor in Eq. 2.1 can be eliminated by taking the ratio (the contrast R) of intensities of two regions with different compositions x and x_0, having intensities I and I_0 respectively:

$$R = \frac{I}{I_0} = \frac{xZ_{\mathrm{Al}}^{\alpha} + (1-x)Z_{\mathrm{Ga}}^{\alpha} + Z_{\mathrm{As}}^{\alpha}}{x_0Z_{\mathrm{Al}}^{\alpha} + (1-x_0)Z_{\mathrm{Ga}}^{\alpha} + Z_{\mathrm{As}}^{\alpha}} \tag{2.3}$$

from which x is readily obtained provided x_0 is known. The only unknown in Eq. 2.3 is the exponent α, which is obtained by a least square fitting of Eq. 2.3 to EDX measurements over the same region. For our experimental conditions, in the case of $Al_xGa_{1-x}As$, the best value of α is 1.7. Taking the reference I_0 on pure GaAs ($x_0 = 0$), we have $x \approx 2.73678(1-R)$. The uncertainty of the method is obtained by propagating the experimental error from EDX and by taking into account the (small) intensity fluctuations due to noise in the HAADF image. Such uncertainty on the composition is in the order of 2%. However, one must keep in mind that variations of intensities due to change of thickness or crystal structure are neglected in Eq. 2.3.

We have applied Eq. 2.3 to atomically-resolved images as well. However, in this case the intensity I is not a well-defined quantity, since its value depends on where we measure it: on top of a group III column, on top of a group V column, between columns or between planes. Since in this work we are interested in tracking the composition along the NW axis, as a simple approach we assigned to each atomic plane the average HAADF intensity over that plane, neglecting the possible overlap with the intensities produced by neighboring planes. This approach will be illustrated in Chapters 4 and 5.

[2] After subtraction of the detector background (dark counts).

Chapter 3

Study of correlations in the stacking sequence of a NW

This chapter includes content from: G. Priante *et al.* Phys. Rev. B **89**, 241301(R) (2014) [118]

3.1 Introduction

In Chapter 1, Section 1.3.3, we have seen that (with the notable exception of nitrides) most III-V semiconductors adopt the cubic zinc blende (ZB) structure in their bulk form, while both ZB and the hexagonal wurtzite (WZ) structures can be found in III-V NWs. We also reviewed that, for very thin NWs (diameters $\leqslant 10$ nm), the WZ stacking is thermodynamically favored [1, 90, 107], while for thicker ones the formation of WZ or ZB is driven by growth kinetics [40, 52], which in turn are governed by growth conditions, such as temperature and supersaturation. Recall that the two structures are distinguished by the stacking order of the III-V bilayers (that we refer simply to as monolayers, or MLs) along the $[111]_{\mathrm{ZB}}/[0001]_{\mathrm{WZ}}$ direction, which is also the preferential NW growth direction. ZB is characterized by a stacking sequence of the type ABCABC... while WZ by an ABABAB... sequence.

In certain growth conditions, NWs display a marked phase mixing, namely the stacking sequence "hesitates" between ZB and WZ, possibly leading to sequences of higher complexity. If such sequence possesses a periodicity, the unit period is referred to as a high-order polytype. A well-known, strongly polytypic IV-IV material is silicon carbide (SiC), for which more than 200 polytypes are known, altough the most common are the 3C, 4H and 6H in Ramsdell's notation [121]. Note that 3C and 2H correspond to ZB and WZ, respectively. The existence of such polytypes is due to some interaction between individual layers, in the sense that the

growing layer "feels" the stacking configuration below. In bulk SiC, polytypism has been sometimes attributed to the presence of screw dislocations [55], but NWs generally do not display this kind of defect. Whatever the actual mechanism, the interaction, depending on the underlying sequence, favors one type of stacking or the other (cubic or hexagonal). The result of interaction is encoded into the stacking sequence in the form of *correlations*.

In some cases, NWs may exhibit other forms of *long range* ordered structures, such as twin planes superlattices [2]; factors such as catalyst droplet distortion, dictated by the three-dimensional NW geometry [2], or stress at the NW sidewalls [148] may then come into play.

The existence of *short range* inter-layer correlations has been observed in bulk SiC and SiC NWs; in particular Kohno *et al.* [81] studied SiC NWs by high-resolution transmission electron microscopy (HRTEM). Describing the stacking process as a random walk, they concluded that the observed SiC stacking was "not a simple random process nor deterministic". However, while some degree of correlation is expected in III-V NWs as well, no direct observation has been reported prior to the present work. Short segments of the 4H structure have been occasionally reported in InSb [91], GaAsSb [30] and GaAs [127]. Johansson *et al.* [74] calculated the formation probabilities of several polytypes in III-V NWs, by introducing short range inter-ML interaction via an axial-next-nearest-neighbor (ANNNI) model, previously used for describing SiC polytypes [23, 87]. Yet correlations and interactions between MLs in NWs remain poorly documented and call for better understanding.

In this chapter, we present a detailed structural analysis of an InP NW and interpret it statistically. A simple probabilistic treatment demonstrates the existence of short range interactions between MLs which influence stacking during growth. We then show that this can be modeled within the classical nucleation theory, provided the step energy of the two-dimensional nucleus Γ (Section 1.3.1) depends not only on the crystallographic positioning of the nucleus (cubic or hexagonal), but also on that of the preceding MLs. It will be shown that the ANNNI interaction only through the σ term, as done in Ref. [74], is not sufficient to account for phase mixing in our NWs.

3.2 NW synthesis and data collection

Vertical InP NWs were grown in the vapor-liquid-solid mode by MBE at 400°C on a InP (111)B substrate, using gold seed droplets (Fig. 3.1). Gold-catalyzed growth at this temperature is known to produce a mix of crystal phases, while the NW remains mostly hexagonal [21]. The occurrence of stacking defects in ZB materials qualitatively results from the small difference in cohesive energy between the WZ and ZB structures. In this case, for

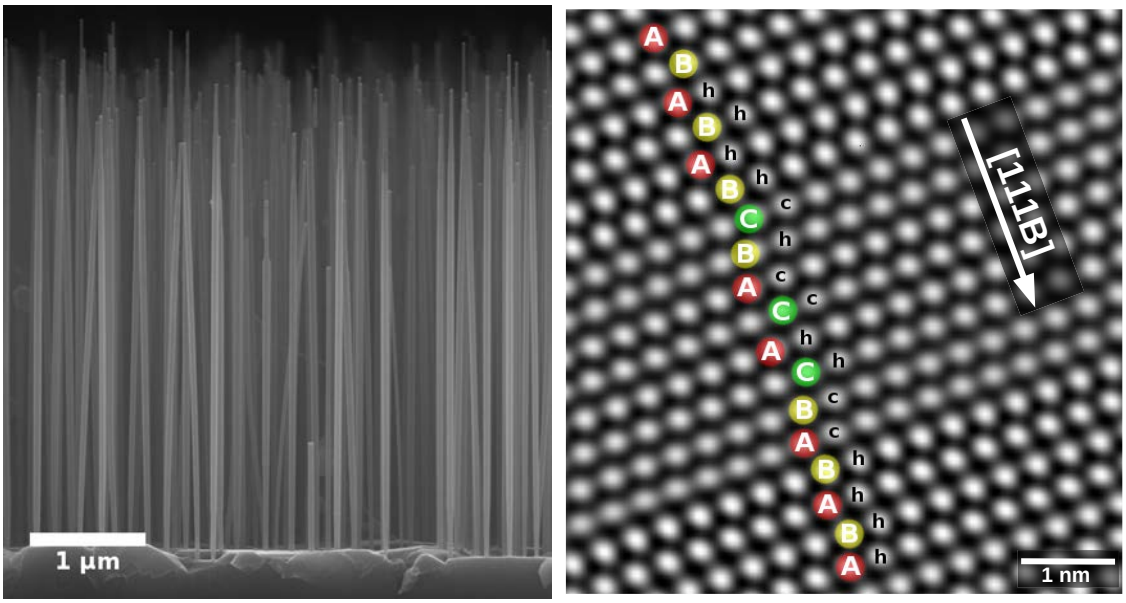

Fig. 3.1 Left: Cross-sectional SEM image of the sample. Right: labeling of the monolayers on a filtered fast-Fourier-transformed HRTEM image. Note that growth direction points downwards.

InP, the difference is calculated to be about 11 meV/pair [1, 12]. The stacking sequence used for the following analysis was obtained from overlapping HRTEM images of a single NW taken along the $\left[1\bar{1}0\right]_{\mathrm{ZB}}$ zone axis, that is, perpendicularly to one of the six NW sidewall facets. Reading was done by eye after application of a fast Fourier transform filter to reduce noise.

Each ML was indexed as cubic (*c*) or hexagonal (*h*). It is important to note that in principle, for III-V semiconductors, it suffices to consider the nearest underlying layer: the new ML is *c* if its III-V bonds are parallel to that of the preceding ML, and *h* if not (see Fig. 3.8). However, we do not resolve the In-P dumbell in our HRTEM images. We thus have to examine the lateral positions of the MLs (indexed by capital letters) and index the MLs as *h* or *c* depending on its position with respect to the *two* neighboring MLs (*h*: ABA, *c*: ABC), as depicted in Fig. 3.1. The labeling is not unique, since the reference can be taken in three different ways (2 MLs below, above, or around a given layer). This does not matter for our analysis, since all indexation schemes produce the same sequence, shifted by one or two MLs. In the context of growth, it is natural to refer to the underlying (already grown) MLs. Finally, we call *segments* the series of consecutive MLs of identical crystalline nature, either *h* or *c*.

The NW under study is prevalently hexagonal. No long-range periodicity nor high-order polytypes were detected. In this NW, a total of 2833 MLs were indexed, of which 230 cubic

Table 3.1 Measured relative frequencies of short sequences.

Single layers (%)	Doublets (%)	Triplets (%)
$h = 91.9$	$hh = 88.2$	$hhh = 84.7$
		$hhc = 3.5$
	$hc = 3.7$	$hch = 1.0$
		$hcc = 2.8$
$c = 8.1$	$ch = 3.7$	$chh = 3.5$
		$chc = 0.2$
	$cc = 4.4$	$cch = 2.7$
		$ccc = 1.6$

and 2603 hexagonal, distributed into 106 and 105 segments respectively. Fig. 3.2 shows the histograms of the lengths of c and h segments in terms of counts and frequencies, defined as the number of segments of given length over the total number of segments *of the same type* (c or h). The shape and width of the two distributions are dramatically different. The cubic distribution is narrow (no segment is longer than 5MLs), whereas the hexagonal one is much broader, extending up to segments of 192 MLs. The cubic distribution peaks at 2 ML-segments, the number of which is well above that of single c insertions. This is a surprising finding, because if there were no correlations we would expect a monotonically decreasing of the distribution with the segment length.[1]

Table 3.1 gives the frequencies of all sequences up to 3 ML long. The longer sequences occurring only a few times are statistically less representative and, as will be seen, are not necessary to our analysis. Note that the frequencies of some short sequences are equal *e.g.* $f(hhc) = f(chh)$. This property will be used later.

3.3 Probabilistic analysis of the stacking sequence: conditional probabilities

We now show that our data prove the existence of correlations between MLs positions. NW growth is described as a stochastic process. At each step, a new ML is formed, either in h or c position, with a certain probability, which may depend on the arrangement of the underlying MLs. We test three different schemes where the positioning of the new ML:

- is independent of the stacking of the underlying MLs (no correlation);

[1] In such case, if $p_i < 1$ is the probability of forming a layer of type i, then the probability of forming n layers of type i is p_i^n, which decreases monotonically with n.

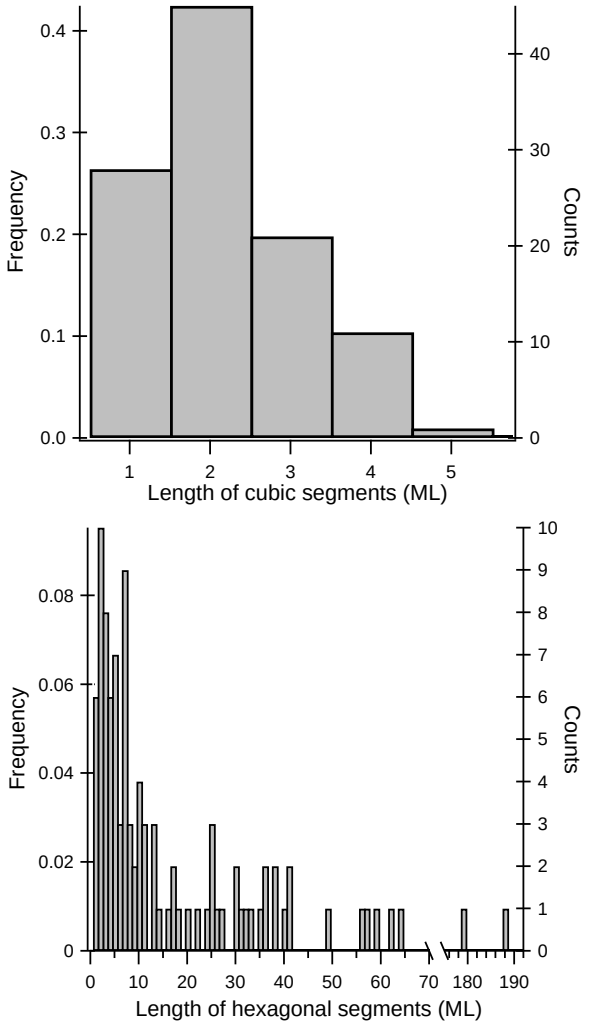

Fig. 3.2 Distributions of the cubic (top) and hexagonal (bottom) segments. Note that the histogram for hexagonal segments is broken between 70 and 150 MLs.

- depends on the sole underlying nearest neighbor ML (NN correlation);
- depends on the nearest and next nearest MLs (NNN correlation);

In the case of no correlation, all ML formation events are independent. Therefore, the probability of forming a ML in h or c position is simply given by the relative frequency f of each type of layer, namely $p_h = f(h)$ and $p_c = f(c)$, with $p_h + p_c = 1$, since the two cases are mutually exclusive.

In order to go beyond and account for possible correlations, we recall a fundamental property of probability, stating that the probability of two events A and B occurring one after another is:

$$P(A \text{ after } B) = P(A)P(B|A) \tag{3.1}$$

where $P(B|A)$ is the conditional probability of B occurring given that A has occurred. We read $B|A$ as "B given A". The order is very important here, because $P(B \text{ and } A) = P(B)P(A|B) \neq P(A)P(B|A)$. The NN scheme is then specified by the conditional probabilities for each type of ML given the position of the underlying ML. These conditional probabilities can be extracted from the frequencies of doublets. As an example, the frequency of the hc doublet reads:

$$f(hc) = p_h p_{c|h} = f(h)p_{c|h} \tag{3.2}$$

with $p_{c|h}$ the probability of forming a c ML on top of an already formed h ML, and similarly for all other doublets (hh, ch and cc). The four conditional probabilities, which must satisfy normalization conditions $p_{h|h} + p_{c|h} = 1$, $p_{h|c} + p_{c|c} = 1$, are then easily obtained from Table 3.1.

This method is readily extended to NNN correlation, by considering the frequencies of triplets. The probability of finding, for instance, sequence hch is:

$$f(hch) = p_h p_{c|h} p_{h|hc} = f(hc)p_{h|hc} \tag{3.3}$$

Hence, counting the frequencies of hch triplets and hc doublets yields the conditional probability $p_{h|hc}$. The conditional probabilities satisfy conditions $p_{h|uv} + p_{c|uv} = 1$ for all combinations $u, v = h$ or c. The probabilities calculated for the three schemes are reported in Table 3.2, from which we can see clearly that the probability of forming an$h$ or c ML is not independent of the nature of the MLs lying further down. For example, the probability of forming an h ML is very different if the ML is formed on top of another h ML ($p_{h|h} = 96\%$) or on top of a c one ($p_{h|c} = 46\%$).

We can now combine the normalization conditions with the the fact that symmetric sequences have the same frequency, to show that the probabilities of the zero-correlation

Table 3.2 Probabilities derived from experimental data (with significant digits), for the three schemes considered.

No correlation	NN-correlation	NNN-correlation
$p_h = 0.9188$	$p_{h\|h} = 0.9600$	$p_{h\|hh} = 0.9607$
		$p_{h\|ch} = 0.94$
	$p_{h\|c} = 0.457$	$p_{h\|hc} = 0.26$
		$p_{h\|cc} = 0.62$
$p_c = 0.0812$	$p_{c\|h} = 0.0404$	$p_{c\|hh} = 0.040$
		$p_{c\|ch} = 0.06$
	$p_{c\|c} = 0.539$	$p_{c\|hc} = 0.74$
		$p_{c\|cc} = 0.37$

scheme can be calculated from those of the NN scheme, which in turn can be calculated from the NNN ones. Consider the doublets *hc* and *ch*: they must have the same frequency $f(hc) = f(ch)$. Because we can write $f(hc) = p_h p_{c|h}$ and $f(ch) = p_c p_{h|c}$ we have:

$$p_h p_{c|h} = p_c p_{h|c} = (1 - p_h) p_{h|c} \tag{3.4}$$

which, solved for p_h gives:

$$p_h = \frac{p_{h|c}}{p_{c|h} + p_{h|c}} \tag{3.5}$$

a similar straightforward calculation shows that the conditional probabilities of the NN-scheme can be deduced from the NNN-scheme.

3.4 Distribution of cubic and hexagonal segments

Now that we have extracted the formation probabilities for each type of layer, we can use them to work out the distribution of the segments plotted in Fig. 3.2. We perform the calculation for cubic segments only, the hexagonal case is obtained simply by exchanging h and c. We note that any c segment must begin just after and end just before a h layer or, in other words, it starts with a *hc* sequence and ends with a *ch* one. The frequencies for each segment length, expected in the uncorrelated, NN- and NNN-correlated schemes are given in Table 3.3.

For each scheme we check that the distributions are normalized, by summing up the columns in Table 3.3. For the uncorrelated scheme, we have:

$$p_h \sum_{m=0}^{\infty} p_c^m = p_h \frac{1}{1 - p_c} = \frac{p_h}{p_h} = 1 \tag{3.6}$$

Table 3.3 Calculated distribution of the lengths of cubic segments. The common starting sequence is underlined.

Length (ML)	Sequence	No correlation	NN-correlation	NNN-correlation
1	$\underline{hc}h$	p_h	$p_{h\|c}$	$p_{h\|hc}$
2	$\underline{hc}ch$	$p_c p_h$	$p_{c\|c} p_{h\|c}$	$p_{c\|hc} p_{h\|cc}$
3	$\underline{hc}cch$	$p_c^2 p_h$	$p_{c\|c}^2 p_{h\|c}$	$p_{c\|hc} p_{c\|cc} p_{h\|cc}$
n	$\underline{hc}c\ldots ch$	$p_c^{n-1} p_h$	$p_{c\|c}^{n-1} p_{h\|c}$	$p_{c\|hc} p_{c\|cc}^{n-2} p_{h\|cc}$

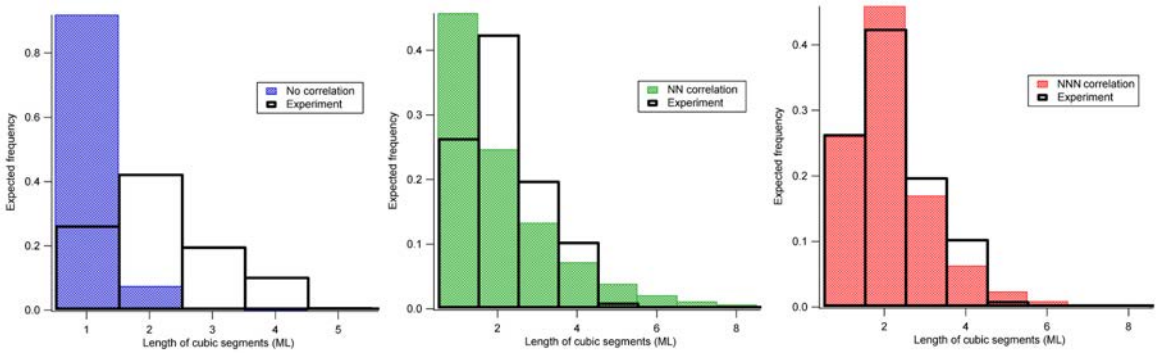

Fig. 3.3 Distributions of cubic segments calculated from Table 3.3, using the probabilities in Table 3.2, compared with the experimental data.

for the NN scheme:

$$p_{h|c} \sum_{m=0}^{\infty} p_{c|c}^m = p_{h|c} \frac{1}{1-p_{c|c}} = \frac{p_{h|c}}{p_{h|c}} = 1 \tag{3.7}$$

and, for the NNN scheme:

$$\begin{aligned} p_{h|hc} + p_{c|hc} \sum_{m=0}^{\infty} p_{c|cc}^m p_{h|cc} &= p_{h|hc} + p_{c|hc} \frac{1}{1-p_{c|cc}} p_{h|cc} \\ &= p_{h|hc} + p_{c|hc} \frac{p_{h|cc}}{p_{h|cc}} = p_{h|hc} + p_{c|hc} = 1 \end{aligned} \tag{3.8}$$

Table 3.3 shows that, in the cases of no or NN correlation, the distributions are exponentially decreasing functions of n. This kind of distribution has indeed been observed in Ref. [75] for GaP NWs. Hence these two schemes cannot reproduce the peak at $n = 2$ of our experimental data (Fig. 3.2), *whatever the values of the probabilities*. Conversely, the NNN scheme correctly predicts not only the shape of the distribution but also the height of each channel (Fig. 3.3 and Fig. 3.4a). Here, the exponential decrease is recovered only for c segments longer than two MLs.

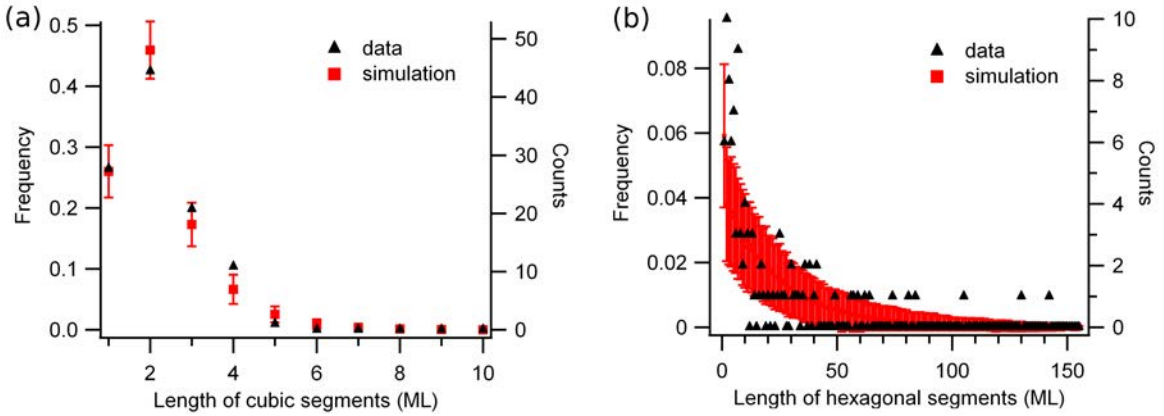

Fig. 3.4 Distributions of the cubic (a) and hexagonal (b) segments. Triangles give the experimental values. For the simulations, the squares represent the average and the error bars the standard deviation corresponding to a large number of NWs having the finite length indicated in the text.

The approach was corroborated by generating one thousand 2833 ML-long random sequences, using the NNN conditional probabilities listed in Table 3.2. Clearly, we have to select two arbitrary layers to start with. Given that our NW is mostly hexagonal, we chose two h layers. These numerical simulations allow us to determine the dispersion of the observables, such as the frequencies and segment distributions. The observables are normally distributed, the corresponding standard deviation is plotted in Fig. 3.4 together with the experimental data, showing that the simulation agrees very well with our experiments for both c and h segments.

3.5 The pair correlation function

To conclude the analysis of the experimental data, we want to find possible hidden periodicities, which indicate a tendency to polytypism. Let us define the following pair correlation function:

$$g(n) = \frac{1}{L-n} \sum_{i=1}^{L-n} t_i t_{i+n}, \quad t_i = \begin{cases} +1 & \text{if} \quad h \\ -1 & \text{if} \quad c \end{cases} \tag{3.9}$$

We can evaluate the extreme values of $g(n)$. From the definition, it follows that $g(0) = 1$. Its asymptotic value can be evaluated considering that, for increasing n, correlations should become less and less important. Therefore, how often each contributing pair occurs (hh, hc, ch and cc) is given by the probabilities in the independent picture. The contribution will be

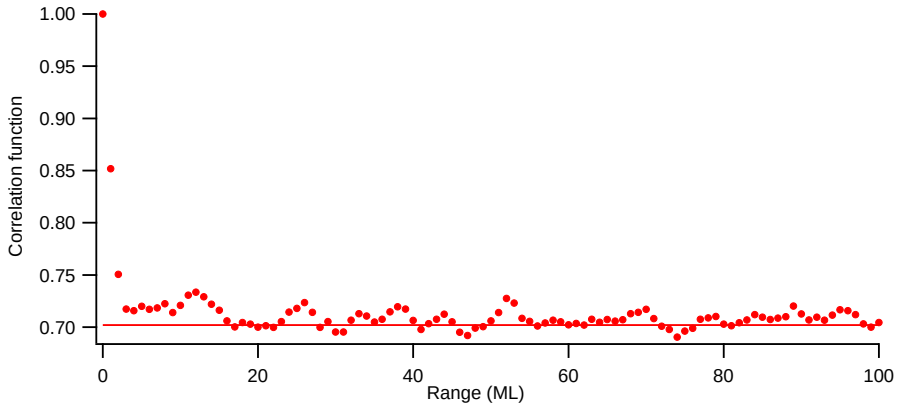

Fig. 3.5 Plot of the pair correlation function $g(n)$ up to $n = 100$. The horizontal line represents the asymptotic value $(p_h - p_c)^2$.

positive for *hh* and *cc* and negative in the other two cases, thus, for $n \gg 1$:

$$g(n) \approx p_h^2 - 2p_h p_c + p_c^2 = (p_h - p_c)^2 \tag{3.10}$$

which in our case is equal to 0.702. The plot of $g(n)$ for our experimental sequence is given in Figure 3.5.

From the figure we notice that the $g(n)$ decreases sharply up to $n = 3$, then it oscillates. These oscillations display no clear periodicity. To understand if these oscillations correspond to some form of long range order or are noise due to finite sampling, we compare the $g(n)$ from the experiment with the one obtained from simulated sequences in the NNN-scheme, having the same length L as the one from experiment. In Figure 3.6, the experimental correlation function is plotted together with the result of simulation. As done previously, the simulated $g(n)$ is obtained as the average of 1000 sequences, with bars representing twice the resulting standard deviation of each point.

Each of the sequences we generated presented irregular oscillations of $g(n)$. From the comparison in Fig. 3.6 we conclude that only the first three points can be statistically distinguished from each other, validating our hypothesis that the the NNN scheme is the minimum (and sufficient) range of correlation to reproduce the data. The correlation may definitely extend beyond the next-nearest neighbor, but to assess this a much larger set of data is required. We also conclude that, in our experiment, there is no significant presence of long-range correlations or high-order polytypes.

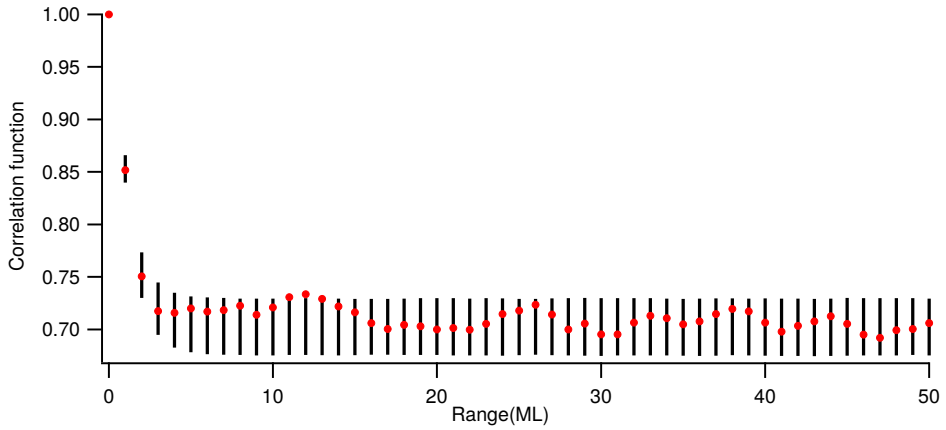

Fig. 3.6 Plot of experimental pair correlation function $g(n)$ up to $n = 50$ (red disks), together with the simulated $g(n)$ and its dispersion (black bars, the mean is located at the center), as obtained from a large number of sequences generated with the NNN-scheme.

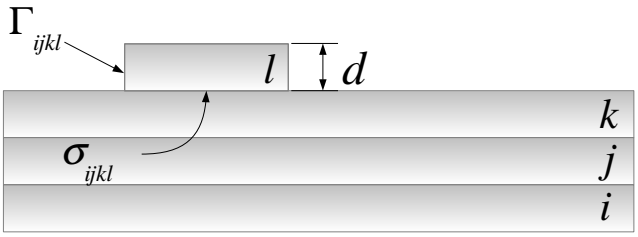

Fig. 3.7 Schematics of the nucleation process.

3.6 Including correlations in the classical nucleation theory

We now demonstrate that these correlations can be accounted for in the framework of classical nucleation theory. We thus consider the formation of a two-dimensional nucleus on the top facet of the NW (Fig. 3.7). The nucleus can be either in c or h position. However, in line with the previous discussion, we assume that its work of formation ΔG depends *also* on the nature of the two underlying MLs.

To compute this stack-dependent ΔG, an expression connecting the stacking configuration and the nucleus formation energy is needed. Looking again at Figure 3.8, we recognize that forming a layer in c (or h) position is equivalent to align the III-V bonds in a parallel (or anti-parallel) configuration. Therefore, the energy cost of forming a layer in a given position may be directly related to the relative direction of the III-V bonds. Since there are only two possible orientations, we can affect to each ML i a pseudo-spin $s_i = \pm 1$, depending on the direction of its III-V bonds, the rule being that $s_i = s_{i-1}$ if ML i is of type c (bond

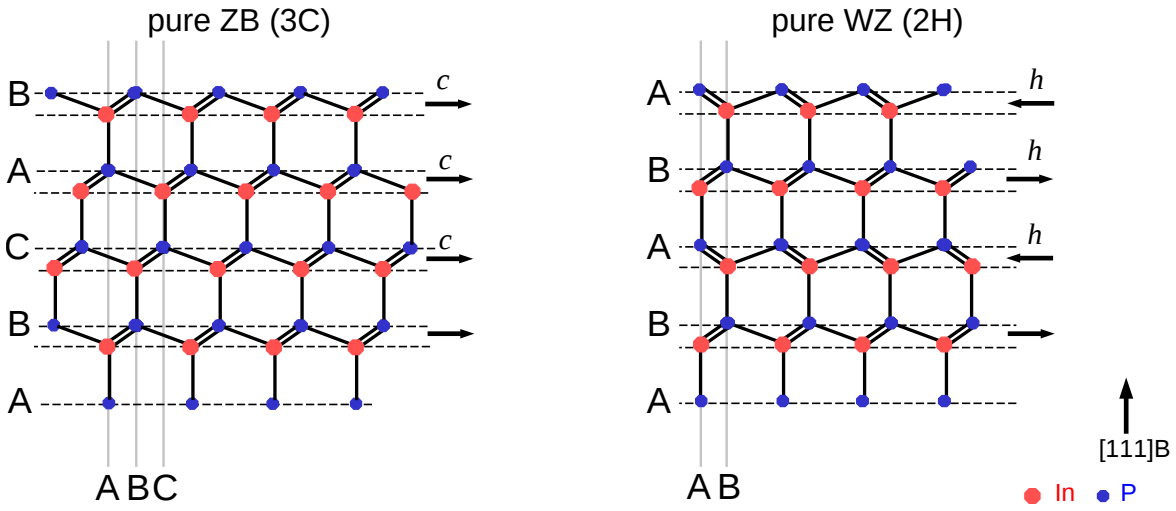

Fig. 3.8 Orientation of the III-V bonds the zincblende and wurtzite structures, and the corresponding orientation of pseudo-spins.

Table 3.4 Correspondence between the (h,c) and spin notations.

Triplet	Spin	Triplet	Spin
hhh	$1\bar{1}1\bar{1}$	*hhc*	$1\bar{1}11$
chh	$11\bar{1}1$	*chc*	$11\bar{1}\bar{1}$
hch	$1\bar{1}\bar{1}1$	*hcc*	$1\bar{1}\bar{1}\bar{1}$
cch	$111\bar{1}$	*ccc*	1111

parallel to that of the preceding ML) and $s_i = -s_{i-1}$ if it is of type h [23, 74]. From the definition it follows that an ordered triplet in terms of c and h is equivalent to an ordered spin quadruplet. However, since the spin description is unaltered by reversing all spins, the first spin is arbitrary. The correspondence between (h,c) triplets and spin quadruplets is given in Table 3.4, where the first spin is arbitrarily taken to be $+1$.

The main dependence of the classical nucleation rate on ΔG is exponential. Then, taking the same Zeldovich factor for all nuclei (Section 1.3.2), the probability per unit time of forming a nucleus of spin l over sequence of spins ijk reads:

$$\lambda_{l|ijk} = A \exp\left(-\frac{\Delta G^*_{ijkl}}{k_B T}\right) \tag{3.11}$$

with k_B the Boltzmann constant, T the temperature, ΔG^*_{ijkl} the stack-dependent nucleation barrier and A a constant. Taking the ratio of Eq. (3.11) for two complementary nucleus configurations $ijkl$ and $ijkl'$, with $l \neq l'$, yields the difference in energy barriers as a function

of the conditional probabilities:

$$\Delta G^*_{ijkl} - \Delta G^*_{ijkl'} = -k_B T \ln \frac{p_{l|ijk}}{p_{l'|ijk}} \tag{3.12}$$

Assuming a triangular nuclei, the barrier writes (Section 1.3.1):

$$\Delta G^*_{ijkl} = 3\sqrt{3} d \frac{\Gamma^2}{\Delta\mu - \sigma/d} \tag{3.13}$$

with d the step height, Γ the effective step energy (per unit area) [52], $\Delta\mu$ the chemical potential difference (per unit volume) between liquid and ZB solid, and σ the energy (per unit area) of the interface between nucleus and underlying NW (Fig. 3.7). ΔG depends on i, j, k, l via the yet unspecified dependences of σ and Γ on the spins. Since we have four pairs of complementary configurations, substituting Eq. (3.13) into Eq. (3.12) yields a system of four equations of the form:

$$\frac{\Gamma^2_{ijkl}}{\Delta\mu - \sigma_{ijkl}/d} - \frac{\Gamma^2_{ijkl'}}{\Delta\mu - \sigma_{ijkl'}/d} = -\frac{k_B T}{3\sqrt{3} d} \ln \frac{p_{l|ijk}}{p_{l'|ijk}}. \tag{3.14}$$

The right-hand side of this equation contains all the experimental data: we set it to be equal to a parameter $q_{ijkl,l'}$, the sign of which is determined by the probability ratios. From the values in Table 3.2 we observe that the $q_{ijkl,l'}$ term is negative in three out of four cases. We rewrite Eq. 3.14 as:

$$\boxed{\frac{\Gamma^2_{ijkl}}{\Delta\mu - \sigma_{ijkl}/d} - \frac{\Gamma^2_{ijkl'}}{\Delta\mu - \sigma_{ijkl'}/d} = q_{ijkl,l'}} \tag{3.15}$$

In the following sections, we discuss the attempts made to solve system 3.15.

3.6.1 Standard choice

In the simple models reviewed in Chapter 1, *only* the position of the nucleus relative to the preceding ML is taken into account, σ (which thus writes σ_{kl}) is set to zero for nucleation in c position ($s_l = s_k$) and to some $\sigma_h > 0$ for nucleation in h position ($s_l = -s_k$) [40, 52, 75]. To account for the formation of WZ in NWs, in Ref. [52] it was proposed that the edge energy of the nucleus also depends on its positioning relative to the previous ML (hence $\Gamma = \Gamma_{kl}$) and a step energy was assigned to each type of nucleus, namelyΓ_h for a nucleus in

h position and $\Gamma_c > \Gamma_h$ for a nucleus in c position. Thus, the system Eq. 3.15 reduces to:

$$\frac{\Gamma_h^2}{\Delta\mu - \sigma_h/d} - \frac{\Gamma_c^2}{\Delta\mu} = q_{ijkl,l'} \tag{3.16}$$

This system has four equations and four unknowns (Γ_h^2, Γ_c^2, $\Delta\mu$ and σ_h). The left-hand side of the equation is the same in all four cases, but it should be simultaneously equal to a negative and a positive quantity. Hence, there is no solution whatever the values of the parameters.

3.6.2 ANNNI for the nucleus interface energy

Specifically to account for the formation of polytypes, Johansson *et al.* [74] proposed to make σ depend on several underlying MLs positions via an axial-next-nearest-neighbor Ising (ANNNI) model [42], which has been successfully applied to the understanding of polytypism in SiC. Accordingly, in our NNN scheme, we write σ_{ijkl} as a sum of pseudo-spin pair interactions:

$$\sigma_{ijkl} = \sigma_0 - J_1 s_l s_k - J_2 s_l s_j - J_3 s_l s_i \tag{3.17}$$

where J_1, J_2 and J_3 are interaction parameters with the nearest, second and third neighboring MLs respectively. For III-V semiconductors with a stable cubic structure,J_1 must be large and positive, while J_2 and J_3 are negative and much smaller than J_1 [108]. Polytypic behavior is controlled by the J_1/J_2 ratio, which is about -14 for InP, compared to -0.5 for SiC [108], which explains why high order polytypes are rarely observed in III-V semiconductors.

Importantly, no solution can be found even if we allow J_1, J_2 and J_3 to vary, an approach adopted (omitting J_3) in Ref. [74], or including a higher order spin product, $-Ks_i s_j s_l s_k$. We conclude that an ANNNI-like interaction through the nucleus interface energy is not sufficiently rich to account for the correlations observed in our experiments.

3.6.3 Extending the ANNNI model to the step energy

The failure of the ANNNI model through σ leads us to propose that the step energy has a major role in conveying information about the underlying stack of MLs and hence we make Γ fully depend on it. However, we do not discard the stacking dependence on σ: instead of using the J_i as fitting parameters, we use recent *ab initio* values for the bulk (5.68, -0.40 and -0.38 meV/pair) taken from Ref. [12].

To account for this in a simple fashion, we first extend the ANNNI model to the step energy, in analogy with Eq. (3.17):

$$\Gamma_{ijkl} = \gamma_0 - K_1 s_l s_k - K_2 s_l s_j - K_3 s_l s_i \tag{3.18}$$

With this assumption, we have five unknowns, of which one is $\Delta\mu$. The value of $\Delta\mu$ is unknown, but surely positive and larger than all σ_{ijkl} and expected to be about 100 to a few hundreds meV/pair [3, 49, 52, 54]. We then assume a value for it and attempt a numerical solution of the system for γ_0, K_1, K_2 and K_3. However, we find no acceptable solution, because the resulting Γ_{ijkl} turn out to be negative or complex, irrespective of the value assumed for $\Delta\mu$.

To obviate this, we extend our ANNNI scheme for the step energy beyond pair interactions: we include in Eq. (3.18) the next term preserving symmetry (reversal of all spins) [23, 87], the 4-spin product $-K_4 s_i s_j s_k s_l$. The physical meaning of this additional term is simply that the step energy of a given nucleus, and hence the probability that it forms, depends on the nature of an underlying ML not only directly (as given by spin pair products) but also *via* the intermediate MLs. For example, from Table 3.2, we observe that the probability of a h nucleus is nearly independent of the NNN ML if the NN is h but not if it is c.

With this extra term, finding the values of the 4 parameters K_n from system (3.15) also requires setting a value for γ_0. We make conservative assumptions for the numerical solution, namely that $\Delta\mu$ lies in the range 50-300 meV/pair, and γ_0 between 0.1 and 1 J m $^{-2}$. The former value is slightly above the step energy in an In melt [70] (with Au in the liquid, we expect a higher γ_0) whereas the latter is of the order of the largest step energies proposed so far for III-V vapor-liquid-solid growth [3]. Within these ranges, solutions can be found with the following characteristics: the leading term K_1 never exceeds 20% of γ_0. The magnitude of K_n decreases with n and K_4 is one order of magnitude below K_1. Each K_n varies linearly with the assumed value of $\Delta\mu$ as long as it remains significantly larger than J_1, a condition surely met.

Even though the indetermination of $\Delta\mu$ and γ_0 precludes an absolute evaluation of the step energies, conclusions can be drawn about their ratios, which depend only weakly on these quantities. Let us choose a median value $\gamma_0 = 0.5$ J m $^{-2}$ and compute, for instance, the ratio $\Gamma_{h|hh}/\Gamma_{c|cc}$ of the step energies for the pure WZ and ZB phases. This ratio varies between 0.89 to 0.96 over our range of $\Delta\mu$. We thus find $\Gamma_{h|hh}$ to be close to, but smaller than, $\Gamma_{c|cc}$, the highest of all step energies. Hence, the model predicts that the step energy is responsible for the prevalence of WZ and for the strong intermixing, in agreement with the model of Ref. [52], but it is much richer, since it reproduces all the observed sequence frequencies.

3.7 Conclusions

In conclusion, on the basis of a detailed investigation of the structure of a NW with pronounced phase mixing, we have demonstrated that the stacking sequence is correlated and that the correlation extends at least to the next-nearest neighbor ML. The correlations between MLs are expressed via conditional probabilities for each type of ML (*h* or *c*) given the stacking sequence underneath. Classical nucleation theory has been used to model the growth process, showing that some form of interaction between the newly formed ML and the underlying MLs must be included. However, a quantitative agreement with the experiment has been obtained only by making the nucleus step energy to be stack-dependent, highlighting its key role in mediating the interaction. Because of its simplicity, we have proposed to extend the ANNNI model to quantitatively account for the dependence on the stacking sequence, but this choice is not unique and leaves the door open to more refined models.

Although we made no hypothesis about where nucleation takes place, we speculate that the observed correlations, peculiar to NWs, are easier to understand if nucleation occurs at the triple phase line bordering the NW top facet [52] (or possibly at the edge between the top facet and some truncation facet, which may exist in certain systems and growth conditions [45, 144], as we will discuss in the next chapter). In particular, in case of nucleation at the triple phase line, the structure and possible surface reconstruction of the NW sidewalls could explain a dependence of the edge energy of the nucleus on the positions of the two MLs underneath.

Chapter 4

Development of self-catalyzed GaAsP axial heterostructures

This chapter includes content from: G. Priante *et al.* Nano Lett. **15**, 6036 (2015) [119]

4.1 Introduction

In Chapter 1 we reviewed the interest, advantages, and challenges associated with the synthesis of axial heterostructures in self-catalyzed NWs. Despite the importance of obtaining axial heterostructures with precise thickness and compositional control, very few works have been devoted to this problem. This is even more surprising when we consider that the problem is potentially simpler than for other catalyst-assisted NWs, where the number of elements at play is larger.

In self-catalyzed III-V NWs, the number of necessary elemental fluxes is three, the third one being either another group III element or another group V element. As discussed in Section 1.5.1, the high solubility of other group III metals in Ga produces a marked reservoir effect which may prevent the fabrication of sharp heterointerfaces [86], although sometimes the results are better than expected, as for the compelling example that will be presented in Chapter 5.

In this chapter, we focus on the growth of self-catalyzed NWs using another group V element. We choose P to this purpose, since it is less soluble in Ga than all group III elements and even less soluble than As (at least at 600 ºC, which is the typical growth temperature) [6]. At supersaturation values expected during growth, the concentrations of both As and P should not exceed a few atomic percents [54]. The low solubility of these elements was already

shown to give abrupt interfaces in gold-catalyzed GaAs/GaP [15, 58, 72] and InAs/InP NWs. [14, 84]

$GaAs_{1-x}P_x$ NWs are also very promising for applications, thanks to the possibility to adjust their group V composition and thus the band gap over a wide range. $GaAs_{1-x}P_x$ is a direct band gap semiconductor up to $x = 0.45\%$ [18]. Moreover, pure GaP is almost lattice-matched to Si (0.37% misfit) and it has been shown to become a direct band gap semiconductor when the NW adopts the wurtzite crystal structure [9].

Nevertheless, very few studies have been devoted to the self-catalyzed growth of Ga(As)P in general [131, 132, 133]. The first report is by Tatebayashi et al. [132], who succeeded in growing GaP NWs by metalorganic chemical vapor deposition (MOCVD), after a predeposition of Ga droplets. Using a similar predeposition technique, Kuang et al. [83] reported the growth of GaP NWs by gas-source molecular beam epitaxy (MBE). Zhang et al. [149] reported the self-catalyzed growth of $GaAs_{1-x}P_x$ NWs by solid-source MBE on Si (111) substrates. However, all these works address the fabrication of homogeneous NWs or core-shell heterostructures and do not consider the formation of axial heterostructures. Holm et al. [68] demonstrated that it is possible to vary the composition of self-catalyzed $GaAs_{1-x}P_x$ NWs along the axis in a continuous fashion, with x ranging from 0.15 to 0.7, by adjusting the As/P flux ratio. The authors in Refs. [83] and [68] report that the direct supply of Ga and P fluxes leads eventually to the disappearance of the Ga nanoparticle, thus ending the VLS growth.

In the present work, a different approach is employed. First, we demonstrate that Ga-catalyzed growth of pure GaP NWs is possible in conditions similar to those required for GaAs NWs. Then we tackle the problem of fabricating GaP/GaAs heterostructures and carefully examine, with monolayer (ML) resolution, the composition profiles at the heterointerfaces. Flux interruptions are shown to be effective to obtain abrupt interfaces.

4.2 Growth of pure, self-catalyzed GaP nanowires

Our objective is to obtain axial NW heterostructures with sharp interfaces using Ga, As and P. From the application point of view, it is reasonable to have Ga(As,P) insertions surrounded by a barrier material with higher P content, since the bandgap of $GaAs_{1-x}P_x$ increases with x. In the limiting case, the barrier would be made of pure GaP, therefore it is interesting to investigate the synthesis of GaP NWs. As we have seen, the few papers describing the self-catalyzed growth of GaP NWs employ MOCVD or gas-source MBE, thus the growth parameters are not directly comparable with ours. Moreover, these papers do not explicitly show the presence of a liquid nanoparticle, though the high growth rates observed are a strong indication of a VLS growth mode, as the authors note. In our laboratory the self-catalyzed

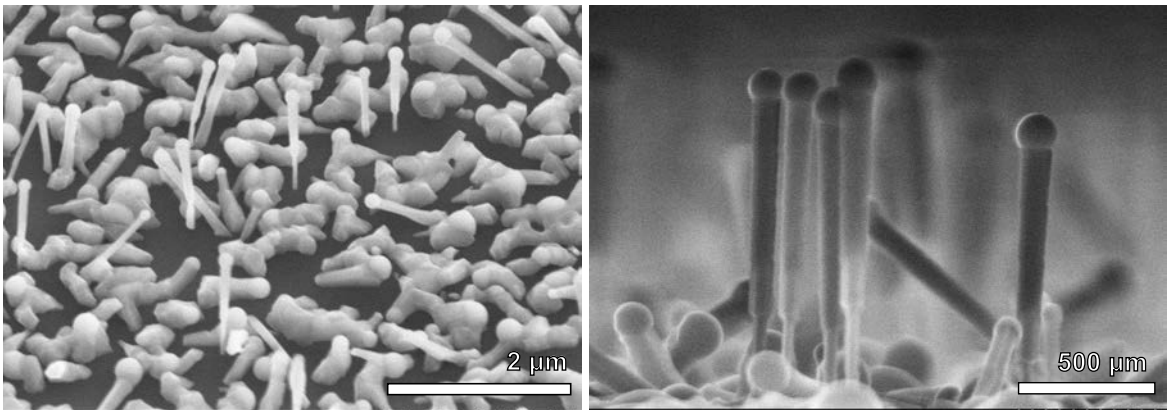

Fig. 4.1 SEM images of self-catalyzed GaAs NWs exposed to a GaP flux for 15 min. Left: 20º view of the sample. Right: cross-sectional view.

growth of GaP NWs was attempted but not realized, thus it is important to find the appropriate growth conditions for these NWs.

To avoid possible complications at the delicate NW seeding stage, the first trial we performed was to expose already-grown Ga-catalyzed GaAs NWs to both Ga and P for some time, keeping the same Ga flux as used to grow the GaAs stems. This sample is shown in Fig. 4.1, where GaAs is grown for 5 min in standard conditions (see Chapter 2), followed by GaP for 15 min. Both P flux and temperature were chosen in a conservative fashion, namely a P_2 BEP set to half of the As_4 one, and 590 ºC to reduce P volatility, while keeping at the same time a reasonable Ga diffusion length. The Ga flux is fixed at 0.2 nm s^{-1} (GaAs growth rate), as measured by RHEED oscillations during thin film growth, for all the experiments presented in this chapter.

As typically observed for GaAs NW growth at 590 ºC, the density of NWs, compared to the density of crystallites, is fairly low. The NW morphology clearly indicates that some overgrowth of GaP has indeed occurred, notably the abrupt diameter change and the pronounced inverse tapering (which is not present at this temperature and fluxes when only GaAs is grown). The presence of a large Ga nanoparticle at the top proves that the V/III ratio was low enough to produce a Ga-rich balance at the growth front. Thus we conclude that Ga-assisted growth of GaP is possible at the selected temperature and flux combinations.

The following step was to grow directly GaP NWs on Si(111). In analogy with the growth of self-catalyzed GaAs NWs, the native oxide layer on the wafer was not removed in order to promote the formation of Ga droplets. The Si(111) wafer, after degassing at 400 ºC for 30 minutes, was brought to 610 ºC and simultaneously exposed to Ga and P_2 vapors, using a P/Ga beam-equivalent pressure ratio (BPR) of 6. A cross-sectional view of this sample is given in Figure 4.2a, showing a good NW yield with droplets having a contact angle larger

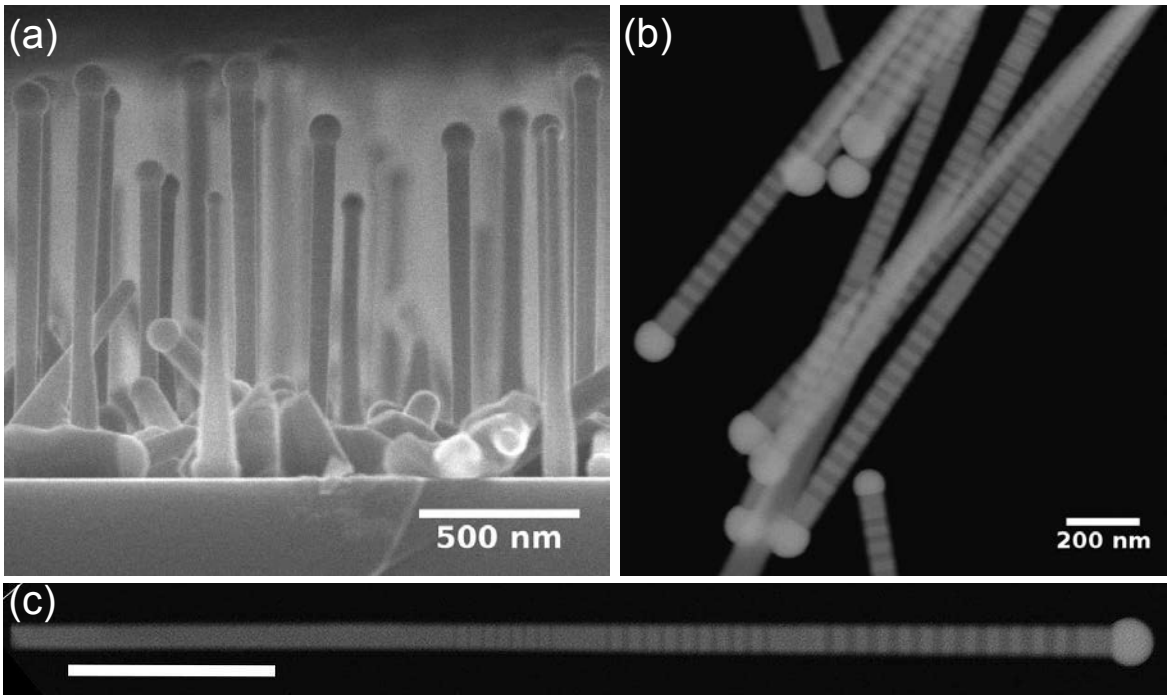

Fig. 4.2 a) Cross-sectional SEM image of pure GaP NWs grown on Si(111). b) HAADF STEM-SEM image of $GaAs_{1-x}P_x$ NWs from sample S, dispersed on a carbon membrane. c) HAADF STEM-SEM image of a single NW; scale bar is 500 nm.

than 130º, strikingly similar to those found for stable self-catalyzed GaAs NW growth [122].

Finally, we wanted to explore the temperature-flux window in which self-catalyzed GaP NW growth is possible. Since a full investigation of the GaP NWs growth parameters is not the scope of the present work, we limited the number of samples by testing selected temperature-flux pairs. We chose a "high" P/Ga BPR of 18 for growth experiments below 600 ºC and a lower ratio of 7 for the experiments above that temperature. This choice is justified by the fact that at high temperatures Ga desorption from the substrate becomes important and therefore the NW density is expected to decrease in accordance with the decreasing number of Ga droplets, in favor of the formation of crystallites.[1] In addition to 610 ºC, we tested the following temperatures: 570, 590, 640 and 670 ºC. In all cases, growth was performed for a duration of 15 min. SEM images of such samples are shown in Figure 4.3.

We observe that the number of features, both wires and crystallites, decrease when the growth temperature increases, at least at moderate BPRs. Growth at 590 ºC gave the best result, with well-defined, round Ga droplets at the top of the NW. The slight inverse tapering

[1] If P desorption was the limiting factor, we would make the opposite choice. In that scenario, however, we would expect to see the formation of droplets not giving life to NWs, which was not observed.

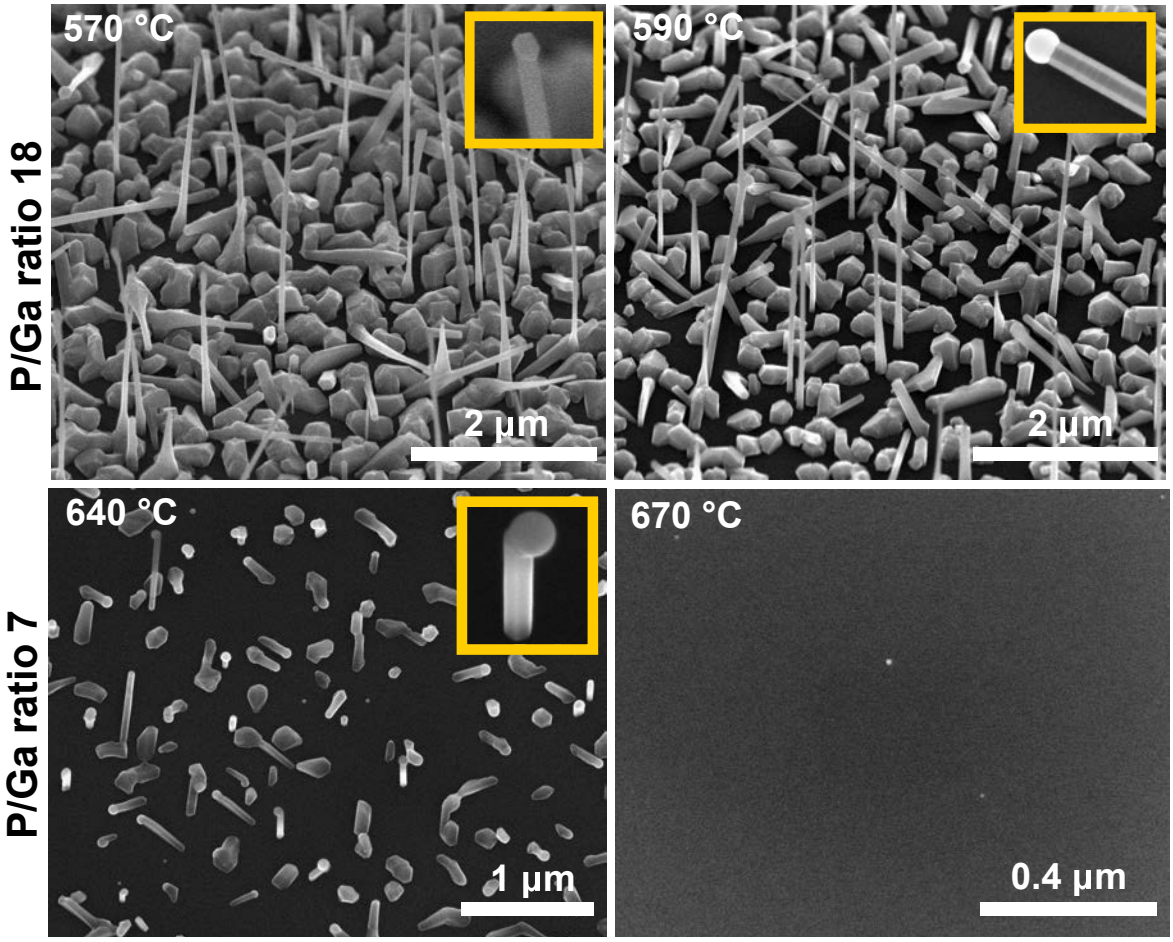

Fig. 4.3 SEM images of self-catalyzed GaP NWs for four different temperatures and two different P_2 fluxes. Tilt angle of the SEM images is 45º for the top row and 20º for the bottom row.

observed for BPR=6 disappeared. At 570 ºC the yield of NW is also good, but Ga droplets solidified into solid GaP (inset in the upper left panel of Fig. 4.3). This can be attributed to the decrease of the Ga diffusion length and increased supersaturation of the droplet (which increases when temperature is lowered). Growth should still be possible by lowering the P/Ga ratio. At the other side of the temperature window, we see that at 640 ºC the NWs are shorter than the ones grown at 610 ºC (despite the higher P flux) which indicates that the P supersaturation is reduced. The majority of NWs show sagging droplets. Finally, at 670 ºC neither crystallites nor NWs are observed, which indicates that the Ga adsorption on the substrate surface is zero. From these observations, we conclude that the growth of GaP NWs is surely achievable in the 590-610 ºC temperature range and for BPRs between 6 and 18. We note that these growth conditions overlap with those of self-catalyzed GaAs NWs. Such conditions will be used as a basis for our next experiments to produce GaP/GaAs heterostructured NWs. We stress that these are sufficient conditions and that GaP NW might grow for other temperature-flux combinations.

4.3 Growth of GaAs (GaP) insertions in GaP (GaAs)

In the next experiments, we investigate different growth recipes for the fabrication of abrupt GaAs/GaP and GaP/GaAs axial heterostructures. Samples are assigned letters (S, V, VI, VLI) which index the different procedures used to fabricate the GaAs (GaP) insertions in the GaP (GaAs) NWs. The complete list of samples is given in Table 1.

The first sample was grown by selecting As and P fluxes that produce similar NW growth rates for the two binary compounds.[2] In our system, this is obtained for a P/As BPR of 7/10. The As and P fluxes were commuted by operating simultaneously the individual shutters of both As and P effusion cells without valve actuation (sample S, for shutters). It is important to note that in MBE, the sole actuation of the individual shutter is not enough to interrupt completely a group V flux. This is related to the relatively high vapor pressure of these elements which have a sticking coefficient much lower than one, even if the absorbing surface is cryogenically cooled. As a result, the shutter cuts off only about 90% of the flux (this point will be discussed in Section 4.4). The structure consists of a GaAs stem about 1 μm long, followed by three series of GaP insertions. Each of these series contains a different number of insertions grown for different times: 8 x 5 s, 10 x 10 s and 12 x 15 s. All insertions are separated by a GaAs segment grown for 15 s and the series are separated by GaAs segments grown for 30 s. Such structure allows for the unambiguous identification of each series in the

[2]We calculate the growth rate of each pure binary by dividing the NW length (as measured from SEM images) by the total growth time.

following analysis. The STEM-SEM contrast in HAADF mode reveals the compositional modulation of the NWs, which itself reflects the change of As/P flux ratio (Figure 4.2b,c). Quite generally, the higher the intensity, the larger the As concentration.

The analysis of the samples was carried out by scanning transmission electron microscopy (STEM) in the high-angle annular dark field (HAADF) mode, both in a scanning electron microscope (SEM) and in a transmission electron microscope (TEM). The NWs have a hexagonal shape limited by six {110}-type facets. In the following TEM observations, the electron beam is always oriented along a <110> zone axis, i.e. perpendicular to two sidewalls of the NW. HAADF intensity profiles along the <111>B growth direction were extracted by averaging the signal laterally over the width of the flat facet. In order to obtain quantitative information on the composition profiles, we used high resolution HAADF TEM images. As seen in Chapter 2, the ratio R between the HAADF intensities in two regions of different compositions can be expressed as:

$$R = \frac{I}{I_0} = \frac{xZ_{\mathrm{P}}^{\alpha} + (1-x)Z_{\mathrm{As}}^{\alpha} + Z_{\mathrm{Ga}}^{\alpha}}{x_0 Z_{\mathrm{P}}^{\alpha} + (1-x_0)Z_{\mathrm{As}}^{\alpha} + Z_{\mathrm{Ga}}^{\alpha}} \tag{4.1}$$

In this phenomenological equation, I and I_0 are the intensities relative to regions of compositions x and x_0 respectively (after subtraction of the dark counts), and Z_i is the atomic number of species i. α is a fitting parameter accounting for deviations from pure Rutherford scattering. Eq. 4.1 can be used to estimate the composition of NW sections, after the composition x_0 of a reference zone of intensity I_0 has been calibrated by energy-dispersive X-ray spectroscopy (EDX). We determined α by converting the HAADF intensity profile of a periodic heterostructure into a composition profile which fits EDX composition measurements of the same heterostructure (Figure 4.4a). The reference I_0 was taken in the GaAs stem. For our experimental conditions, the best value of α is 1.4.

In Figure 4.4b, the method is applied to an atomically resolved image of an interface between sections of different P content, to infer the composition x of each single ML. Because each HAADF oscillation corresponds to a III-V ML, as a first approach, we assigned to each ML the HAADF intensity averaged over one oscillation. This simple method allows to measure the composition profile across NW heterostructures with atomic resolution.

Figure 4.5 reveals rather broad interfaces in sample S, for which the As/P alternations are performed by closing and opening simultaneously the individual shutters. The transition lengths are about 15 MLs thick for As-rich to P-rich interfaces, and 10 MLs thick for P-rich to As-rich interfaces. The lengths of the transition regions are independent of the thickness of the insertion.

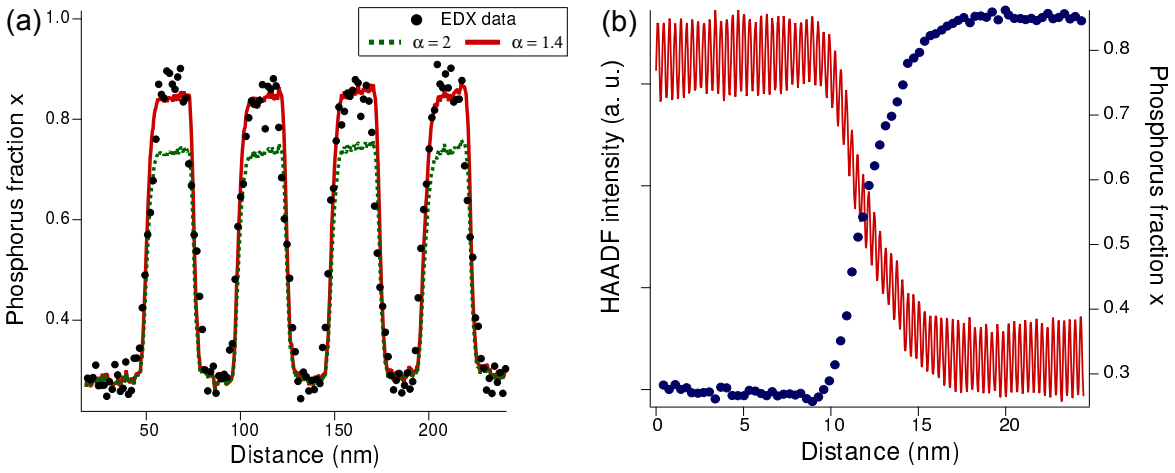

Fig. 4.4 a) Comparison between the composition calculated from Eq. 4.1 and the EDX data from a medium-resolution image of sample S, using either $\alpha = 2$ (dashed green line) or $\alpha = 1.4$ (full red line); b) Atomically-resolved HAADF intensity profile (full red line) and the corresponding composition profile (blue dots) estimated for each monolayer using Eq. 4.1 with $\alpha = 1.4$.

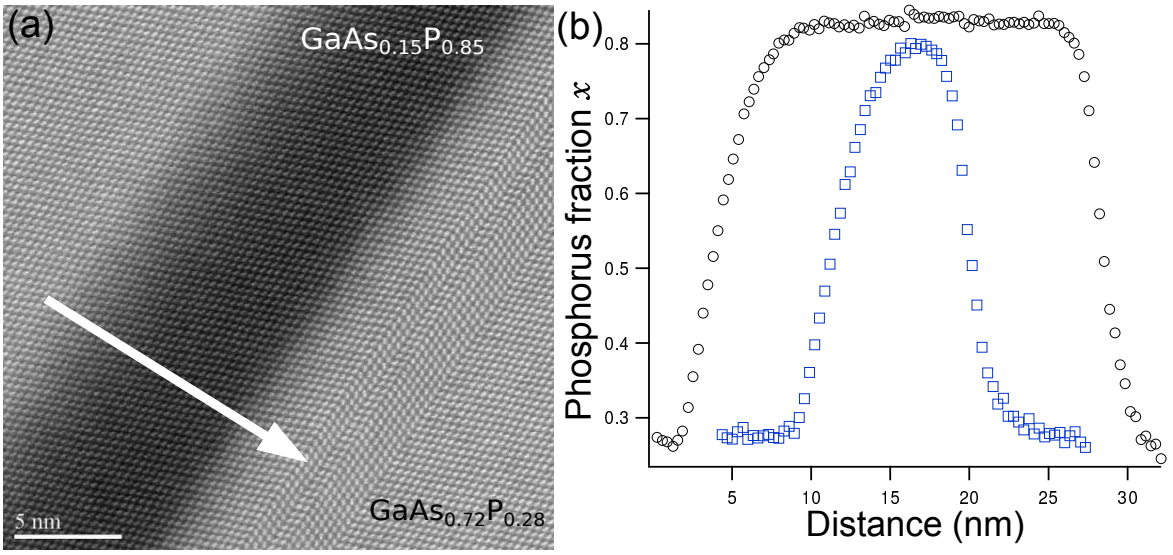

Fig. 4.5 a) HAADF TEM image of heterointerfaces of a 5 s insertion in sample S. The arrow indicates the growth direction; b) Compositional profiles along the growth direction extracted from HAADF intensity for insertions grown for 5 s (blue squares) and 15 s (black circles).

Table 4.1 List of samples.

Sample	S	V	VI	VLI
Main material	GaAs	GaP	GaP	GaP
Insertions	GaP	GaAs	GaAs	GaAs
P/Ga BPR	7	7	7	15
As/Ga BPR	10	11	11	15
Group V switch using	Shutters	Shutters and valves	Shutter, valves, main shutter	Shutter, valves, main shutter
Flux interruption	No	No	20 s	60 s

The sharper P→As interface can be explained by a shorter P depletion time from the droplet, related to its lower solubility in the catalyst and to its higher evaporation rate as compared to As [16, 49]. For sample S, the significant amount of P (~28%) in the GaAs sections and of As (~15%) in the GaP sections is understood by recalling that the shutters are not capable of blocking the fluxes completely (see also Section 4.4).

In the next sample (V, for valves) we grew GaP NWs with GaAs insertions. To limit as much as possible the background fluxes, we commuted between As and P by closing the valves (as well as the shutters) of the group V cells, which are more effective than shutters but slower to operate (about 1 s compared to 0.1 s). Sample V consists of nominally pure GaAs insertions grown for different times (5, 10 and 15 s), each of these repeated 5 times, embedded in a nominally pure GaP NW grown at BPR=7.

We also grew sample VI (for valves and interruptions), a variant of sample V for which *all* fluxes were stopped during 20 s at each interface. The main shutter was also closed, as a further shield for the NWs against the volatile group V species.

Finally, we grew sample VLI (for valves and long interruptions), another variant of sample V. Sample VLI is grown at a slightly lower temperature (590°C) and higher BPR=15 for both As and P, to obtain thinner wires (around 50 nm in diameter as opposed to 100 nm for the other samples)[3] and a longer flux interruption of 60 s was introduced.

Of interest is the peculiar crystal structure of these samples. The structure of pure GaP NWs and all $GaAs_{1-x}P_x$ segments in sample S resulted to be pure zincblende, affected only by twinning. The density of twins varied greatly with the concentration of P, being lowest for compositions close to the pure binaries. A similar trend was reported in Ref. [149]. Surprisingly, we note that all GaAs insertions of samples V, VI and VLI, possess the wurtzite structure (Figure 4.6), whereas self-catalyzed GaAs NWs tend to be either mixed

[3]Right at the formation of the NW, the Ga droplet is exposed to a direct Ga flux and to an indirect contribution from surface diffusion on the substrate. Lower BPRs, and therefore lower elongation rates, enhance droplet inflation at the beginning of growth, resulting in larger diameters.

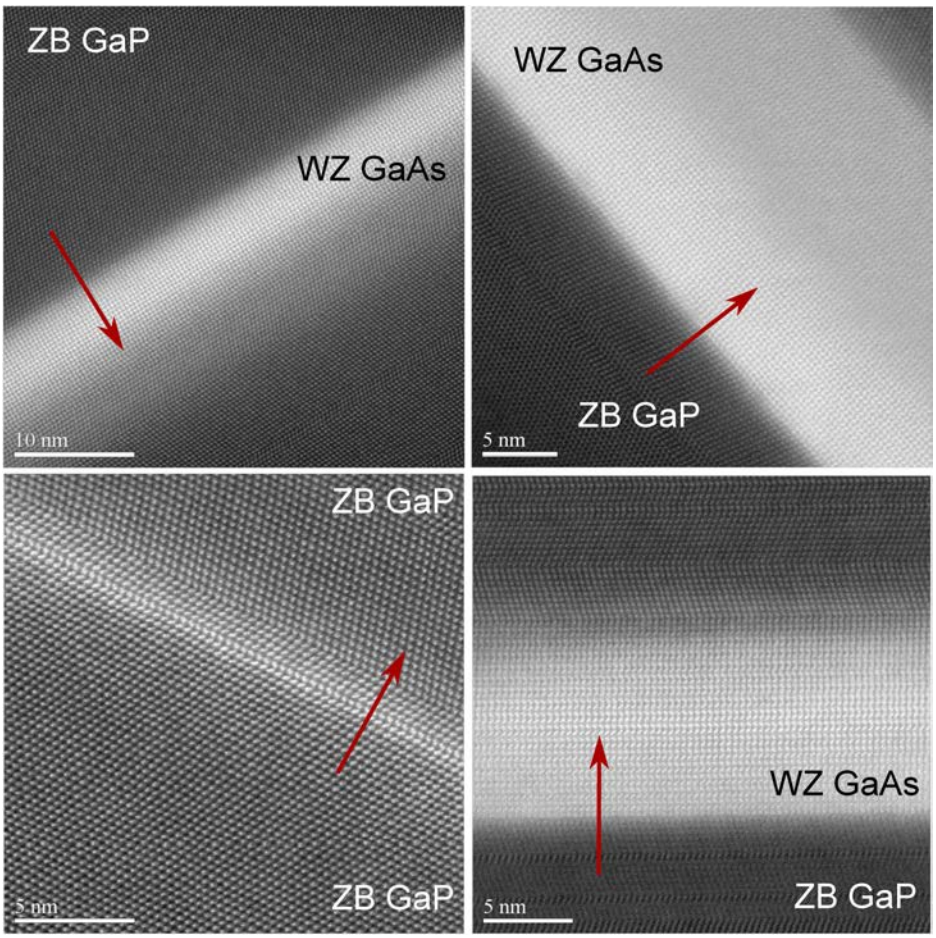

Fig. 4.6 WZ GaAs insertions for different samples and thickness. Clockwise, from the top left: 5 s insertion in sample V; 15 s insertion in sample VI; 15 s insertion in sample VLI; 5 s insertion is sample VLI. Red arrows indicate the growth direction.

wurtzite/zincblende [129] or pure zincblende crystals [24, 120]. However, we have not investigated the reason of this unexpected behavior.

Let us now focus on the interfaces. In Figure 4.7a, we compare the interface sharpness measured on atomically resolved HAADF images of samples V, VI and VLI. Flux interruption remarkably improves the abruptness of the GaP→GaAs interface. Indeed, the width of the transition region decreases from 15 to 2 MLs between samples V and VLI.

The situation is more complicated for the GaAs→GaP interface. We observe that the isointensity lines, which are normal to the <111>B growth axis in the central portion of the NW, curve near the NW periphery (Figure 4.7b). Recall however that HAADF profiles were extracted from the central portion of the image (which corresponds to the flat sidewall facet). There, along the NW axis, the HAADF intensity, and therefore the As concentration, also

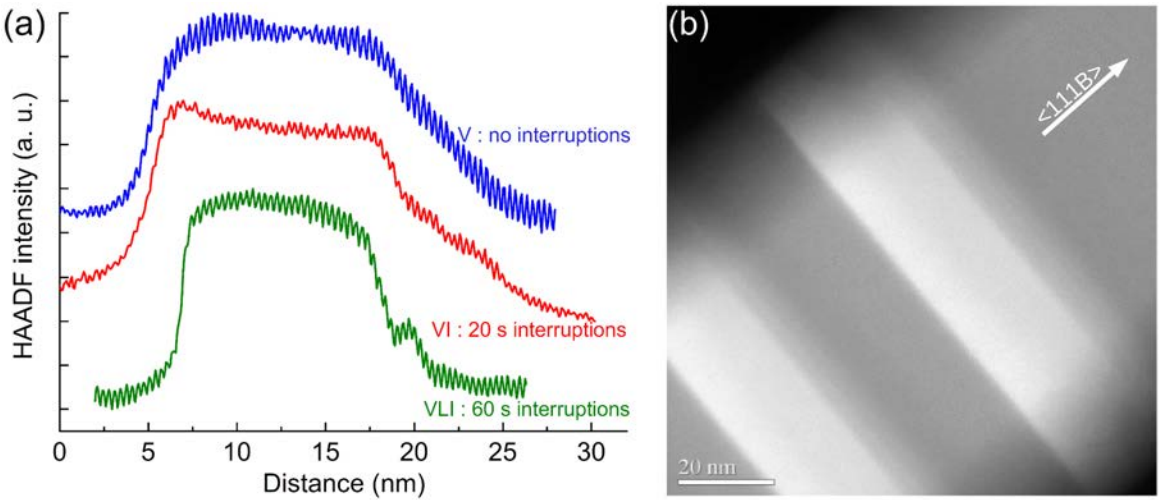

Fig. 4.7 a) Comparison of the HAADF intensities in the case of flux interruptions of 0, 20 and 60 s, for GaAs insertions grown for 10 s; b) Detail of interfaces for GaAs insertions grown for 10 s in sample VI.

decreases more abruptly with increasing flux interruption time, but on the other hand a tail appears, about 30 MLs long.

Why this long transition region exists and why the interface has an irregular shape is unclear at present. Bearing in mind that, due to limited specimen tilt available in our microscope, the three-dimensional geometry of the insertion cannot be fully deduced from our two-dimensional TEM images, we speculate that two scenarios are possible: i) the GaAs insertion grows with a tapered shape and, due to the reservoir effect, the GaP that subsequently covers and surrounds it incorporates a certain amount of As; ii) part of the GaAs insertion gets dissolved back into the droplet during the flux interruption and the As so liberated redeposits when growth is resumed, this time mixed with P.

Whatever the actual mechanism, it is likely that a non-flat interface, which we always observe to have roughly similar shapes, extends all around the NW. If this is the case, the electron beam traverses an As-rich core and a shell poorer in As, so that the measured As composition is lower than that of the core. Notwithstanding these complications, it is clear that flux interruptions are beneficial in purging the catalyst droplet as well as the residual P vapor in the chamber: EDX analysis shows a decrease of the average P content in the GaAs insertions from $x = 0.10$ to $x = 0.05$ between 0 and 20 s flux interruptions, as measured in the thick (15 s) GaAs segments. However, the residual P content is still significant, which suggests the presence of a source of P *other than* the reservoir effect in the droplet. Yet the effect of the As background on the NW composition is less detrimental: the residual

As concentration in the nominally pure GaP sections never exceeds 1%, according to EDX measurements, a value comparable to the detection limit of the method.

4.4 Behavior of As and P fluxes

In order to investigate the probable accumulation of the group V vapors in the chamber suggested by the results of Section 4.3 and the effective duration of flux transients, we performed dummy growth experiments with an ion gauge replacing the substrate. The ion gauge output current was acquired through an analog-digital converter and sent to the computer for data storage. The current was sampled every 50 ms, fast enough to resolve the transients of interest. In all cases, the Ga cell was kept at standby temperature,[4] and at the beginning of the experiments the pressure measured from the ion gauge was about 1×10^{-10} Torr or lower. We recorded separately the fluxes of both As and P for each experiment presented in this section.

In Figure 4.8, the As and P beam equivalent pressures (BEPs) for sample S are shown (note the logarithmic scale). For both species we see that, whenever the shutter is open, the flux provided is reproducible and constant throughout the experiment. A small increase of the P flux just after the shutter closure is also observed (red curve in Fig. 4.8), which we attribute to the re-evaporation of P condensed in the cracker tube and on the chamber walls around the cell orifice. Re-evaporation is probably caused by the heat reflected by the shutter.

As stated previously, the shutters are not efficient to stop completely the fluxes: from Figure 4.8, we see that the efficiency[5] is actually around 90% for As and only 60-70 % for P. By evaluating the time derivative of the signals in Fig. 4.8, we see that the slopes change abruptly, which indicates that the shutter operation time is comparable with our temporal resolution of 0.05 s. It is clear that the flux transients related to the opening and closing of shutters are negligible compared to the transition time in which both P and As pressures equilibrate with the rest of the MBE system. In sample S, the latter varies between 1 and 2 seconds.

Since the NW growth rate of self-catalyzed NWs is set by both group V species, it is likely not constant during interface formation and cannot be measured directly. However, from Figure 4.5 we can infer that the insertion growth rate for sample S is about 1.5 nm s^{-1}, which implies that some 1.5 nm (or 5 MLs) of compositional gradient are due to the non-abrupt change of the As/P ratio. Moreover, note that for this sample the As pressure

[4] That is, no flux is emitted from the Ga effusion cell.

[5] Defined as one minus the ratio between pressure with shutter closed and pressure with shutter open.

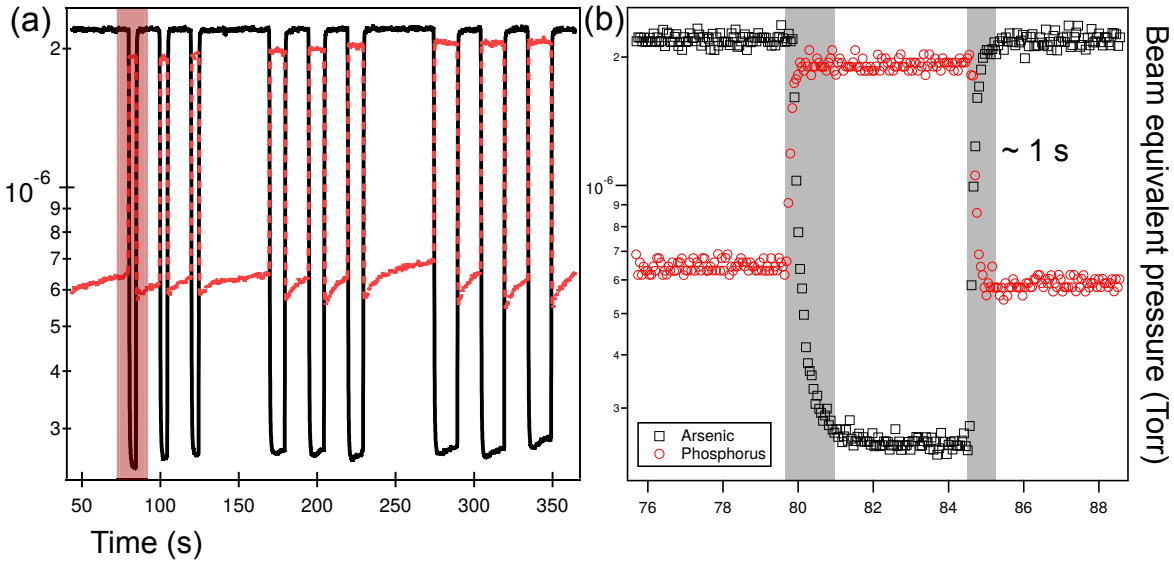

Fig. 4.8 Measured fluxes of sample S (shutters only), expressed in terms of beam equivalent pressure. a) Overview of the flux profiles for the whole sample. The red stripe indicates the region reproduced in the left panel; b) detail of the P and As flux evolution when the shutters are alternated for 5 s (thin insertions), the grey stripes indicate the transition regions between the stationary values. The spacing between each point is 50 ms.

takes almost 2 s, twice the time compared to P, to reach its stationary value when the shutter is closed (Fig. 4.8b). This would imply a larger interface thickness when going from As-rich to P-rich than vice versa, which is consistent with our observations.

Let us now take a look at the situation when the P-As switch is performed using valves in conjunction with the shutters. In Figure 4.9a, the flux profiles for 10 s insertions in sample V are shown. Again, from the panel on the left we see that the flux modulations are well reproducible. The pressure excursion between valleys and peaks for both materials is one order of magnitude greater than for sample S, which enhances the compositional difference between the insertions and the rest of the NW. However, since the chamber is pumped at (an approximately) constant speed, the transients are longer. As will be shown in Chapter 6, group V fluxes of the order of 10^{-7} Torr are sufficient to promote growth in self-catalyzed NWs. To reach a residual flux of 10^{-8} Torr, 10-20 s are generally necessary, depending on whether the main shutter is used or not. This is also consistent with the fact that flux interruptions of 20 s or less are rather ineffective for improving interface abruptness.

From the right panel in Figure 4.9b, we analyze in more detail a typical P flux profile when valves are used. When the shutter is opened, a residual flux is emitted, supporting the hypothesis of material accumulation behind it, followed by a sharp increase after approxi-

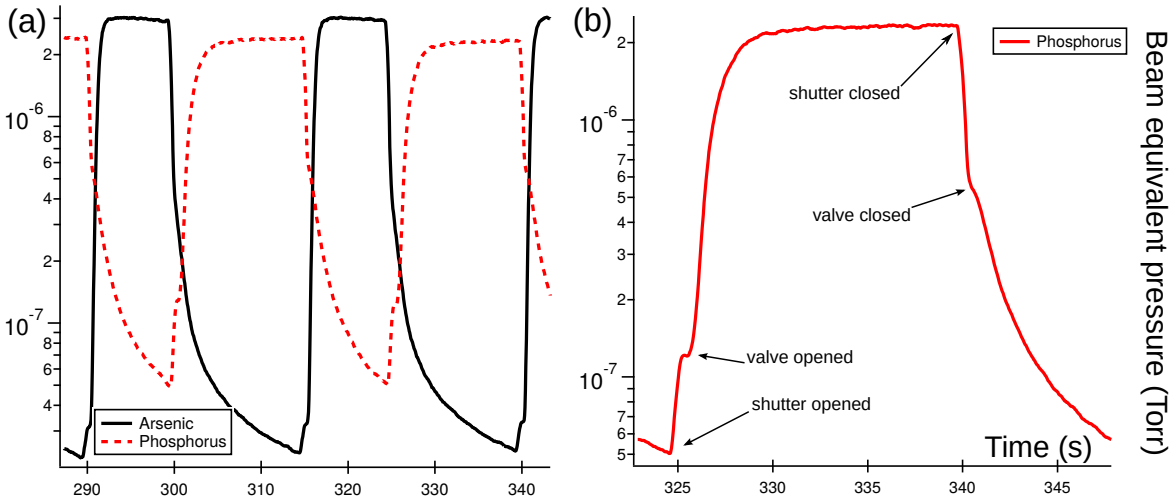

Fig. 4.9 Measured fluxes of sample V, expressed as beam equivalent pressures. Left: detail of flux transients during the growth of 10 s insertions. Right: detail of the evolution of P flux for a complete shutter and valve opening-closing cycle.

mately one second. Since the valve takes about 1 s to open completely, we can associate the second change in slope to the fully open valve.

From the above analysis of the flux profiles, we conclude that another type of reservoir effect, due to the growth chamber itself, is present and it is very likely to affect strongly the NW composition profiles. This hypothesis is consistent with the fact that the sharpness of the interfaces improves and residual contents of P in GaAs insertions decrease with increasing flux interruption time. Group V vapor accumulation appears to be a machine-related problem and an MBE-specific one. In fact, a group V background pressure is detrimental in planar MBE of III-V-V heterostructures as well. However, this effect is somehow amplified in self-catalyzed NWs by the large collecting surface of the droplet compared to the size of the growth front: the ratio between the areas of these two surfaces is about 6, for a typical droplet contact angle of 130°. The problem for NWs may be significantly mitigated by lowering the absolute value of the fluxes and thus the growth rate, both of which are beneficial for the quality of the interfaces. Growth at lower rates will be explored in Chapter 6.

4.5 Morphology of the growth front

Finally, we focus on the morphology of the GaP→GaAs interfaces. Figure 4.10 shows images of the thin (5 s) insertions in the case of 0 s and 60 s flux interruptions. In Fig. 4.10a,b (samples S and V), we note that the GaP→GaAs interface is flat from side to side, i.e. from the edge between two {110} sidewalls tilted with respect to the electron beam, to

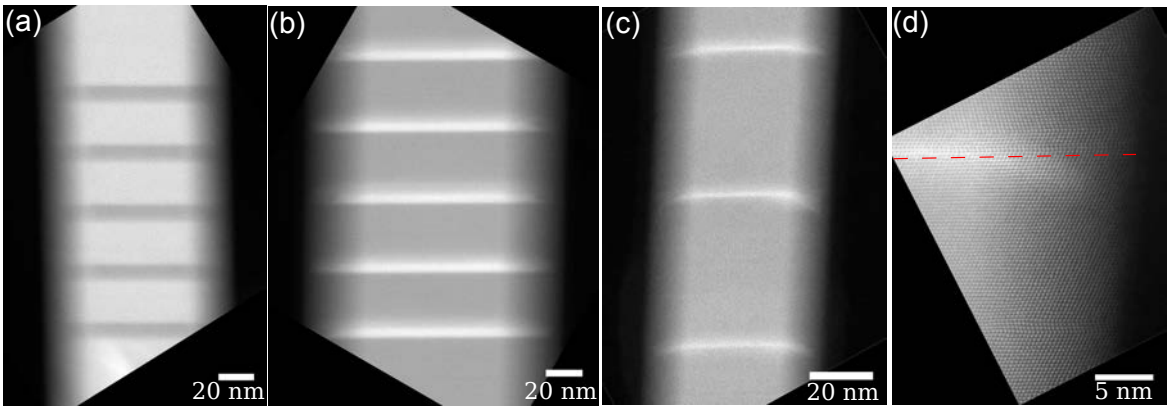

Fig. 4.10 Morphology of the thin insertions. The growth direction points upwards. a) No flux interruptions (sample S); b) No flux interruptions (sample V); c) 60 s flux interruption (sample VLI); d) close up from panel (c), the (111) plane at the beginning of the GaAs insertion has been marked by a dashed red line as a guide to the eye.

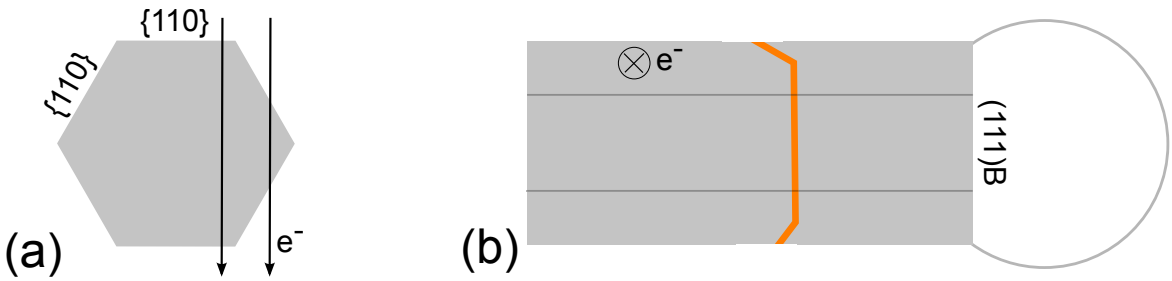

Fig. 4.11 Typical geometry of NW observation by TEM. NWs tend to adhere to the grid on one of the six {110} sidewalls, making them easy to observe along a <110> zone axis. a) Cross sectional view: the amount of material traversed by the electron beam, and therefore the HAADF intensity, decreases when moving towards the edges. b) Top view: schematic representation of the non-planar shape of thin GaAs insertions obtained with long flux interruptions.

the opposite one, as depicted in Fig. 4.11 (near these edges, the NW gets thinner so that the HAADF intensity decreases). By contrast, in Fig. 4.10c,d (sample VLI), the GaP→GaAs interface is not flat but show small truncation facets on the edge, as marked by the GaAs layers. The occurrence of such truncated interfaces is systematic in all samples for which flux interruptions were performed.

Thanks to the contrast of HAADF images, we are able to tell that the composition of the material grown on the top (111)B facet and on the truncation facets is similar, which indicates that the whole NW top was covered by the Ga droplet at the moment of the insertion formation. This is a clear *ex situ* observation of truncation facets, which occurrence in various types of NWs was already observed by *in situ* TEM experiments [45, 101, 144].

Knowledge of the shape of the growth front during growth is of tremendous importance for the understanding of NW growth mechanisms. Importantly, the shape can influence the position of the vapor-liquid-solid boundary (also referred to as the triple phase line) where preferential nucleation may take place. As seen in Chapter 1, this also has consequences on whether the new nucleus will be formed in hexagonal or cubic position, thus affecting crystal phase selection.

In the specific case of GaP NWs, Ref. [144] reported that truncation facets exist at all times during in situ TEM growth by chemical vapor deposition. Here, we show that the appearance of truncation facets actually depends on the growth conditions. In conditions that give NW growth rates of 1-2 nm s^{-1} (those used in this work, typical of standard MBE), we expect the concentration of group V elements in the droplet to be several times above the equilibrium concentration [54]. In such conditions, we never observe any truncation facet. If they exist (a possibility that we allow for because of the reduced signal coming from the NW edges) their lateral length should not exceed a few atomic spacings. On the other hand, when flux interruption is applied, the concentration of group V elements drops quickly because of residual growth and evaporation, approaching the equilibrium value. Between these two limit conditions, the system passes through an intermediate state, which corresponds to a condition of low supersaturation, and the interface truncation forms.

To summarize, while it is clear that the crystal equilibrium shape is most often faceted, the present observations show that the size of these truncation facets depends on the level of supersaturation. The present analysis might explain why truncation facets are often observed in TEM growth experiments, where the pressures of the precursors are limited by the microscope design. At typical pressures employed in these experiments, growth rates are of the order of 0.1 nm s^{-1} or even less, which corresponds to supersaturation values lower than in our experiments. However, the situation is further complicated by the composition of the droplet, which in most in situ experiments contains also a foreign metal, typically gold, which affects surface and interface energies as well.

4.6 Conclusions

In summary, in this chapter, we have shown that the stable, self-catalyzed, vapor-liquid solid growth of GaP NWs can be achieved by MBE. We have explored the optimal growth conditions for these NWs and found that they overlap nicely with those used for GaAs NWs. This enabled us to fabricate axial heterostructures of both ternary-ternary Ga(As,P) and quasi-binary GaAs and GaP sections.

The quality of the interfaces was assessed with monolayer resolution. We demonstrated that their abruptness can be greatly improved by flux interruptions, down to only two monolayers for the GaP/GaAs interface. Through accurate flux measurements, we found that the reservoir effect associated with accumulation of P (or As) in the droplet is not the main factor deteriorating interface abruptness, but that the growth chamber itself acts as a gaseous reservoir. Long growth interruptions are effective in improving the compositional control, but also lead to collateral problems such as dissolution of the grown material, faceting of the growth front, change of crystal structure and, potentially, to an increased incorporation of contaminants. Lowering the absolute fluxes of group V species, and with them the NW growth rate, is suggested as a strategy to mitigate this problem in MBE systems, reducing the overall background pressure and thus the time necessary to purge the growth chamber.

The study of the interfaces also provided insight on the dependence of the growth front shape on growth conditions. In particular, we showed that truncation facets can be formed under the droplet in a condition of low supersaturation, when the feed fluxes are interrupted for some time. The observation of a constantly flat interface, when insertions are grown at standard growth rates, rules out the possibility that truncation facets of appreciable size are present at all times during growth. Given the importance of knowing where the nucleation takes place for the modeling and understanding of growth mechanisms, notably polytypism, this will surely be object of further investigations.

Chapter 5

(Al,Ga)As axial heterostructures

This chapter includes content from: G. Priante *et al.* Nano Lett. **16**, 1917 (2016) [117]

5.1 (Al,Ga)As insertions in self-catalyzed GaAs NWs

In Chapter 1, Section 1.5.1, we have seen that the main obstacle to the synthesis of sharp heterointerfaces is the accumulation of one or more species in the liquid catalyst, known as the reservoir effect. Starting from the assumption that the solubility in Ga of group V elements is generally low and, in any case, much lower than that of group III metals, in the previous chapter we explored the self-catalyzed growth using both P and As to fabricate binary and ternary heterostructured NWs. Surprisingly, we found that the advantage of using group V elements was partly mitigated by their high vapor pressure, making abrupt interfaces difficult to achieve in a conventional MBE system.

On the other hand, while group III elements do suffer from high solubility in the droplet, their vapor pressure in standard growth conditions is negligible. As opposed to group V species, a shutter is sufficient to interrupt the flux rapidly and completely. When a III-III-V heterostructure is desired, the choice of the second group III material is limited mainly to Al and In. One report deals with the synthesis of self-catalyzed InGaAs NWs [65] but pointed to a non-optimal control of the composition, caused by low incorporation of In via the droplet.

To the best of our knowledge, there is presently no report that studies the formation of (Al,Ga)As heterostructures in NWs obtained by the self-catalyzed vapor-liquid-solid method. The $Al_xGa_{1-x}As$ system is of particular interest, thanks to the negligible mismatch between the end-point binaries that allows one to fabricate defect-free NW heterostructures over the whole composition range. Moreover, the electronic, mechanic and thermodynamic properties of this system are well known and a large amount of data is available in the literature. Nevertheless, few reports deal with the formation of axial GaAs/(Al,Ga)As heterostructures

in NWs in general [22, 59, 60, 64, 134], and even fewer address the problem of interfaces [102].

In this chapter, the growth of ternary (Al,Ga)As insertions in self-catalyzed GaAs NWs is investigated in depth, and the composition and abruptness of interfaces are analyzed with monolayer (ML) precision. A quantitative model is proposed, describing the shape and composition of the interfaces, and giving hints to make them sharper.

5.2 Experimental details

The self-catalyzed growth of heterostructured GaAs/(Al,Ga)As NWs was carried out by solid-source MBE between 590 and 610 ºC. Ga and Al fluxes were kept fixed and equivalent to two-dimensional deposition rates on GaAs (001) of 0.20 and 0.08 nm s^{-1} respectively, as deduced from reflection high-energy electron diffraction oscillations. The As flux, which governs the steady-state growth rate of self-catalyzed NWs [27, 54, 120], was set to produce an average NW growth rate of 1.6 nm s^{-1}. Growth was performed on undoped Si (111) wafers degassed in ultrahigh vacuum at 400 ºC for 30 min, without removing the native oxide. Growth was initiated by supplying Ga and As simultaneously and continued for 15 min to form a GaAs stem about 1.5 µm long. In order to create $Al_xGa_{1-x}As$ insertions, Al and As were supplied for different durations, either simultaneously or separately[1].

Three main samples were studied:

- Sample A: (Al,Ga)As insertions of various thickness were grown by opening the Al shutter for different durations, all other parameters unchanged;
- Sample B: similar to sample A, but the As flux was reduced to approximately 10% of its standard value during heterostructure formation. As shown in Chapter 4, this reduction of As flux is obtained almost instantaneously by closing the As shutter;
- Sample C: the As flux is interrupted completely for some time before heterostructure growth. The composition of the droplet is modified by supplying Al alone, a procedure we refer to as droplet *pre-filling*. GaAs growth is then growth is resumed in standard conditions.

The samples were observed in a scanning transmission electron microscope (STEM) in the high-angle annular dark field (HAADF) mode. The NWs predominantly crystallize in the zinc-blende structure and exhibit a hexagonal shape limited by six {110} sidewalls. In

[1] Ga was not supplied for the short time of heterostructure formation, to prevent excessive inflation of the droplet when low As fluxes are used.

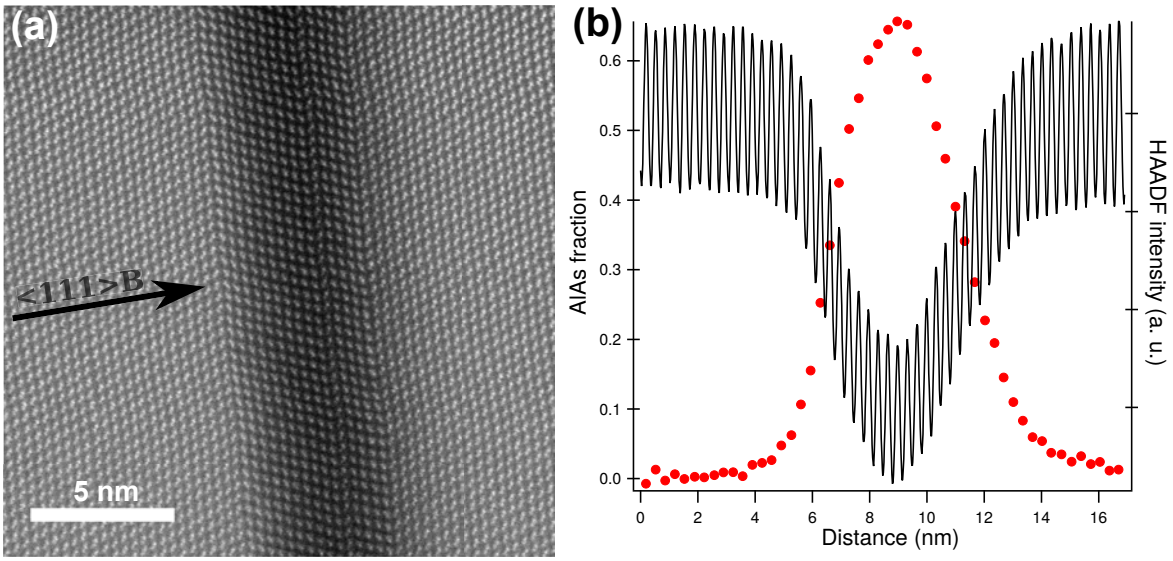

Fig. 5.1 a) High resolution HAADF image of an (Al,Ga)As insertion in a NW; b) Composition profile (red dots) calculated from the HAADF intensities in panel a) using Eq. 2.3.

the following STEM observations, the electron beam is oriented along a <110> zone axis, i.e. perpendicular to two sidewalls of the NW. HAADF intensity profiles along the <111>B growth direction were extracted by lateral averaging over the width of the flat facet (Figure 5.1a).

Compositional profiles with ML resolution were obtained according the procedure described in Section 2.2.3 and illustrated in the previous chapter. Eq. 2.3 was calibrated by performing a comparison with EDX data obtained from a thick and homogeneous AlGaAs section from sample A, giving $\alpha = 1.7$.

5.3 Abruptness of interfaces

We first consider sample A, which contains (Al,Ga)As insertions grown by supplying Al and As fluxes for short times. The HAADF images and composition profiles shown in Fig. 5.2 correspond to a single insertion grown for 20 s (Fig. 5.2a,b) or multiple insertions grown for 5 s each (Fig. 5.2c,d).

From the composition profile in Fig. 5.2b, we observe that the Al content in the solid saturates at $x \simeq 0.1$, although we provide only Al and As. This will be clarified by the model developed later. The transition width is of the order of 10 MLs for both the GaAs→(Al,Ga)As and (Al,Ga)As→GaAs interfaces, independently of the thickness of the insertion. We may compare the widths of such interfaces with the values reported by Ouattara et al. [102] for gold-catalyzed NWs grown by metalorganic vapor phase epitaxy at 630 ºC. These authors

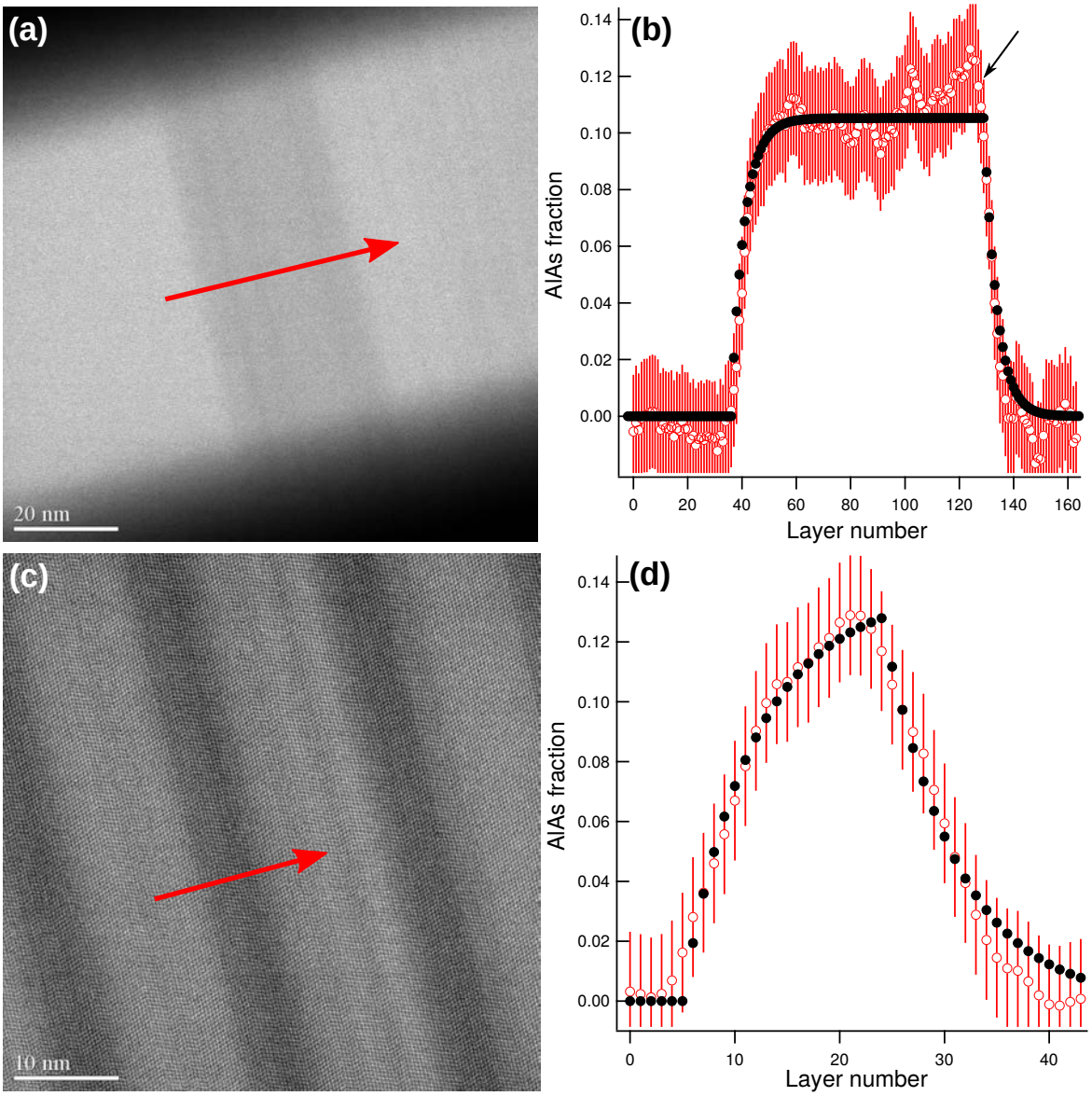

Fig. 5.2 a) HAADF image of an (Al,Ga)As insertion grown for 20 s in a NW from sample A; b) Composition profile (red circles and error bars) calculated from the HAADF intensity in panel a), compared with the results from the model (black dots) described in the text. The black arrow indicates the onset of the AlAs fraction decrease; c) HAADF image of a series of (Al,Ga)As insertions grown for 5 s in sample A; d) composition profile compared with the model, for a single insertion grown for 5 s. Red arrows indicate the <111>B growth direction, along which the profiles are extracted.

grew a homogenous section of $Al_{0.1}Ga_{0.9}As$ in a GaAs NW, thus with the same solid composition as in our experiment. While the GaAs→(Al,Ga)As interface is reported to be atomically sharp, the (Al,Ga)As→GaAs tail is in excess of 50 nm (∼150 MLs), i.e. much wider than in our experiment.[2] This observation suggests that the relative amount of Al accumulated in the Au droplet, hence the stationary Al concentration, is higher than in Ga. Given that the growth temperature in Ref. [102] is only slightly higher than ours, we speculate that it is gold itself promoting the accumulation of Al in the droplet. In the next section, we try to quantify such stationary Al concentration for sample A.

5.3.1 Estimation of Al fraction in the liquid

If we make the assumption that all Al entering the droplet eventually incorporates into the solid, we can get an indication of the Al fraction in the liquid, y_{Al}. The assumption is justified by the fact that Al evaporation is negligible at our growth temperature, and by the chemical affinity of Al with Ga, which gives no reason for Al to leave the droplet. From summation of the composition profile of Fig. 5.2b, over the (Al,Ga)As→GaAs tail (marked by the black arrow in Fig. 5.2b), we obtain the amount of Al transferred from the droplet to the NW during depletion (∼0.65 ML), which is equal to the initial number of Al atoms in the liquid (since we provide no Al during this phase). Neglecting the very small variation of lattice parameter between the end point binaries, the number of group III atoms N_{III}^{ML} in a NW of radius R is given by:

$$N_{III}^{ML} = \frac{4\pi R^2}{\sqrt{3}a_0^2} \tag{5.1}$$

where a_0 is the GaAs lattice parameter. Given the absolute number of Al atoms transferred into the solid, we can calculate the Al atomic fraction in the liquid $y_{Al} = N_{Al}^l/N^l$ where N^l is the total number of atoms in the liquid. The latter can be estimated by dividing the droplet volume V (modeled as a spherical cap) by the Ga atomic volume Ω_{Ga}:

$$N^l = \frac{V}{\Omega_{Ga}} = \frac{\pi R^3}{\Omega_{Ga}} \frac{(1-\cos\beta)^2(2+\cos\beta)}{3\sin^3\beta} \tag{5.2}$$

where β is the droplet contact angle. Given the NW radius R (60 nm) and a droplet contact angle β of 135° (measured post-growth), we evaluate the steady-state Al atomic concentration to be $y_{Al} \approx 4 \times 10^{-4}$. This estimate is consistent with EDX measurements of the droplet composition after growth of an homogeneous $Al_{0.1}Ga_{0.9}As$ section, which showed

[2]The difference is even more striking when we consider that our NWs are much thicker than those described in Ref. [102] (diameter of about 120 nm compared to 60 nm). Recall from Section 1.5.1 that the reservoir effect should affect more NWs with large droplet volumes.

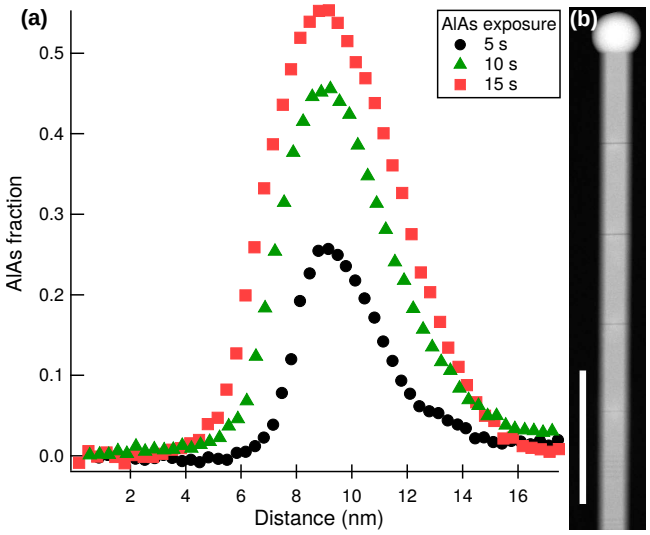

Fig. 5.3 a) Composition profiles from sample B, for insertions grown for 5, 10 and 15 s; b) HAADF image of the NW of sample B, scale bar is 0.5 µm.

the Al content to be below the detection limit of the method (around 0.5%). Nonetheless, the Al concentration in the solid is some 250 times higher, indicating that Al has a much stronger tendency to incorporate into the solid than Ga.

5.3.2 The effect of As flux and Al diffusion

Although fairly sharp, the interfaces of sample A are still not optimal. In order to improve the interface abruptness and to study in greater detail the effect of the exposure time, we grew sample B, which contains insertions formed by supplying Al and As during 5, 10 and 15 s. In contrast to sample A, the As flux was reduced to 10% of its standard value during the growth of the insertions. Figure 5.3 shows the composition profiles obtained by applying Eq. 2.3 to HAADF profiles from sample B, for the three (Al,Ga)As insertions.

The maximum Al content in the insertions of sample B is higher than in sample A. This is a direct consequence of the lower As flux which results in a lower growth rate and causes the Al to be distributed over fewer layers. Integrating the profiles along the NW axis, we obtain the total amount of Al incorporated in each insertion. Since the absolute Al flux is known, we can calculate the number of Al atoms directly impinging on a droplet of known geometry (using the calculation of Glas [50], for a beam incidence angle α of 17.2°)[3] for a given exposure time. We then compare this number with the number of Al atoms in the NW.

[3]For this incidence angle, the surface of the droplet intercepting the flux is simply $\frac{\pi R^2}{\sin^2 \beta}$.

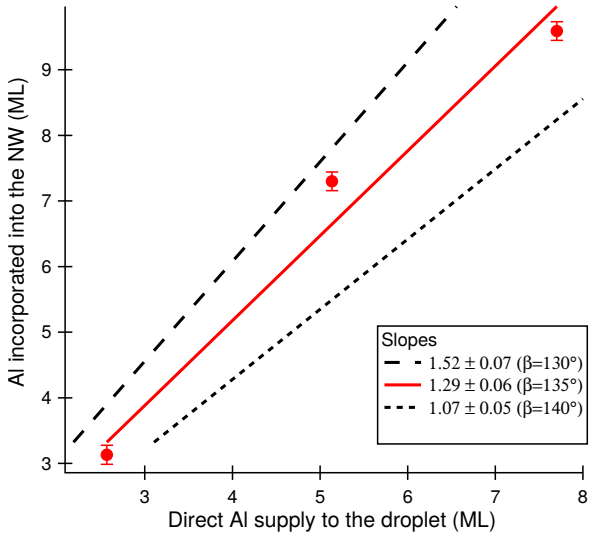

Fig. 5.4 Plot of total Al incorporated into the NW versus the amount of Al impinging directly on the droplet, both expressed in NW MLs, for the insertions in sample B. Red disks: experiment using the post-growth value of $\beta = 135°$, and corresponding linear fit (solid line). Two other values of the contact angle β are tested, namely 130° (dashed line) and 140° (fine dashed line).

This allows us to distinguish the contribution of the direct flux from the indirect flux possibly due to adatom diffusion on the NW sidewalls.

Such a comparison is made in Fig. 5.4 for a NW of sample B ($R = 60$ nm). For this NW, the droplet contact angle is $\beta = 135°$ after growth, but we allow for the possibility that β might have been slightly different during growth. The relation between the numbers of atoms incorporated into the solid and atoms supplied is linear, but the slope varies strongly with the assumed value of β, e. g. between 1.07 for $\beta = 140°$ and 1.52 for $\beta = 130°$. If only the atoms impinging on the droplet were incorporated, the slope should be unity. Slopes larger than 1 indicate a diffusive contribution other than direct impingement. For our long NWs, as a first approximation, the sidewall diffusion contribution relates to the Al flux intercepted by a rectangle of area $2R\lambda$, with λ the surface diffusion length. The maximum value of λ obtained in this way (for $\beta = 130°$) is 0.28±0.04 µm. However, it is more likely that β was larger during growth, which would correspond to a much smaller diffusion length. In any case, these estimations show that Al surface diffusion is far from being the dominant contribution to (Al,Ga)As growth.

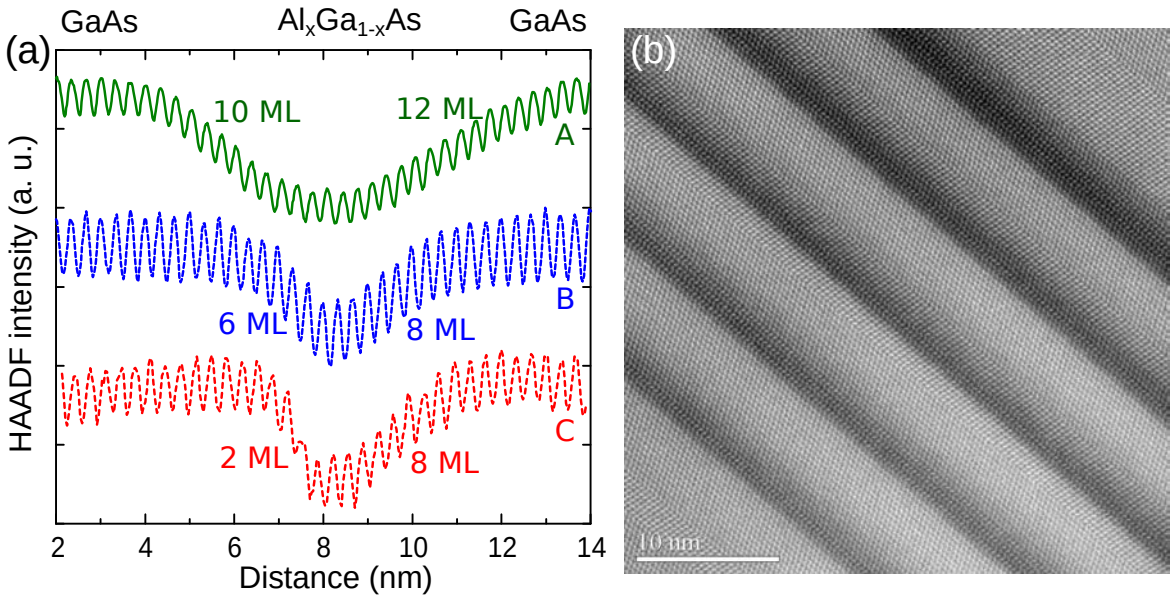

Fig. 5.5 a) HAADF profiles for 5s insertions of Al. Comparison of interface widths for continuous growth (solid green line, sample A), growth with reduced As flux (dashed blue line, sample B) and with pre-filling (dashed red line, sample C); b) High-resolution HAADF image of a series of 5 s (Al,Ga)As insertions in sample C.

5.3.3 Improving interface abruptness with droplet pre-filling

Finally, we consider sample C where, before growth of the insertions, all fluxes, including As, are interrupted completely for 30 s. Then, Al and As are supplied sequentially: the flux interruption followed by supply of Al is referred to as droplet *pre-filling*. The underlying idea is to stop NW growth and to enrich the droplet with Al before resuming it, possibly leading to a sharp interface. Similar strategies of droplet engineering (that is, a deliberate modification of the state of the droplet) have been used successfully for other purposes, such as the control of growth direction [142] and polarity [147], and to improve the NW verticality on Si (111) substrates [115]. In practice, the droplet is pre-filled with Al for 5 s. After that, As alone is supplied for 15 s, before resuming growth of GaAs. The comparison of interface abruptness between insertions grown for 5 s with standard As flux (sample A), reduced As flux (sample B) and with droplet pre-filling is given in Figure 5.5a.

The GaAs→(Al,Ga)As interface becomes more abrupt when the growth rate (or As flux) is reduced. The composition gradient does not spread over more than 2 MLs when growth is stopped completely during the supply of Al. On the other hand, the width of the (Al,Ga)As→GaAs interface does not depend significantly on the growth procedure. These findings are elucidated in the following modeling of the composition gradients.

5.4 Modeling the interface composition

The thermodynamics governing the catalyzed growth of alloyed III-V NWs from a liquid is complicated by the high number of components, at least four when a foreign catalyst metal is used. In this respect, self-catalyzed (Al,Ga)As NWs constitute a simpler case. The liquid is fully characterized by the three atomic fractions y_i (i = Ga,Al,As), of which only two are independent since $y_{\mathrm{Al}} + y_{\mathrm{Ga}} + y_{\mathrm{As}} = 1$. The solid is a pseudo-binary $(\mathrm{AlAs})_x(\mathrm{GaAs})_{1-x}$ alloy characterized by a single parameter, the fraction x of AlAs pairs. Moreover, extensive thermodynamic data are available for this system; see Ref. [7] for a comprehensive review.

We represent NW growth by the addition of individual MLs, each characterized by its own x value. Our aim here is not to describe fully the growth kinetics, which would oblige us to account for the fact that NW growth usually occurs far from equilibrium, but simply to model the evolution of the composition of the solid NW in given growth conditions. Within these limits, our central assumption is that the distribution coefficient of Al atoms between liquid and solid, x/y_{Al}, is the same as at equilibrium. This is somehow justified by the fact that the relative incorporation of Al and Ga into the solid is more likely to be governed by group-III concentrations in the liquid phase and by barriers for attachment to the solid, which presumably depend only weakly on the supersaturation. We stress that we do not make any assumption about the composition of the solid nucleus which probably mediates the formation of each ML. We simply suppose that this nucleus is sufficiently small for the ML composition to be determined by post-nucleation attachment kinetics.

5.4.1 Liquid-solid equilibrium of the Al-Ga-As alloy

Our objective is to determine the relation between the composition of the liquid and the composition of the solid *at equilibrium*. Equilibrium between the ternary liquid and the pseudo-binary solid is defined by the equality of the chemical potentials of the two types of III-V pairs (Ga-As and Al-As) in the two phases:

$$\begin{cases} \mu^l_{\mathrm{Al}} + \mu^l_{\mathrm{As}} = \mu^s_{\mathrm{AlAs}} \\ \mu^l_{\mathrm{Ga}} + \mu^l_{\mathrm{As}} = \mu^s_{\mathrm{GaAs}} \end{cases} \tag{5.3}$$

In Eq. 5.3, μ^l_i is the chemical potential of element i in the liquid and $\mu^s_{i\mathrm{As}}$ that of an i-As pair in the solid. As mentioned above, at given temperature and pressure, the liquid has two degrees of freedom whereas the solid has only one. At equilibrium, the two constraints expressed by Eq. 5.3 leave only one degree of freedom, for instance the Al fraction in the liquid, y_{Al} . Once this parameter is fixed, all the others are determined.

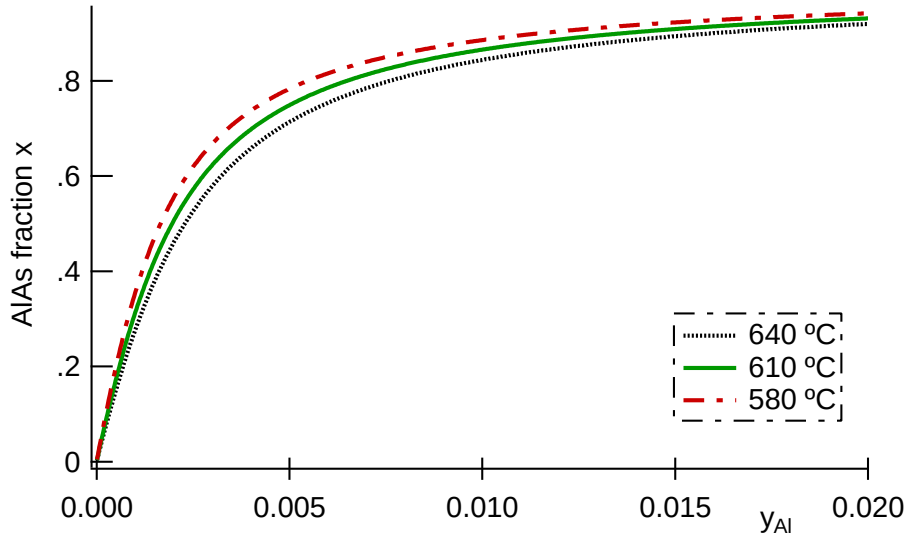

Fig. 5.6 Calculated solidus curves in the Ga-rich corner for typical NW growth temperatures.

The critical review by Li et al. [85] provides explicit expressions for the Gibbs energy of the system, obtained via the CALPHAD scheme [89], from which we calculate the relevant chemical potentials. By solving the system (Eq. 5.3), we get the solidus. Given the very low estimates of the Al and As [54] concentrations in the droplet, we limit ourselves to the Ga-rich corner, shown in Figure 5.6. The detail of this calculation is given in Appendix A.

The curves in Fig. 5.6, calculated for typical NW growth temperatures (580-640 °C) and an Al concentration in the liquid up to 2%, show that the solid is strongly enriched in Al ($x \gg y_{\mathrm{Al}}$), consistently with our experimental estimation from sample A. Moreover, x is a steeply non-linear function of y_{Al}. We observe that the solidus becomes steeper as the temperature is decreased. In other words, the competition for incorporation between AlAs and GaAs is controlled by the temperature, with incorporation of AlAs pairs being favored at low growth temperatures.

5.4.2 Predicting the composition profile

Now that we have derived function $x(y_{\mathrm{Al}})$ connecting the compositions of liquid and solid, we may attempt to model the shape of the interfaces and to reproduce the experiments. The mass balance for the Al atoms reads:

$$\frac{dN^{l}_{\mathrm{Al}}}{dt} = -N^{\mathrm{ML}}_{\mathrm{III}} x(y_{\mathrm{Al}}) r + \varphi \tag{5.4}$$

where N^l_{Al} is the number of atoms in the droplet, $N^{\mathrm{ML}}_{\mathrm{III}}$ the total number of group III atoms in one ML, $x(y_{\mathrm{Al}})$ the composition of the solid ML, r the instantaneous rate of formation of MLs and φ the Al current (atoms per unit time) entering the droplet. Moreover, $N^l_{\mathrm{Al}} = y_{\mathrm{Al}} N^l$, where N^l is the total number of atoms in the liquid. Because $y_{\mathrm{Al}} \ll 1$ and y_{As} is typically of the order of 1% for self-catalyzed growth [54], the droplet is always overwhelmingly composed of Ga. We may thus assume that $dN^{\mathrm{l}}/dt \approx 0$ over the relatively short period of heterostructure formation. Then, Eq. 5.4 rewrites:

$$\frac{dy_{\mathrm{Al}}}{dt} = -grx(y_{\mathrm{Al}}) + \frac{\varphi}{N^{\mathrm{l}}} \tag{5.5}$$

where $g \equiv N^{\mathrm{ML}}_{\mathrm{III}}/N^{\mathrm{l}}$ is a NW-specific geometric factor which depends only on NW radius and droplet contact angle (see Eq. 5.1 and Eq. 5.2). We emphasize that our model does not contain any fitting parameter. Nevertheless, while the NW geometry (g and N^{l}) can be generally determined by post-growth measurements, the direct measurement of the instantaneous growth rate r is not possible in conventional epitaxy systems.

We start by simulating the complete shape of the insertions of samples A and B, via Eq. 5.5, which requires an accurate estimate of the incoming Al current. This is obtained from the experimental data as done in Section 5.3.2. The total amount of Al atoms entering the solid is given by the sum of the compositions of all MLs. Assuming that the Al atoms leave the liquid only through solidification, we know how many atoms have entered the droplet and hence, from the time of exposure, the influx φ of Al. The only unknown left in Eq. 5.5 is now the growth rate r. Recalling again that the steady-state growth rate is governed by the As flux, which is kept constant in samples A and B, it seems reasonable to assume, as a first approximation, that r is also constant during the growth of the insertions.

Under this hypothesis, the overall agreement between numerical calculations based on Eq. 5.5 and experiments, is good for sample A (Fig. 5.2b,d) and fair for sample B (Fig. 5.7, empty triangles). Note that, especially in sample B, the calculation tends to overestimate the composition of the first MLs of the GaAs →(Al,Ga)As interface (and underestimate that of the last MLs). A possible explanation is that the growth rate might not be strictly constant. Actually, addition of Al to the ternary liquid depresses the solubility of As [85, 106], which potentially speeds up growth.

Instead of attempting to reproduce the whole insertion profile, which is sensitive to r, we may solve numerically Eq. 5.5 for the (Al,Ga)As→GaAs interface only. This corresponds to Al purge from the droplet under zero Al current ($\varphi = 0$). In this case, the profile of the interface does not depend on the growth rate (whether it be constant or not) but only on the initial Al concentration in the liquid and NW/droplet geometry (described by the parameter

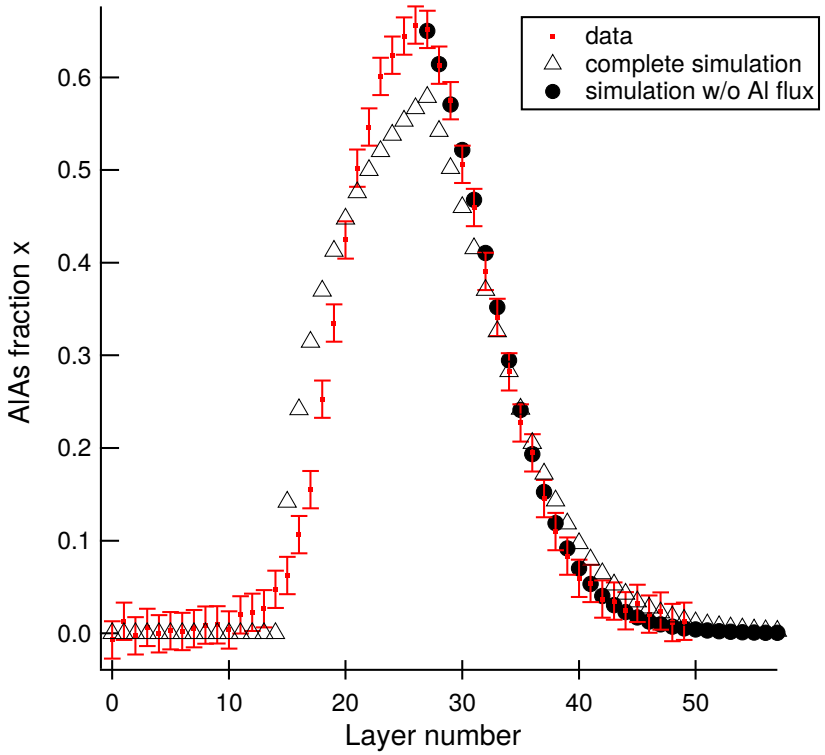

Fig. 5.7 Simulation of the compositional profile in Figure 5.1 (sample B, 15 s of AlAs). Red dots: experimental data. Empty triangles: calculated profile using a square pulse Al current. Circles: profile calculated in the sole (Al,Ga)As→GaAs section, when the Al current is zero.

g). This is easily seen by setting $\varphi = 0$ in Eq. 5.5 and by introducing the axial coordinate z, such that $dz \equiv rhdt$, where h is the height of one ML:

$$\frac{dy_{\mathrm{Al}}}{dz} = -\frac{g}{h}x(y_{\mathrm{Al}}) \tag{5.6}$$

Alternatively, it can be understood simply as follows: each ML adopts a composition $x(y_{\mathrm{Al}})$ dictated by the composition y_{Al} in the liquid before the ML was formed; this depletes the liquid of the corresponding number of Al atoms (fixed by R), which in turn, given the droplet volume, sets the new value of y_{Al} for the next ML. The initial concentration $y_{\mathrm{Al}}(t=0)$ is determined, again via the $x(y_{\mathrm{Al}})$ relation, by the composition of the starting solid ML (e.g. the one where x starts to decrease). The result of such a simulation for the insertion of sample B is given in Figure 5.7 (disks). The agreement with the experiment is now excellent. This validates our initial hypothesis, that is, the distribution coefficient of Al atoms during growth is indistinguishable from the equilibrium one.

5.4.3 An analytical solution for the interface profile

In order to go beyond the numerical simulation and find an analytical formula for the interface profile, we need an explicit expression of the function that connects the compositions of liquid and solid (at equilibrium). It turns out that this relation is well described by the following expression:

$$x(y_{\mathrm{Al}}) = \frac{\varepsilon y_{\mathrm{Al}}}{1+(\varepsilon-1)y_{\mathrm{Al}}} \tag{5.7}$$

This is similar to the Langmuir-McLean result for a segregating system [97] where ε is a parameter that depends only on temperature. Eq. 5.7 can be derived qualitatively as follows: consider the two solidification reactions $\mathrm{Al}^l + \mathrm{As}^l \rightarrow \mathrm{AlAs}^s$ and $\mathrm{Ga}^l + \mathrm{As}^l \rightarrow \mathrm{GaAs}^s$, each of them having a kinetic coefficient K_{AlAs} and K_{GaAs}. For each elementary reaction we may write that the fraction of the product is proportional to the fractions of the reactants (law of mass action):

$$\begin{cases} x_{\mathrm{AlAs}} = x = K_{\mathrm{AlAs}} y_{\mathrm{Al}} y_{\mathrm{As}} \\ x_{\mathrm{GaAs}} = 1-x = K_{\mathrm{GaAs}} y_{\mathrm{Ga}} y_{\mathrm{As}} \end{cases} \tag{5.8}$$

taking the ratio of the two equations in Eq. 5.8, recalling that $y_{\mathrm{Ga}} = 1 - y_{\mathrm{Al}} - y_{\mathrm{As}}$ and neglecting y_{As}, yields Eq. 5.7 with $\varepsilon = K_{\mathrm{AlAs}}/K_{\mathrm{GaAs}}$. Therefore ε can be interpreted as a measure of the relative strength of the two reactions. When Eq. 5.7 is fitted in the $10^{-5} \leq y_{\mathrm{Al}} \leq 0.5$ range, at 610 °C, the best value for ε is 4.97×10^2 (Fig. 5.8).[4]

[4] An even better fit can be obtained using the function $x(y_{\mathrm{Al}}) = \frac{b y_{\mathrm{Al}}^k}{1+(b-1)y_{\mathrm{Al}}^k}$ but in this case the parameters b and k have no clear physical meaning. Their best values are $k = 1.12$ and $b = 1.09 \times 10^3$.

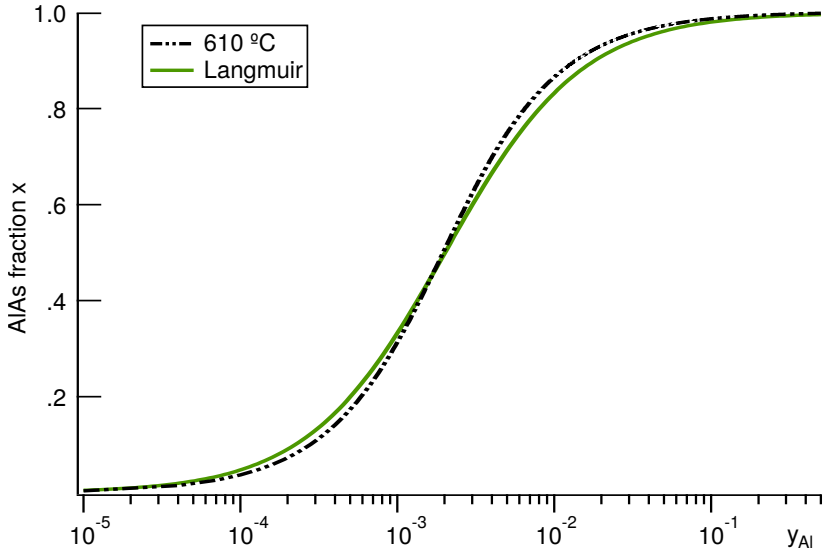

Fig. 5.8 Dash-dotted black line: solid-liquid equilibrium curve for the Al-Ga-As mixture, calculated from data in Ref. [85], at 610 °C. Solid green line: plot of Eq. 5.7 with $\varepsilon = 4.97 \times 10^2$.

A rational function that resembles Eq. 5.7, connecting the composition of the solid to the chemical potentials (which depend on solid and liquid compositions) has been proposed by Periwal et al. [111] to describe the competition between incorporation of Si and Ge in Si/Ge heterostructured NWs. Very recently, starting from an irreversible growth model, Dubrovskii and Sibirev [39] have derived an expression similar to Eq. 5.7 for ternary III-V NWs catalyzed by Au.

Inserting Eq. 5.7 into Eq. 5.5, we get:

$$\frac{dy_{\mathrm{Al}}}{dt} = -gr\frac{\varepsilon y_{\mathrm{Al}}}{1+(\varepsilon-1)y_{\mathrm{Al}}} + \frac{\varphi}{N^{\mathrm{l}}} \tag{5.9}$$

Eq. 5.9 can be solved analytically and has a simple solution when $\varphi = 0$. This corresponds in our case to the (Al,Ga)As→GaAs interface. Introducing the axial coordinate z, such that $dz \equiv rhdt$, with h the height of a ML, Eq. 5.9 then rewrites:

$$\frac{dy_{\mathrm{Al}}}{dz} = -\frac{g}{h}\frac{\varepsilon y_{\mathrm{Al}}}{1+(\varepsilon-1)y_{\mathrm{Al}}} \tag{5.10}$$

Solution of Eq. 5.10 with boundary condition $y(0) = y_0$ gives the composition profile:

$$y_{\mathrm{Al}}(z) = \frac{1}{\varepsilon-1} W\left[(\varepsilon-1)y_0 \exp\left((\varepsilon-1)y_0 - \varepsilon g\frac{z}{h}\right)\right] \tag{5.11}$$

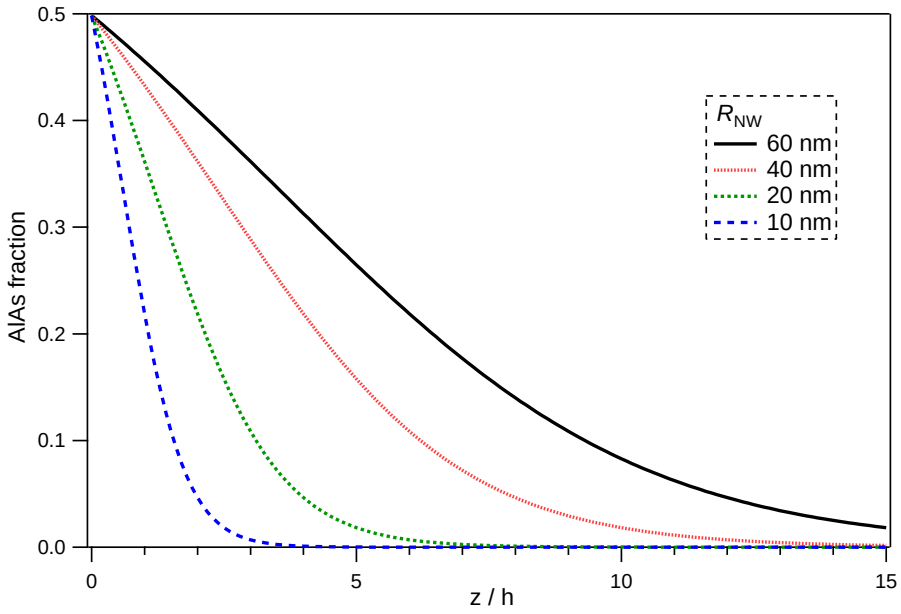

Fig. 5.9 Calculated composition profiles of the (Al,Ga)As/GaAs interface under zero Al flux for different NW radii (60, 40, 20 and 10 nm), starting with a liquid Al composition $y_0 = 2.0 \times 10^{-3}$. Very sharp interfaces are expected for thin NWs.

where W is the principal branch of the Lambert function [28].[5] Substituting back into Eq. 5.7 and using the fact that $\varepsilon \gg 1$:

$$x(z) \approx \frac{W\left[\varepsilon y_0 \exp\left(\varepsilon y_0 - \varepsilon g \frac{z}{h}\right)\right]}{1 + W\left[\varepsilon y_0 \exp\left(\varepsilon y_0 - \varepsilon g \frac{z}{h}\right)\right]} \tag{5.12}$$

which gives the general shape of the (Al,Ga)As/GaAs interface. The compositional profiles obtained from Eq. 5.12 are extremely close to the results of the numerical simulation. Plots of Eq. 5.12 for different NWs radii (of common contact angle $\beta = 135°$) are given in Fig. 5.9.

As expected (see Sect. 1.5.1 and Refs. [25, 86]), NWs show a reduced reservoir effect with decreasing droplet volumes (which are fixed by R). However, at variance with simple models of the reservoir effect (Ref. [86]), the decay profile is not exponential, especially when starting with solid compositions of high Al content. Small droplet volumes, in conjunction with the propensity of Al to incorporate into the solid phase at the expense of Ga, should thus allow the fabrication of very sharp (Al,Ga)As→GaAs interfaces in self-catalyzed NWs. Nevertheless, the realization of very thin NWs ($R_{NW} < 20$ nm) is not straightforward, although

[5] W is the inverse function of xe^x and it is single-valued for real numbers $x \geq -1/e$, a condition that in our case is always satisfied.

a priori possible by careful tuning of the V/III ratio [116]. Attempts to fabricate such NWs will be described in Chapter 6.

5.5 Conclusions

In summary, in this chapter we have demonstrated the formation of sharp interfaces in ternary (Al,Ga)As heterostructured NWs with the self-catalyzed method. We analyzed the composition gradients at the interfaces with atomic resolution. Analysis of the experimental data revealed that interfaces are some ten times sharper than those obtained using a gold catalyst. Using a strategy of growth interruption followed by supply of Al alone (pre-filling of the droplet), we have been able to reduce the GaAs/AlGaAs interface width to only 2 ML.

Comparison between the amount of Al incorporated into the NW and the amount supplied to the droplet by direct impingement, has shown that diffusion on the NW sidewalls is a minor source of Al to the droplet.

We have found that the phase diagram of the macroscopic (Al,Ga)As system predicts the stationary composition of the solid very well. Using this thermodynamic data, we have developed a model for the composition profiles. Remarkably, our model does not contain any fitting parameters, although the instantaneous growth rate and the actual geometry of the NW during growth cannot always be determined directly. We have found that the decay profile of the Al concentration during depletion is not a simple exponential. However, in line with other models of the reservoir effect, the size of the droplet has been found to be the primary factor controlling the abruptness of the (Al,Ga)As→GaAs junction. Atomically sharp interfaces are expected for nanowires with radii smaller than 20 nm, although control of the NW diameter obtained by the self-catalyzed method is still not well mastered.

Despite its importance, we have not discussed the role of the critical nucleus which likely mediates the formation of each ML. Including a theory of nucleation for the ternary case is a necessary step to understand the influence of the droplet composition on growth rates and on the crystal structure of the NWs. Clearly, the presence of a third element complicates the analysis and multiple questions arise. The first is what is the composition of the critical nucleus, and how to calculate the relevant surface energies. Another important question is whether or not the nucleus has the same composition as the rest of the ML. Finally, is the ML compositionally homogeneous? This question is important especially in thin NWs, as we have seen that the number of Al atoms stored in the droplet is often less than the number of atoms that can be stored in a NW ML. Attempts to answer these questions will certainly open the way for future discoveries and to a better understanding of how ternary NWs grow.

Chapter 6

On thin nanowires and the ultimate control of nucleation events

This chapter is about opportunities. We try to address questions regarding the control of insertion thickness and diameter in self-catalyzed NWs. Both of these are non-trivial problems and have implications for the quality of the structures obtained. Precise control of thickness and diameter (or at least one of the two) is of fundamental importance for exploitation of quantum effects. Furthermore, NWs with thin diameters can minimize the reservoir effect and improve strain relaxation at heterointerfaces. More specifically, in this chapter we discuss preliminary results on the possibility of controlling the growth of single monolayers in self-catalyzed GaAs nanowires. Building on the predicitive model of Ref. [54] and making use of numerical simulations, we explore conditions for the optimum control of the nucleation events. We highlight some of the difficulties that may be encountered experimentally. Finally, we show that the diameter of self-catalyzed GaAs and GaP nanowires can be reduced, down to 20 nm, by using a high V/III ratio at the beginning of growth.

6.1 Nucleation statistics in time

In Chapter 1 we have seen that NW growth usually proceeds layer-by-layer via nucleation. Nucleation occurs with a certain *probability*, which is determined by the supersaturation, NW geometry, and a number of interface energies. Hence, the nucleation process has an intrinsically stochastic character. However, as we have seen in Chapter 3 when analyzing the stacking sequence, certain correlations between nucleation events may exist. In Chapter 3 we found a *spatial* correlation between nucleation events. In this section, we are going to discuss the *temporal* correlation and how this can be exploited to reduce randomness,

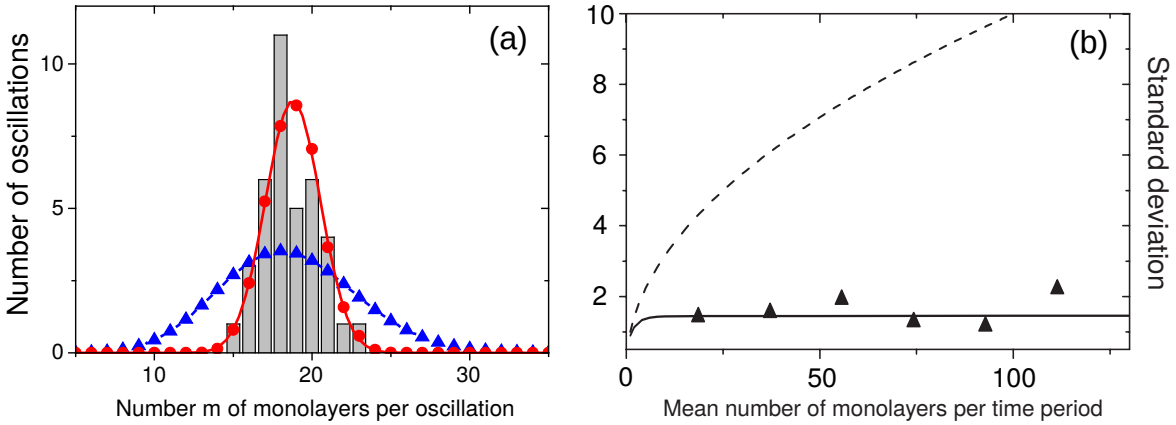

Fig. 6.1 a) Length distribution of segments between markers in an InAsP NW, showing its sub-poissonian character: triangles: Poisson distribution; red line: self-regulated statistics b) standard deviation of the number of MLs per time period. Triangles represent the experimental standard deviations for different periods and the dashed line represent the standard deviation expected from Poisson's statistics. Both panels are adapted from Ref. [53].

possibly leading to an improved control of nucleation events and, ultimately, to controlling nucleation of single layers.

In a paper by Glas et al. [53] the growth kinetics of a single In(As,P) NW was investigated using a marker technique [61]. Markers are compositional modulations introduced by periodically changing the As/P ratio. This technique allows one to record a time scale along the NW, hence giving access to the growth rate. Interestingly, the authors found that the length distribution of the segments between two markers is much narrower than the Poisson distribution, that is, the distribution that we would expect if the formation of each layer was fully independent from the previous ones (Fig. 6.1a).

Moreover, the width of this distribution (standard deviation) quickly saturates to a value independent of the average segment length, in strong contrast with the Poisson distribution, the width of which increases as the square root of the segment length (Fig. 6.1b). The authors note that the nucleation events are *anticorrelated* in time, namely that it is less likely to nucleate a NW ML just after one has formed. This is qualitatively explained as follows. Since the droplet is of finite size, the formation of a new ML causes an abrupt decrease of the concentrations group III and group V atoms, especially the latter, because of their low concentration in the droplet (a few percent at most) during growth. The drop of concentrations translates in a reduction of the chemical potentials in the liquid, on which the nucleation rate depends strongly (Section 1.3.2). Therefore, the NW has to wait for the droplet to be refilled before the nucleation probability rises again, producing the observed sub-Poissonian distribution of the nucleation events. Clearly, the width of this sub-Poissonian

distribution depends on how much the nucleation probability is lowered by each nucleation event.

In this section, using nucleation-based growth simulations in self-catalyzed GaAs NWs, we explore to which extent the width of the sub-Poissonian distribution of the segment lengths can be reduced by changing the growth parameters. Ideally, we would like to make nucleation events to be fully periodic, so that thickness control would be achieved by controlling the growth time. Note that the standard deviation of the segment lengths in the case of periodic nucleation is between zero and 0.5 MLs, depending on the time interval between markers. [1]

6.1.1 Growth rate diagram of self-catalyzed GaAs nanowires

As seen in Chapters 1 and 5, the thermodynamic state of the Ga droplet is completely defined by the temperature T and by the As fraction x. Let us rewrite the nucleation rate per unit area (Eq. 1.5) as:

$$J = A(T)x\sqrt{\frac{\Delta\mu}{k_B T}}\exp\left(-\frac{\Delta G^*}{k_B T}\right) \tag{6.1}$$

where k_B is the Boltzmann constant and ΔG^* is the nucleation barrier, which depends on $\Delta\mu$ (Eq. 1.4). $\Delta\mu$ is the difference of chemical potentials between the liquid l and solid s, and reads:

$$\Delta\mu = \mu^l_{\mathrm{Ga}} + \mu^l_{\mathrm{As}} - \mu^s_{\mathrm{GaAs}} \tag{6.2}$$

These chemical potentials are functions of x and T and have been calculated in Ref. [54] on the basis of the thermodynamic data of Ref. [6]. According to Glas et al. [54], the best values of the exponential prefactor $A(T)$ and nucleus edge energy Γ are 7.01×10^{18} m^{-2} s^{-1} and 0.123 J m^{-2}, respectively. Assuming mononucleation, knowledge of x and T allows one to obtain the growth rate via Eq. 6.1 and we may thus construct a "growth rate diagram", as illustrated in Fig. 6.2 for a NW of radius $R = 50$ nm.

From Fig. 6.2, we see that there exist values of x and T at which growth does not occur (where $\Delta\mu \leq 0$, white region). We call the boundary between this region and the rest of the diagram the equilibrium line (where $\Delta\mu = 0$). Not surprisingly, the growth rate increases quickly with As concentration. On the other hand, for a given x, the growth rate increases with decreasing temperature (because of the increasing $\Delta\mu$).

It is instructive to measure the As concentration in terms of equivalent GaAs MLs. Since the number of As atoms in one ML is $N^{\mathrm{ML}}_{\mathrm{As}} = 4\pi R^2/(\sqrt{3}a_0^2)$, where a_0 is the GaAs lattice parameter, x is readily converted in number of MLs. This is plotted in Fig. 6.3 for NW radii between 10 and 50 nm and droplet contact angle β =135°.

[1] For a discussion of the sub-Poissonian statistics, see Ref. [51].

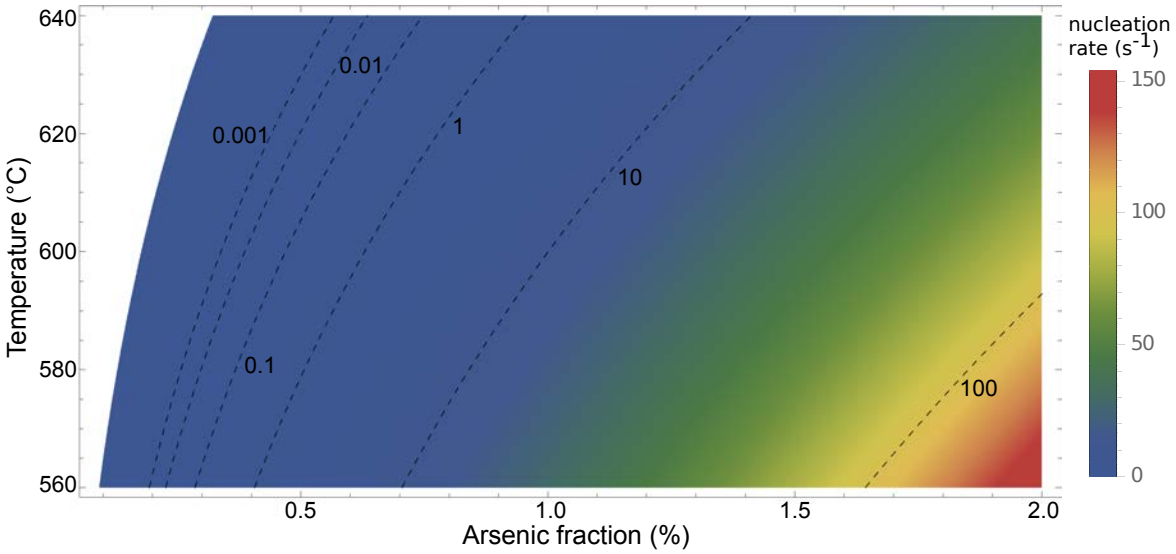

Fig. 6.2 Plot of nucleation rate for a typical NW with radius R =50 nm, as function of temperature and As concentration in the droplet. Contours of constant growth rate are spaced by a factor 10 from each other.

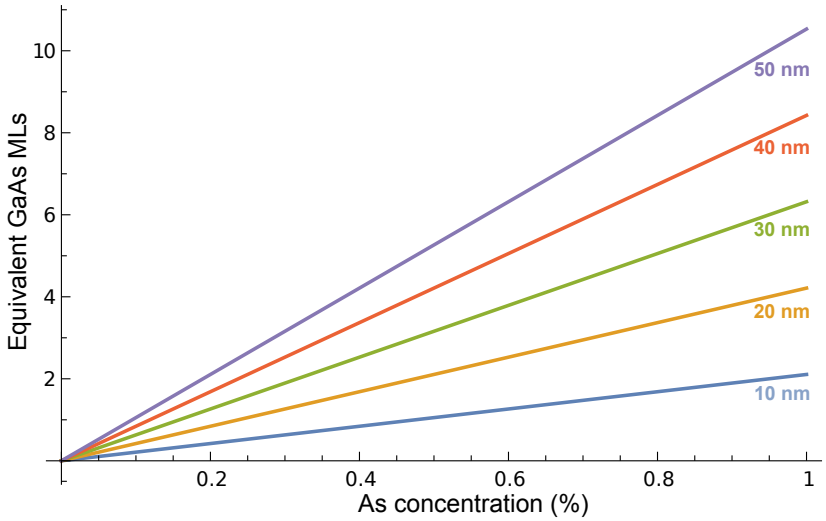

Fig. 6.3 Arsenic concentration expressed in terms of equivalent GaAs MLs for NWs of different radii and droplet contact angle β =135°.

By comparing Figs. 6.2 and 6.3, we see that for a NW with radius 50 nm, growing in standard conditions (growth rate in the 1-10 ML/s range and temperature in the 590-610 °C range), x lies between 0.5% and 1.1%, which corresponds to roughly 6-12 MLs. This shows that the number of MLs stored in the droplet during *steady-state* growth is indeed small, but not negligible. This "excess" As contributes to $\Delta\mu$ and thus to the growth rate, without however incorporating into the solid. Such an As reservoir represents a big obstacle to the control of nucleation events, because removal of one As equivalent ML does not reduce the composition of the liquid drastically.

Our objective is thus to find growth conditions for which the As fraction x is significantly altered by the removal of one equivalent ML. This goal may be achieved either by having thin NWs (Fig. 6.3) or by reducing the As flux, thus lowering the steady-state value of x. Note that reduction of the steady state value of x reduces the growth rate rapidly, and that, at fixed value of x, thin NWs will grow more slowly than thick ones, because the nucleation probability scales as R^2. Therefore we are confronted with a trade-off between growth rate and amount of As stored in the droplet. Before we continue the discussion of the steady-state case, let us analyze how the droplet is emptied because of growth and evaporation, and what are the characteristic timescales of each of these processes.

6.1.2 Depleting the droplet: growth versus evaporation

The As concentration during steady-state growth results from the balance between the incoming flux (both direct and re-emitted from the neighboring surfaces) and the outgoing flux due to growth and evaporation. Gaseous arsenic can exist as atomic As, As_2, As_3 and As_4 molecules; however the equilibrium pressure of As_2 is by far the largest. Following Glas et al. [54] we write the evaporated As atomic flux J_e as:

$$J_e = \frac{2p_2}{\sqrt{2\pi M k_B T}} \tag{6.3}$$

where M is the mass of the As_2 molecule and p_2 is its partial pressure at equilibrium with the liquid, which is found in Ref. [6]. In order to compare how quickly the As atoms are removed because of evaporation, compared to growth, in Fig. 6.4 we simulate the random time evolution of x without As supply, for a NW of radius 40 nm and two typical growth temperatures, starting from an arbitrary initial concentration $x(t=0) = 0.02$.

The steps visible in the left panel of Fig. 6.4 are associated with the formation of single MLs. We observe that growth is the main mechanism of droplet depletion, with evaporation being a much slower process. The As fraction drops quickly (in less than 1 s) until nucleation is no longer possible. Using Fig. 6.3, we see that after the last nucleation event about 3-4

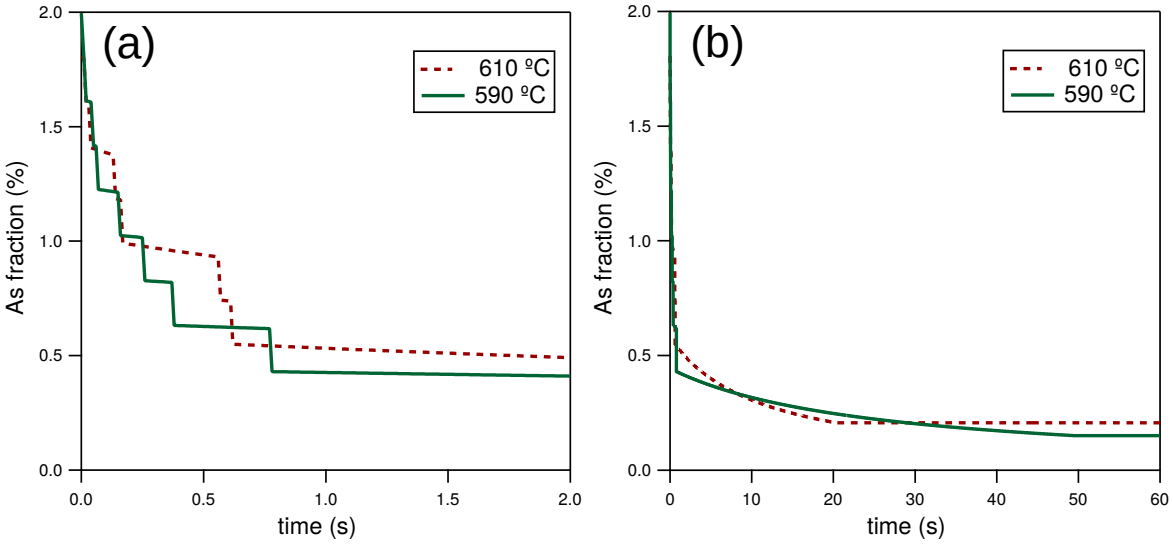

Fig. 6.4 Temporal evolution of the As fraction x for a NW with $R = 40$ nm, starting from 2% at time zero. a) Evolution of x in the first 2 s. b) Evolution of x in the first minute.

MLs are still stored in the droplet. These MLs are slowly evaporated until the equilibrium As fraction is reached (the equilibrium fraction is lower at lower temperatures). Evaporation becomes more efficient with increasing temperatures. However, it is risky to use evaporation as the main depletion mechanism, because if the As fraction drops below its equilibrium value the system would compensate by dissolution of the already grown layers. Moreover, the reduced $\Delta\mu$ at high temperatures would require larger As fluxes to induce growth, which (as we have seen in Chapter 4) are an issue in MBE as they increase the residual pressure in the chamber. For these reasons, it is preferable to minimize evaporation by using moderate growth temperatures ($\sim$600 °C and lower).

6.1.3 Difficulties of the steady-state approach

Besides keeping evaporation under control, a relatively low temperature is helpful to enhance the growth rate when low fluxes are used. Recall however that the survival of the Ga droplet (and thus of self-catalyzed growth itself) depends critically on the V/III ratio at the NW tip. In particular, the amount of Ga reaching the droplet depends on the diffusive contribution from the NW sidewalls [27, 38], which in turn depends on temperature. Moreover, in MBE, low temperatures favor the vapor-solid growth on the sidewalls (radial growth). For these reasons, self-catalyzed GaAs NW growth is typically performed in the 580-630 °C range. Very recently, Balaghi et al. [10] showed that self-catalyzed growth can be extended down to 450 °C by alternate supply of Ga and As, an approach similar to migration-enhanced epitaxy. However, achieving an optimal V/III balance with alternate supply is tricky, as more growth

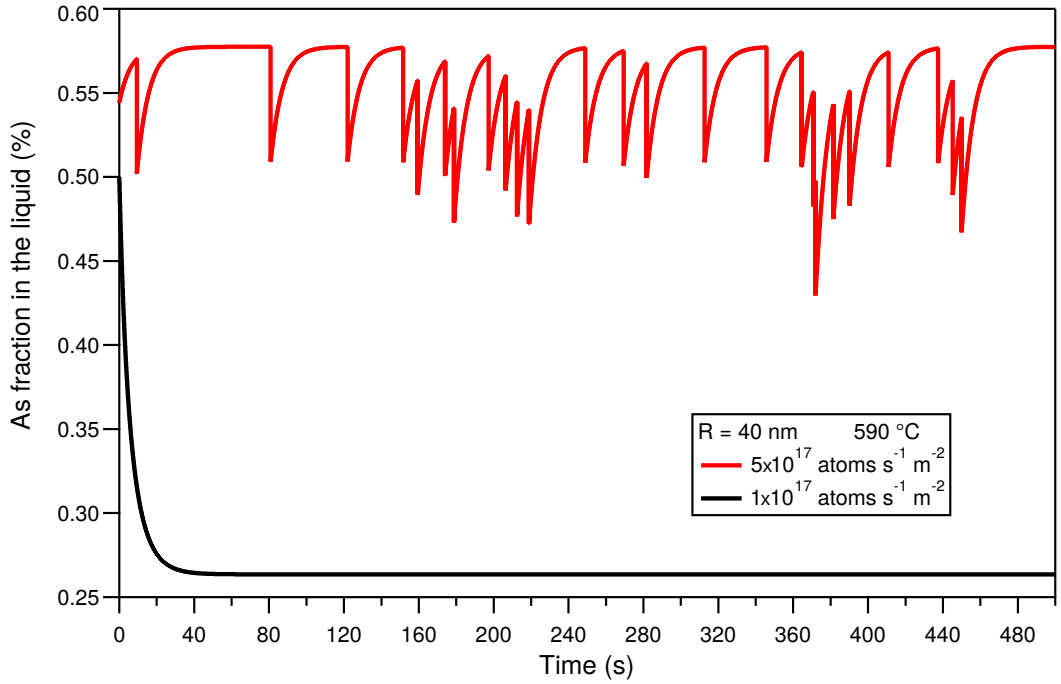

Fig. 6.5 Temporal evolution of the As concentration for a NW with $R = 40$ nm grown at 590 °C for two different "low" fluxes.

parameters are added (namely the supply durations for Ga and As and the delays between pulses), compared to standard steady-state growth, where fluxes are kept constant.

Here, we analyze the steady-state case in the lower part of the temperature window, at 590 °C. It is easily seen that the reduction of the As flux alone is not a viable approach to produce quasi-periodic nucleations for typical temperatures and typical NW radii. This point is illustrated in Fig. 6.5, where the time evolution of x is plotted for the NW of Fig. 6.4 using two different "low" fluxes that produce growth rates much smaller than 1 ML/s. The flux supplied is given in units of atoms m^{-2} s^{-1} and includes both the direct and re-emitted contributions.[2] These are 10 and 20 times lower than the flux which produces a growth rate of $\sim$2 ML/s for the same NW.

For the first flux of 5×10^{17} m^{-2} s^{-1}, we observe that the concentration profile is a smoothed sawtooth, reflecting the fact that the rate of supply is comparable to the rate of removal due to evaporation. The growth rate is very small, of the order of 0.05 ML/s on average. It is not necessary to perform a statistical analysis to see that nucleation is still quite random in time. Further reduction of the flux (black line in Fig. 6.5) leads to insufficient As supply for growth to occur, as x drops to a value close to equilibrium. We conclude that

[2]The re-emitted flux depends on temperature and geometry of the NW array. However, the precise source of As does not matter to our analysis, which only requires the amount of As reaching the droplet. Therefore, the flux is defined as the current entering the droplet divided by the droplet surface.

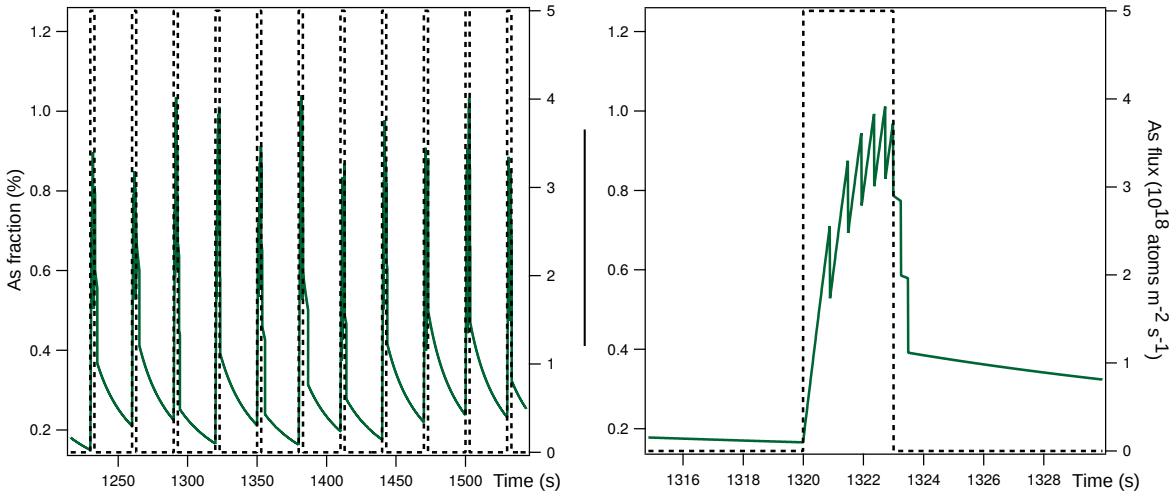

Fig. 6.6 Example of As flux pulsing for the growth of short segments. a) Continuous green line: time evolution of the As concentration (left axis), dashed black line: As flux (right axis). b) Detail from panel a) for one of the flux pulses.

using very low fluxes is not enough to produce quasi periodic ML formation. However, the standard deviation of the length distribution of long segments grown in this way is small, 0.7 in the example shown here. For comparison, growth in standard condition produces standard deviations larger than one (but typically smaller than 2) [51]. We performed a limited set of simulations for the same NW at lower temperatures, down to 500 °C, without finding major improvements in the standard deviation, which always remains in the 0.6-0.7 range. Nevertheless, further analysis is required to clarify this point. To summarize, reduction of the flux and temperature is beneficial to reduce the standard deviation of the segment lengths, at the expense of the growth rate. Although randomness is reduced compared to growth with standard fluxes, the process is still far from being quasi-deterministic.

6.1.4 Pulsing the As supply

In this section, we demonstrate that it is possible to grow short segments with high reproducibility by pulsing the As source (as in Ref. [10]), instead of using a continuous supply. An example is given in Fig. 6.6. The simulation is again performed on a NW of 40 nm radius, at 580 °C, with As supplied as a square wave of period 30 s and 10% duty. The amplitude of the wave is such that it would produce a growth rate of about 10 ML/s in the steady state.

The period of the pulses was chosen to allow the droplet to consume As by both growth and evaporation. Since evaporation is a much slower process than nucleation, the equilibrium line is never reached, despite the relatively long flux interruptions. It turns out that this strategy allows one to grow almost the same number of MLs in each cycle. The distribution

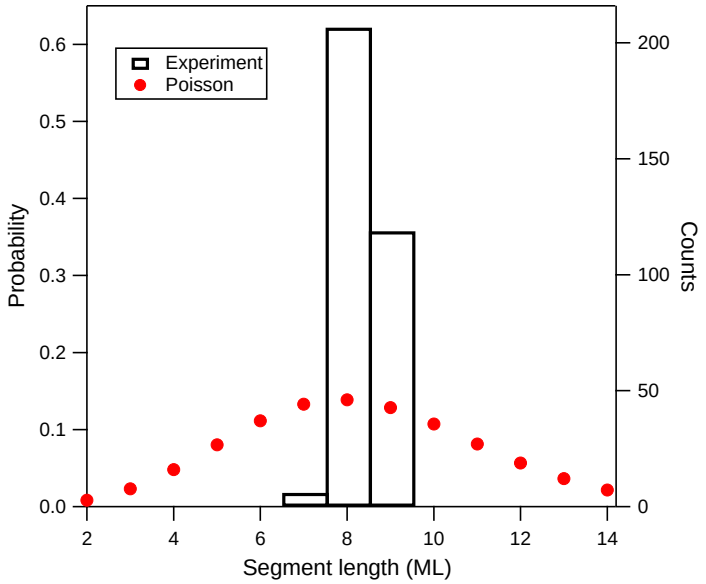

Fig. 6.7 Distribution of the number of layers grown for each As pulse (bars), expressed in terms of probability and counts, compared with the Poisson distribution (red disks). The distribution is very narrow, as the standard deviation is 0.5 ML.

of the layers grown during individual pulses is shown in Fig. 6.7, expressed in terms of probability and counts. The distribution is narrower than that obtained in the steady state (standard deviation of 0.52 ML, compared to 0.6-0.7 MLs at best in the steady state). The weighted average is of 8.4 MLs, with the majority of pulses (62%) producing exactly 8 MLs, 9 MLs in the 36% of the cases and occasionally 7 MLs (2% of the cases).

Nevertheless, while the method appears to be effective for the growth of short segments, it cannot be used repeatedly for the growth of long segments. The standard deviation of the distribution of each cycle (Fig. 6.7) is indeed small, but it is still greater than zero. Therefore, trying to grow long segments by pulsing the As flux N times will result in the dispersions of single cycles adding up together. Since the cycles are statistically independent from each other,[3] then the standard deviation of the segment length would increase as $\sqrt{N}$, eventually becoming worse than what one would obtain by growing the same number of MLs in the steady state.

6.1.5 First experimental demonstrations

In this section, we show two experimental demonstrations of growth at low supersaturation. The first one is taken from the Ga(As,P) NWs studied in Chapter 4 (Fig. 6.8). The GaAs

[3] During the flux interruption, the As concentration is reset close to its equilibrium value, so that the memory of the droplet is practically "erased".

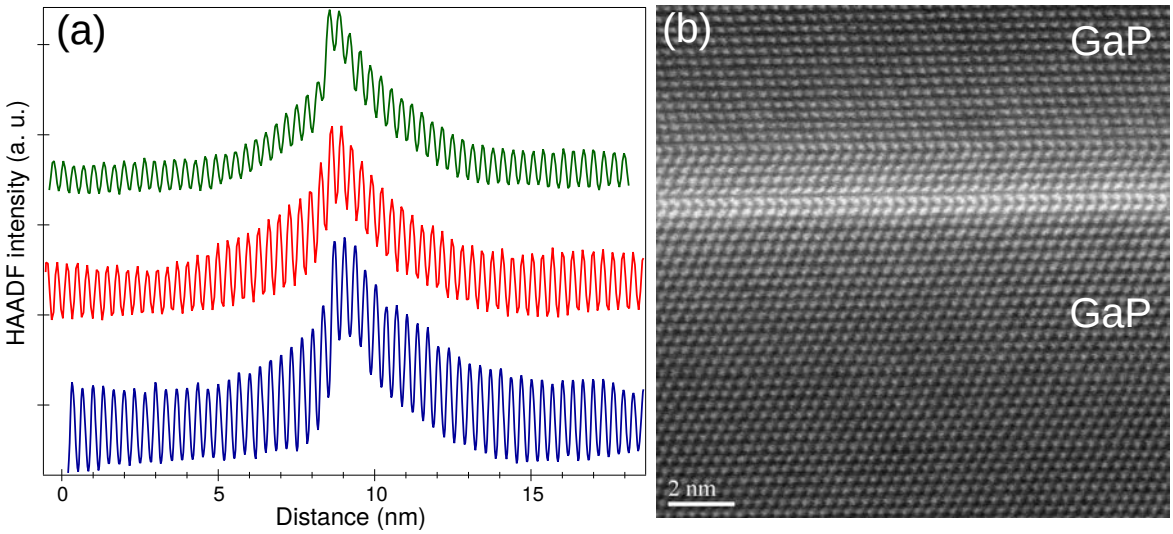

Fig. 6.8 Ultra-thin insertions in sample VLI. a) HAADF intensity recorded across the 5 s insertions on three different NWs. b) HAADF image of one GaAs insertion. The growth direction points upwards.

insertions grown for 5 s in sample VLI[4] were very thin, although we did not discuss the reason for this at that point. Recall that the shape of these insertions was not flat and showed truncation facets, the formation of which we attributed to the lowering of group V concentration in the droplet during the flux interruption. In practice, the situation is similar to the one described in the previous section, in which a depleted droplet is suddenly exposed to an As flux. HAADF intensity profiles extracted from high-resolution images of the thin insertions, for three different NWs from sample VLI, are shown in Fig. 6.8a.

The HAADF profiles are remarkably similar to each other, although it is not possible to define the thickness of the insertion unambiguously because of the intensity gradients at both leading and trailing edges. Five seconds of As supply at the rate used in sample VLI would produce a growth of 7.5 nm (24 MLs) in the steady state, while here only 2 or 3 MLs are grown. Therefore some 20 MLs are missing, a number that cannot be explained only by the flux transient of the As cell.[5] This observation is compatible with the picture in which the NW has to wait and store enough As in the droplet before the nucleation probability becomes high enough to cause growth. The As stored in the droplet but not directly participating to growth may also explain, at least in part, the compositional gradient observed afterwards: when growth of GaP is resumed, the concentration of the group V species rises up to the point

[4]Recall that, in sample VLI, all fluxes were shut off completely for one minute prior to heterostructure growth.

[5]The As flux does not take more than 2 s to stabilize, which is roughly the time necessary to grow 10 MLs in the stady state.

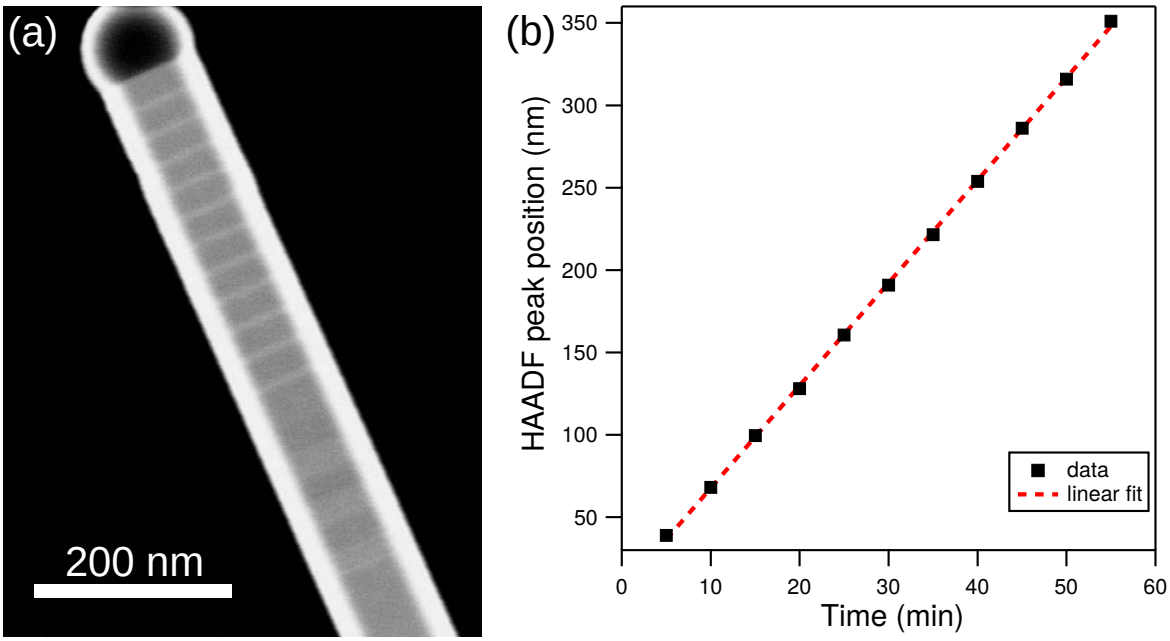

Fig. 6.9 a) STEM-SEM HAADF image of a GaAs NW with (Al,Ga)As makers grown using reduced fluxes. b) position of the markers as function of time, showing a constant growth rate, as usually observed for growth in standard conditions.

at which the nucleation barrier is overcome. After nucleation has occurred, As incorporation is limited only by the barrier of attachment to the growing nucleus. Since the barrier for attachment of the two group V species is likely to be similar [149], As is gradually removed along with P.

The next illustration is a GaAs NW sample grown using reduced fluxes at 580 °C (Fig. 6.9). To avoid problems right at NW formation, NWs are grown using standard fluxes for the first 20 min, at the end of which three thick (Al,Ga)As insertions are introduced to mark the position where standard growth ended. After this, all fluxes are interrupted for 5 min to adjust the Ga and Al cell temperatures. Growth is then resumed for one hour with fluxes equal to 1/10th of their value during standard growth. AlGaAs markers were introduced by simply opening the Al shutter every 5 min for 1 min. The STEM-SEM HAADF image of a representative NW from this sample is shown in Fig. 6.9a.

From the HAADF image we can track the positions of the intensity peaks associated with the (Al,Ga)As markers, as shown in Fig. 6.9b. A perfect linear time dependence of the marker positions is observed, from which we calculate the growth rate to be 6.2 nm/min or 0.3 ML/s. From the simulations presented above, at this growth rate the distribution of segment lengths between markers should be narrower than for standard growth (improving thickness control), although this has not yet been confirmed by statistical analysis. Nevertheless, the

reduction by a factor 10 of the As flux is beneficial for the background pressure of the MBE chamber, which remained constant at 1×10^{-9} Torr. Low background pressures can palliate the problem of compositional control in III-V-V heterostructures without the need of long flux interruptions. Growth of group V heterostructures using low fluxes will be the object of future investigations.

6.1.6 Conclusions

In summary, keeping the As fraction x as close as possible to the equilibrium line helps to maximize the temporal anticorrelation between nucleation events. This comes however at the expense of the growth rate, which may become too low for practical purposes. The growth rate can be increased by lowering the temperature, which has the unwanted effect of reducing Ga diffusion and promoting radial growth. Moreover, the standard deviation of the segment lengths does not appear to change significantly between 600 and 500 °C, which probably makes low growth temperatures not useful to achieve ML control. Growth at high temperatures makes As evaporation important, and dissolution of the already grown MLs and decomposition at the NW sidewalls occurs, unless it is prevented by a properly balanced As overpressure. On the other hand, if growth of short segments is desired, pulsing the As source at moderate temperatures can result in excellent thickness control. One can imagine, for example, fabricating a GaAs/GaP superlattice by alternating As and P pulses of fixed duration. These growth conditions would prevent group V accumulation in the MBE chamber, minimizing the group V background pressure, hence optimizing compositional control.

6.2 Growth of thin NWs

Throughout this manuscript, we appreciated how the realization of self-catalyzed NWs with small diameters would be helpful to improve interface abruptness and favor strain relaxation in NW heterostructures. Moreover, NWs with diameters smaller than 20 nm are needed for quantum effects to become important (the Bohr radius of the free exciton in GaAs is 13 nm). Similarly to VLS growth assisted by a foreign metal, the diameter of self-catalyzed NWs is determined by the size of the droplet. However, the size of Ga droplets depends on the balance between rate of arrival and rate of consumption of Ga, and therefore on the V/III ratio, as noted by Paek et al. [103], who observed increasing NW diameters with increasing Ga flux and decreasing diameters with increasing As flux.

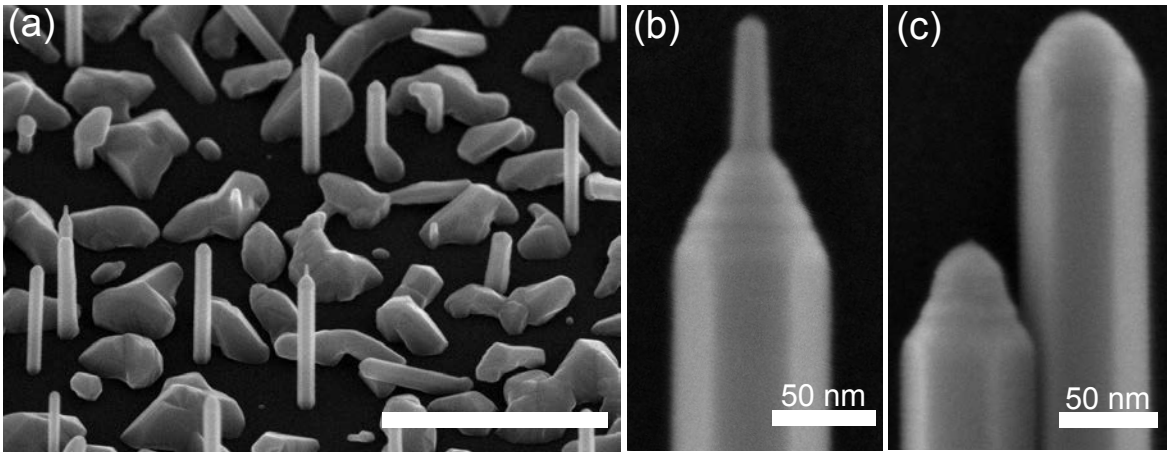

Fig. 6.10 Two-step growth of GaAs NWs. a) 45° view of the sample, scale bar is 5 μm; b) needle-like NW tip; c) dome-shaped tips.

Strictly speaking, we would say that the V/III ratio is *balanced* when the volume of the droplet does not change with time. However, even minuscule deviations from such optimal V/III ratio would accumulate over time, leading to either continuous expansion or shrinkage of the droplet, and therefore to tapered NWs. In practice, tapered NWs are rarely observed, which implies that the droplet size and NW diameter somehow adjust themselves to the V/III ratio, and several theoretical efforts have been recently made to understand this self-equilibration mechanism [36, 37, 136]. The discussion is further complicated by the fact that the V/III ratio at the NW tip may change as the NW elongates (reducing the diffusion contribution from the substrate) and the surrounding surfaces evolve (causing shadowing and different As re-emission), making it difficult to predict the final diameters as a function of the growth conditions. Recently, very thin NWs (down to 7 nm) were fabricate via a "reverse-reaction" process, by annealing already-grown self-catalyzed GaAs NWs [88]. However, such a technique may result in roughening of the NW sidewalls, as opposed to the atomically-smooth sidewalls obtained by VLS growth alone [102].

In this section, we present preliminary results on the growth of self-catalyzed GaAs and GaP NWs at high V/III ratios, on Si(111) covered with native oxide, that is, without particular substrate preparation procedures. In order to be sure that NWs have formed on the substrate, we started our experiments on GaAs NWs grown for 10 min in standard conditions [6] at 610 °C, followed by a gradual As BEP increase over 15 min from 3.0×10^{-6} Torr to 8.7×10^{-6} Torr, which corresponds to 90% of the As cell valve aperture, while the Ga cell is kept open. The result of this experiment is shown in Fig. 6.10.

[6] Ga rate of 2 Å s^{-1} and As/Ga BPR=12.

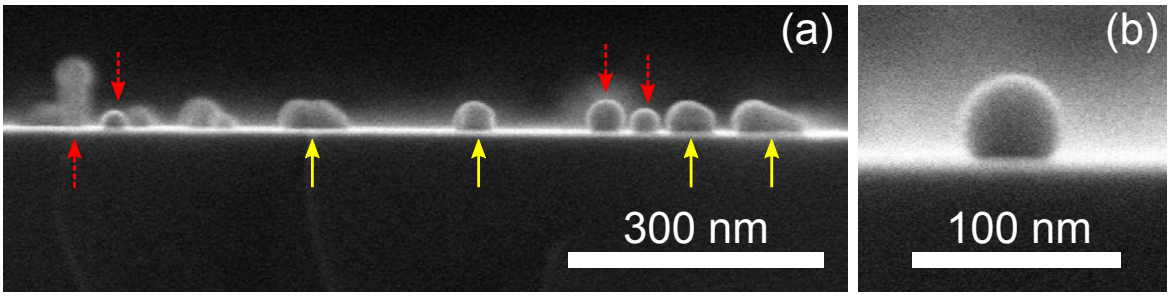

Fig. 6.11 1 min growth of GaAs NWs in standard conditions. a) cross-sectional view of the sample. Continuous yellow arrows indicate the crystallites, whereas dashed red arrows indicate NWs; b) close-up of a Ga droplet sitting on a short NW segment. The droplet contact angle β is 120°.

We see that the diameter of pre-grown NWs is about 65 nm (as typically observed in standard growth conditions) and that the droplet was consumed during the As ramp. The tip morphology is not uniform, with a predominance of dome-shaped tips (Fig. 6.10c) and a few needle-like tips (Fig. 6.10b). The pointed tips have a diameter of only 15 nm. The spread of tip morphologies might result from the slightly different local growth conditions at the different locations. The tips observed in this experiment are different from those obtained when the droplet is consumed at constant As flux, which usually results in flat tips [78, 116]. Although this experiment did not produce a continuation of VLS growth with reduced diameters, it indicates that a gradual change of the V/III ratio during growth might allow one to tune the droplet diameter and to shape the NW tip at will.

Instead of trying to reduce the NW diameter after 10 min of growth in standard conditions, when the NW diameter is quite large, we decided to change the V/III ratio after 1 min. This approach is based on the hypothesis that NWs have smaller diameters right at their formation. This hypothesis was experimentally verified by growing a GaAs NW sample in standard condition for 1 min and observing the results, shown in Fig. 6.11, where the base diameters of the droplets are only 30 nm on average.

Fig. 6.11 indicates that all NWs do not form at the same time, and a dispersion of droplet sizes is observed. However, after 1 min, all droplets are not any more in contact with the substrate, and contact angles are similar to those observed after long growths. It is interesting to note that *all* structures on the substrate (both NWs and crystallites) have a droplet attached to them, which means that crystallites are likely the result of a "failed" NW growth and are not formed by vapor-solid deposition alone.

We grew a series of samples in which, after the first minute of growth, we opened the As valve *abruptly* to 90% and continued growth for 10 min. In contrast with the first sample (gradual As opening), consumption of the droplet does not occur (Fig. 6.12a), although the

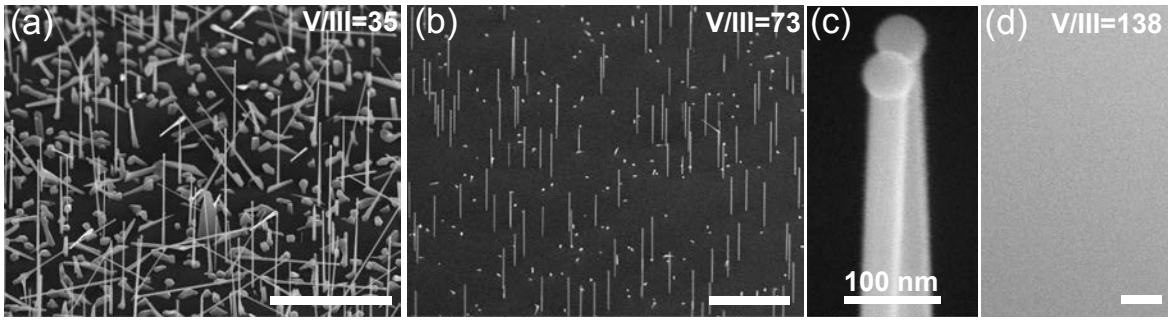

Fig. 6.12 Growth of GaAs NWs at 610 °C under constant As flux. V/III ratios refer to BPR measured prior to growth. a) V/III BPR 35; b) V/III BPR 73; c) detail of the NWs in panel b); d) V/III BPR 138. Scale bars in panels a) b) and d) are 5 μm.

reason for this is not clear at present. Growth experiments using the As valve opened to 100% (BEP 1.1×10^{-5} Torr) were not distinguishable from those performed with the valve at 90 %. Instead of changing the As flux, which is already close to the maximum attainable by the cell, we reduced the Ga flux from 2 Å/s (Fig. 6.12a) to 1 Å/s (Fig. 6.12b) and 0.5 Å/s (Fig. 6.12d).

The NWs in the first sample have lengths of about 5 μm and diameters of 30 nm, on average. In the second one, NWs are shorter, averaging 3.5 μm in length and 20 nm in diameter. Both in the first and second sample, NWs with diameters of 15 nm are occasionally observed. As in the first sample, NWs in the second sample present nice, round droplets at their top (Fig. 6.12c). In the third one (6.12d), the V/III ratio is too high to allow the formation of Ga droplets and no structures (neither NWs nor crystallites) are formed. Although this is a limited series of samples, we see that reduction of the Ga flux allows one to reduce the NW diameter (at constant As flux). Moreover, the formation of parasitic structures is also reduced and NW verticality is improved. We speculate that, right at the NW formation, droplets inflate more quickly with larger Ga fluxes. Such inflation leads to the formation of NWs with large diameters or, when excessive, to the failure of NW growth and transition to crystallite growth. Further diameter reduction may be obtained by reduction of the growth time in standard conditions, in order to obtain even thinner NW bases. Another strategy would be to increase supersaturation by lowering the growth temperature, thereby enhancing the axial growth rate while keeping the same As flux. However, reduction of the growth temperature may also favor radial growth. Such an experiment was attempted, using a compromise temperature of 590 °C, but no difference in NW diameters was found compared to the experiments presented above.

The situation seems to be a little more complicated in the case of GaP NWs. In Chapter 4, we have seen that both materials can be grown at 610 °C, and that their growth rates are

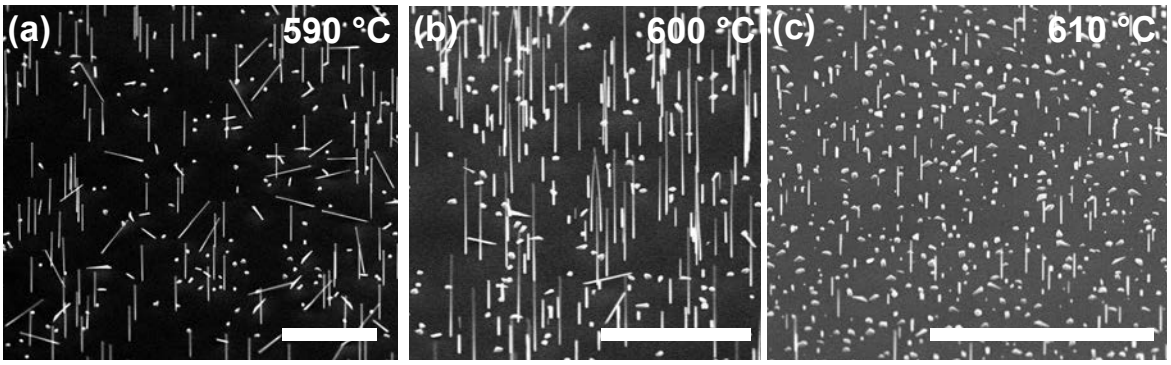

Fig. 6.13 Single-step, 10 min growth of GaP NWs at different temperatures: a) 590 °C; b) 600 °C; c) 610 °C.; scale bars are 5 μm.

roughly the same when the P/As BPR is 7/10. In Fig. 6.13 we show the result of 10 min growth using a P_2 BEP of 6.0×10^{-6} Torr, which should produce the same NW growth rate as in the experiments with GaAs shown in Fig. 6.12. The Ga flux was set to 1 Å/s, the value that gave the best results in the case of GaAs. We tested three different temperatures: 590, 600 and 610 °C. These samples have been grown in a single step, without change of the V/III ratio, as this supplementary step revealed itself unnecessary to form GaP NWs.

The diameters measured on the samples grown at 590 and 600 °C are 30 nm on average, although the NWs grown at 600 °C are denser and longer (approximately 4 μm compared to 2.5 μm). The distribution of diameters is quite broad and NWs with diameters of 15 nm are occasionally found. At 610 °C, the droplets are all consumed and only very short NW segments are found. In an attempt at reducing the diameters, a higher P flux of 8.0×10^{-6} was tested, which however always led to the disappearance of Ga droplets, regardless of the temperature.

The reason why our strategy was not effective at reducing the diameter of GaP NWs below 30 nm, whereas GaAs NWs diameters were reduced to 20 nm, is not clear yet. The form in which the group V species are supplied may play a role. As is provided as As_4 tetramers, while P_4 is cracked to P_2 dimers to avoid the accumulation of white phosphorus in the chamber (P_4 is a hazard when the MBE chamber is opened for maintenance). For Au-catalyzed GaAs NWs, it was shown that using As_2 instead of As_4 reduces the axial growth rate while at the same time increasing the radial growth rate [124]. By analogy, a similar phenomenon can be expected for P species. However, as pointed out at the beginning of this section, the mechanism of radial growth in self-catalyzed NWs is not yet fully understood and further investigations will be necessary to address this point.

General conclusions and perspectives

In this final section, we summarize the main results of the present thesis and we give perspectives for future work. The first part of the manuscript was devoted to understanding the mechanism of polytype formation. To this end, we analyzed the stacking sequence of InP NWs presenting a mixed crystal phase. These NWs are useful for applications, and since their electronic properties are degraded by stacking disorder, understanding of the latter is essential to improve them. This allowed us to uncover spatial correlation between MLs. The conditional probabilities, expressing the chances that a nucleus has to form in hexagonal or cubic position, given the position of the previous MLs, were connected to the nucleation rate to extract the differences in the nucleus work of formation. Such treatment yielded a system of equations that could not be satisfied without some form of interaction between MLs. Introduction of a stack-dependent nucleus-solid energy, as suggested by other authors, did not produced any quantitative agreement with the experiment. A quantitative agreement was found only by making the nucleus edge energy dependent on the stacking sequence. Although this does not represent a proof of mechanism, it strongly suggests that, if the nucleation takes place at the triple phase line (which is likely), the NW sidewalls are responsible for this interaction, possibly via surface reconstruction.

Then we focused on the growth of axial heterostructures in self-catalyzed NWs. In order to exploit quantum effects, it is important to control precisely the composition profiles at the interfaces, and these often need to be sharp. Because of the droplet reservoir effect, the interface abruptness of axial heterostructures is generally worse than that obtained in core-shell or planar heterostructures. Moreover, it is commonly believed that the high solubility of the NW constituents in the droplet is the main obstacle to obtain sharp interfaces. Since group V elements have a low solubility in Ga, we decided that the Ga(As,P) system was the ideal candidate for the realization of GaAs insertions with precisely controlled thickness and interfaces. The first problem we tackled is the growth of self-catalyzed GaP NWs, for which the literature was very scarce and our laboratory had not developed any growth protocol. After having succeeded in growing pure GaP NWs, we attempted to fabricate GaAs/GaP heterostructures. Surprisingly, we discovered that the interfaces were not sharp.

By performing flux measurements with high temporal resolution, we found that the group V background pressure in the MBE chamber was the main responsible for the interface broadness. The detrimental effect of the group V background pressure was limited by performing flux interruptions, which however introduced further complications, notably the appearance of truncation facets at the growth front. The observation of truncation facets only when the fluxes are interrupted for long durations, led us to formulate the hypothesis that such facets are not present in all growth conditions, but only at low enough supersaturation. This observation sheds light on the fact that truncation facets are commonly observed in in-situ TEM experiments but are not noticeable in heterostructures grown in standard conditions.

To investigate further the problem of reservoir effect, we also produced axial heterostructures in the (Al,Ga)As system. Since Al is fully soluble in liquid Ga, one would expect the interfaces to be broad, or at least broader than those obtained using group V elements. Instead, we found that the interfaces were fairly sharp, in any case much sharper than what was reported for gold-catalyzed NWs. By optimizing the growth recipe (using droplet pre-filling) we succeeded in obtaining very sharp interfaces. Since the Al-Ga-As system is well known and plenty of thermodynamic data are available, we looked at the liquid-solid equilibrium data and found a striking similarity between our estimates of the liquid and solid compositions with those found in the phase diagram. Interestingly, the equilibrium Al fraction in the liquid is much lower than in the equilibrium solid, and growth of $Al_xGa_{1-x}As$ with $x = 90\%$ using a Ga droplet would require only 1% of Al in the liquid. Actually, it is not the solubility of Al in Ga that matters, but the solubility of Al in the Ga-As liquid. By analogy, we would expect a similar behavior in the In-Ga-As system, where Ga will tend to incorporate faster than In into the solid. Therefore, we could imagine growing GaAs NWs using a catalyst made almost entirely of In. An In catalyst would also be the only way of getting In incorporated into the solid. This would explain the difficulties encountered by the authors of Ref. [65] at reaching In contents higher than 5% in Ga-catalyzed NWs (which, to the best of our knowledge, is the only report on the subject). In any case, using the equilibrium thermodynamic data, we built a model which predicts the interface composition of single MLs within experimental error. Such model suggested that atomically sharp interfaces would be attainable in self-catalyzed (Al,Ga)As NWs with small diameters ($\leq$ 20 nm).

While obtaining small diameters with a foreign catalyst is relatively easy, since the droplet volume is (almost) fixed and one can even buy monodispersed metal nanoparticles, in self-catalyzed NWs the diameter is determined by the complex (and evolving) material balance at the NW tip. As shown in Chapter 6, we successfully reduced the diameters of GaAs NWs down to 20 nm, while GaP was limited to 30 nm for reasons which are not yet clarified. However, such diameters would be small enough to start observing quantum effects

and to produce very sharp interfaces, since the reservoir effect is minimized (both for group III and group V elements, provided that the background pressure is not too high).

The group V background pressure in MBE can be minimized by lowering the group V fluxes. This is not only beneficial for the control of composition of the NWs and for interface abruptness, but may also lead to an improved control over the thickness of the insertions. In fact, nucleation being a random process, the number of MLs which are grown cannot be simply controlled with precision by controlling the growth time. While some dispersion of the segment length will always be present, we have shown that it is possible to minimize it by lowering the absolute fluxes or by pulsing the As source if short segments are desired.

These results, combined with the properties of self-catalyzed NWs (absence of metallic impurities, clear-cut and reversible switch between axial and radial growth, pure zinc-blende phase, etc.), open the way to the realization of complex structures in NWs with high degree of control, enabling for instance the growth of quantum dots with widely tunable dimensions and aspect ratios (with vastly extended possibilities of band gap engineering) or the combination of different types of quantum structures in the same NW, both for basic physics and applications.

References

[1] Akiyama, T., Nakamura, K., and Ito, T. (2006). Structural stability and electronic structures of InP nanowires: Role of surface dangling bonds on nanowire facets. *Phys. Rev. B*, 73:235308.

[2] Algra, R. E., Verheijen, M. A., Borgström, M. T., Feiner, L.-F., Immink, G., van Enckevort, W. J. P., Vlieg, E., and Bakkers, E. P. A. M. (2008). Twinning superlattices in indium phosphide nanowires. *Nature*, 456:369–372.

[3] Algra, R. E., Verheijen, M. A., Feiner, L.-F., Immink, G. G. W., van Enckevort, W. J. P., Vlieg, E., and Bakkers, E. P. A. M. (2011). The role of surface energies and chemical potential during nanowire growth. *Nano Lett.*, 11:1259–1264.

[4] Ambrosini, S., Fanetti, M., Grillo, V., Franciosi, A., and Rubini, S. (2011a). Self-catalyzed GaAs nanowire growth on Si-treated GaAs (100) substrates. *J. Appl. Phys.*, 109(9):094306.

[5] Ambrosini, S., Fanetti, M., Grillo, V., Franciosi, A., and Rubini, S. (2011b). Vapor-liquid-solid and vapor-solid growth of self-catalyzed GaAs nanowires. *AIP Adv.*, 1(4):042142.

[6] Ansara, I., Chatillon, C., Lukas, H. L., Nishizawa, T., Ohtani, H., Ishida, K., Hillert, M., Sundman, B., Argent, B. B., Watson, A., Chart, T., and Anderson, T. (1994). A binary database for III-V compound semiconductor systems. *Calphad*, 18:177–222.

[7] Ansara, I., Cornish, L., Gröbner, J., Tedenac, J.-C., and Wu, B. (2006). *Landolt-Börnstein - Group IV Physical Chemistry 11C1*. Springer-Verlag, Berlin Heidelberg.

[8] Arthur, J. and LePore, J. (1969). GaAs, GaP, and $GaAs_xP_{1-x}$ epitaxial films grown by molecular beam deposition. *J. Vac. Sci. Technol*, 6:545–548.

[9] Assali, S., Zardo, I., Plissard, S., Kriegner, D., Verheijen, M., Bauer, G., Meijerink, A., Belabbes, A., Bechstedt, F., Haverkort, J., et al. (2013). Direct band gap wurtzite gallium phosphide nanowires. *Nano Lett.*, 13(4):1559–1563.

[10] Balaghi, L., Tauchnitz, T., Hübner, R., Bischoff, L., Schneider, H., Helm, M., and Dimakis, E. (2016). Droplet-confined alternate pulsed epitaxy of GaAs nanowires on Si substrates down to CMOS-compatible temperatures. *Nano Lett.*, 16(7):4032–4039.

[11] Barns, R. and Ellis, W. (1965). Whisker crystals of gallium arsenide and gallium phosphide grown by the vapor—liquid—solid mechanism. *J. Appl. Phys.*, 36(7):2296–2301.

[12] Bechstedt, F. and Belabbes, A. (2013). Structure, energetics, and electronic states of III-V compound polytypes. *J. Phys.: Condens. Matter*, 25(27):273201.

[13] Belabbes, A., Panse, C., Furthmüller, J., and Bechstedt, F. (2012). Electronic bands of III-V semiconductor polytypes and their alignment. *Phys. Rev. B*, 86(7):075208.

[14] Björk, M. T., Ohlsson, B. J., Sass, T., Persson, A. I., Thelander, C., Magnusson, M. H., Deppert, K., Wallenberg, L. R., and Samuelson, L. (2002). One-dimensional steeplechase for electrons realized. *Nano Lett.*, 2:87–89.

[15] Borgström, M. T., Verheijen, M. A., Immink, G., de Smet, T., and Bakkers, E. P. A. M. (2006). Interface study on heterostructured GaP-GaAs nanowires. *Nanotechnology*, 17:4010–4013.

[16] Boulanger, J. and LaPierre, R. (2014). Unveiling transient GaAs/GaP nanowire growth behavior using group V oscillations. *J. Crys. Growth*, 388:116–123.

[17] Bryllert, T., Wernersson, L.-E., Löwgren, T., and Samuelson, L. (2006). Vertical wrap-gated nanowire transistors. *Nanotechnology*, 17(11):S227.

[18] Bugajski, M., Kontkiewicz, A., and Mariette, H. (1983). Energy bands of ternary alloy semiconductors: coherent-potential-approximation calculations. *Phys. Rev. B*, 28(12):7105.

[19] Carlino, E. and Grillo, V. (2005). Atomic-resolution quantitative composition analysis using scanning transmission electron microscopy Z-contrast experiments. *Phys. Rev. B*, 71:235303.

[20] Chan, C. K., Zhang, X. F., and Cui, Y. (2008). High capacity Li ion battery anodes using Ge nanowires. *Nano Lett.*, 8(1):307–309.

[21] Chauvin, N., Alouane, M. H., Anufriev, R., Khmissi, H., Naji, K., Patriarche, G., Bru-Chevallier, C., and Gendry, M. (2012). Growth temperature dependence of exciton lifetime in wurtzite InP nanowires grown on silicon substrates. *Appl. Phys. Lett.*, 100(1):011906.

[22] Chen, C., Braidy, N., Couteau, C., Fradin, C., Weihs, G., and LaPierre, R. (2008). Multiple quantum well AlGaAs nanowires. *Nano Lett.*, 8(2):495–499.

[23] Cheng, C., Needs, R., and Heine, V. (1988). Inter-layer interactions and the origin of SiC polytypes. *J. Phys. C*, 21(6):1049.

[24] Cirlin, G. E., Dubrovskii, V. G., Samsonenko, Y. B., Bouravleuv, A. D., Durose, K., Proskuryakov, Y. Y., Mendes, B., Bowen, L., Kaliteevski, M. A., Abram, R. A., and Zeze, D. (2010). Self-catalyzed, pure zincblende GaAs nanowires grown on Si(111) by molecular beam epitaxy. *Phys. Rev. B*, 82:035302.

[25] Clark, T. E., Nimmatoor, P., Lew, K.-K., Pan, L., Redwing, J. M., and Dickey, E. C. (2008). Diameter dependent growth rate and interfacial abruptness in vapor-liquid-solid $Si/Si_{1-x}Ge_x$ heterostructure nanowires. *Nano Lett.*, 8:1246–1252.

[26] Collins, C. B., Carlson, R. O., and Gallagher, C. J. (1957). Properties of gold-doped silicon. *Phys. Rev.*, 105:1168–1173.

[27] Colombo, C., Spirkoska, D., Frimmer, M., Abstreiter, G., and Fontcuberta i Morral, A. (2008). Ga-assisted catalyst-free growth mechanism of GaAs nanowires by molecular beam epitaxy. *Phys. Rev. B*, 77:155326.

[28] Corless, R. M., Gonnet, G. H., Hare, D. E., Jeffrey, D. J., and Knuth, D. E. (1996). On the Lambert W function. *Adv. Comput. Math.*, 5(1):329–359.

[29] Dash, J. G. (1977). Clustering and percolation transitions in helium and other thin films. *Phys. Rev. B*, 15:3136.

[30] Dheeraj, D. L., Patriarche, G., Zhou, H., Hoang, T. B., Moses, A. F., Grønsberg, S., van Helvoort, A. T. J., Fimland, B.-O., and Weman, H. (2008). Growth and characterization of wurtzite GaAs nanowires with defect-free zinc blende GaAsSb inserts. *Nano Lett.*, 8:4459–4463.

[31] Dick, K. A., Bolinsson, J., Borg, B. M., and Johansson, J. (2012). Controlling the abruptness of axial heterojunctions in III-V nanowires: beyond the reservoir effect. *Nano Lett.*, 12(6):3200–3206.

[32] Dick, K. A. and Caroff, P. (2014). Metal-seeded growth of III–V semiconductor nanowires: towards gold-free synthesis. *Nanoscale*, 6(6):3006–3021.

[33] Dick, K. A., Kodambaka, S., Reuter, M. C., Deppert, K., Samuelson, L., Seifert, W., Wallenberg, L. R., , and Ross, F. M. (2007). The morphology of axial and branched nanowire heterostructures. *Nano Lett.*, 7:1817–1822.

[34] Duan, X., Huang, Y., Agarwal, R., and Lieber, C. M. (2003). Single-nanowire electrically driven lasers. *Nature*, 421(6920):241–245.

[35] Duan, X. and Lieber, C. M. (2000). General synthesis of compound semiconductor nanowires. *Adv. Mater.*, 12:298–302.

[36] Dubrovskii, V., Berdnikov, Y., and Sibirev, N. (2016). Regimes of radial growth for Ga-catalyzed GaAs nanowires. *Appl. Phys. A*, 122(7):1–7.

[37] Dubrovskii, V., Xu, T., Álvarez, A. D., Plissard, S., Caroff, P., Glas, F., and Grandidier, B. (2015). Self-equilibration of the diameter of Ga-catalyzed GaAs nanowires. *Nano Lett.*, 15(8):5580–5584.

[38] Dubrovskii, V. G., Cirlin, G. E., Soshnikov, I. P., Tonkikh, A. A., Sibirev, N. V., Samsonenko, Y. B., and Ustinov, V. M. (2005). Diffusion-induced growth of GaAs nanowhiskers during molecular beam epitaxy: Theory and experiment. *Phys. Rev. B*, 71:205325.

[39] Dubrovskii, V. G. and Sibirev, N. V. (2016). Factors influencing the interfacial abruptness in axial III–V nanowire heterostructures. *Cryst. Growth Des.*, 16(4):2019–2023.

[40] Dubrovskii, V. G., Sibirev, N. V., Harmand, J. C., and Glas, F. (2008). Growth kinetics and crystal structure of semiconductor nanowires. *Phys. Rev. B*, 78:235301.

[41] Ferrand, D. and Cibert, J. (2014). Strain in crystalline core-shell nanowires. *Eur. Phys. J. Appl. Phys.*, 67(3):30403.

[42] Fisher, M. E. and Selke, W. (1980). Infinitely many commensurate phases in a simple Ising model. *Phys. Rev. Lett.*, 44(23):1502.

[43] Fontcuberta i Morral, A., Colombo, C., Abstreiter, G., Arbiol, J., and Morante, J. R. (2008). Nucleation mechanism of gallium-assisted molecular beam epitaxy growth of gallium arsenide nanowires. *Appl. Phys. Lett.*, 92:063112.

[44] Fortuna, S. A. and Li, X. (2010). Metal-catalyzed semiconductor nanowires: a review on the control of growth directions. *Semicond. Sci. Technol.*, 25(2):024005.

[45] Gamalski, A. D., Ducati, C., and Hofmann, S. (2011). Cyclic supersaturation and triple phase boundary dynamics in germanium nanowire growth. *J. Phys. Chem. C*, 115:4413–4417.

[46] Ghaderi, N., Peressi, M., Binggeli, N., and Akbarzadeh, H. (2010). Structural properties and energetics of intrinsic and Si-doped GaAs nanowires: First-principles pseudopotential calculations. *Phys. Rev. B*, 81(15):155311.

[47] Givargizov, E. I. (1975). Fundamental aspects of VLS growth. *J. Cryst. Growth*, 31:20–30.

[48] Glas, F. (2006). Critical dimensions for the plastic relaxation of strained axial heterostructures in free-standing nanowires. *Phys. Rev. B*, 74:121302.

[49] Glas, F. (2010a). Chemical potentials for Au-assisted vapor-liquid-solid growth of III-V nanowires. *J. Appl. Phys.*, 108:073506.

[50] Glas, F. (2010b). Vapor fluxes on the apical droplet during nanowire growth by molecular beam epitaxy. *Phys. Stat. Sol. B*, 247:254–258.

[51] Glas, F. (2014). Statistics of sub-Poissonian nucleation in a nanophase. *Phys. Rev. B*, 90(12):125406.

[52] Glas, F., Harmand, J. C., and Patriarche, G. (2007). Why does wurtzite form in nanowires of III-V zinc blende semiconductors? *Phys. Rev. Lett.*, 99:146101.

[53] Glas, F., Harmand, J. C., and Patriarche, G. (2010). Nucleation antibunching in catalyst-assisted nanowire growth. *Phys. Rev. Lett.*, 104:135501.

[54] Glas, F., Ramdani, M. R., Patriarche, G., and Harmand, J.-C. (2013). Predictive modeling of self-catalyzed III-V nanowire growth. *Phys. Rev. B*, 88(19):195304.

[55] Glass, R., Henshall, D., Tsvetkov, V., and Carter, C. (1997). SiC-seeded crystal growth. *MRS Bull.*, 22(03):30–35.

[56] Goldberger, J., Hochbaum, A. I., Fan, R., and Yang, P. (2006). Silicon vertically integrated nanowire field effect transistors. *Nano Lett.*, 6(5):973–977.

[57] Gomes, U. P., Ercolani, D., Zannier, V., David, J., Gemmi, M., Beltram, F., and Sorba, L. (2016). Nucleation and growth mechanism of self-catalyzed InAs nanowires on silicon. *Nanotechnology*, 27(25):255601.

[58] Gudiksen, M. S., Lauhon, L. J., Wang, J., Smith, D. C., and Lieber, C. M. (2002). Growth of nanowire superlattice structures for nanoscale photonics and electronics. *Nature*, 415:617–620.

[59] Guo, J., Huang, H., Ding, Y., Ji, Z., Liu, M., Ren, X., Zhang, X., and Huang, Y. (2012). Growth of zinc blende GaAs/AlGaAs heterostructure nanowires on Si substrate by using AlGaAs buffer layers. *J. Crys. Growth*, 359:30–34.

[60] Guo, J., Huang, H., Ren, X., Yan, X., Cai, S., Huang, Y., Wang, Q., Zhang, X., and Wang, W. (2011). Stacking-faults-free zinc blende GaAs/AlGaAs axial heterostructure nanowires during vapor-liquid-solid growth. *Chin. Opt. Lett.*, 9(4):041601.

[61] Harmand, J.-C., Glas, F., and Patriarche, G. (2010). Growth kinetics of a single $InP_{1-x}As_x$ nanowire. *Phys. Rev. B*, 81:235436.

[62] Harmand, J. C., Patriarche, G., Péré-Laperne, N., Mérat-Combes, M.-N., Travers, L., and Glas, F. (2005). Analysis of vapor-liquid-solid mechanism in Au-assisted GaAs nanowire growth. *Appl. Phys. Lett.*, 87:203101.

[63] Harris, J., Joyce, B., and Dobson, P. (1981). Oscillations in the surface structure of Sn-doped GaAs during growth by MBE. *Surf. Sci. Lett.*, 103(1):L90–L96.

[64] Hayashida, A., Sato, T., Hara, S., Motohisa, J., Hiruma, K., and Fukui, T. (2010). Fabrication and characterization of GaAs quantum well buried in AlGaAs/GaAs heterostructure nanowires. *J. Crys. Growth*, 312(24):3592–3598.

[65] Heiß, M., Gustafsson, A., Conesa-Boj, S., PeirŽo, F., Morante, J. R., Abstreiter, G., Arbiol, J., Samuelson, L., and Fontcuberta i Morral, A. (2009). Catalyst-free nanowires with axial $InGa_{1-x}As_x$/GaAs heterostructures. *Nanotechnology*, 20:075603.

[66] Hiruma, K., Yasawa, M., Katsuyama, T., Ogawa, K., Haraguchi, K., Koguchi, M., and Kakibayashi, H. (1995). Growth and optical properties of nanometer-scale GaAs and InAs whiskers. *J. Appl. Phys.*, 77:447–462.

[67] Hofmann, S., Sharma, R., Wirth, C. T., Cervantes-Sodi, F., Ducati, C., Kasama, T., Dunin-Borkowski, R. E., Drucker, J., Bennett, P., and Robertson, J. (2008). Ledge-flow-controlled catalyst interface dynamics during Si nanowire growth. *Nat. Mater.*, 7(5):372–375.

[68] Holm, J. V., Jørgensen, H. I., Krogstrup, P., Nygård, J., Liu, H., and Aagesen, M. (2013). Surface-passivated GaAsP single-nanowire solar cells exceeding 10% efficiency grown on silicon. *Nat. Commun.*, 4:1498.

[69] Huang, M. H., Mao, S., Feick, H., Yan, H., Wu, Y., Kind, H., Weber, E., Russo, R., and Yang, P. (2001). Room-temperature ultraviolet nanowire nanolasers. *Science*, 292(5523):1897–1899.

[70] Hurle, D. (1995). A mechanism for twin formation during Czochralski and encapsulated vertical bridgman growth of III-V compound semiconductors. *J. Cryst. Growth*, 147(3):239–250.

[71] Jabeen, F., Grillo, V., Rubini, S., and Martelli, F. (2008). Self-catalyzed growth of GaAs nanowires on cleaved Si by molecular beam epitaxy. *Nanotechnology*, 19:275711.

[72] Jabeen, F., Patriarche, G., Glas, F., and Harmand, J.-C. (2011). GaP/$GaAs_{1-x}P_x$ nanowires fabricated with modulated fluxes: A step towards the realization of superlattices in a single nanowire. *J. Cryst. Growth*, 323:293 – 296.

[73] Jacobsson, D., Panciera, F., Tersoff, J., Reuter, M. C., Lehmann, S., Hofmann, S., Dick, K. A., and Ross, F. M. (2016). Interface dynamics and crystal phase switching in GaAs nanowires. *Nature*, 531(7594):317–322.

[74] Johansson, J., Bolinsson, J., Ek, M., Caroff, P., and Dick, K. A. (2012). Combinatorial approaches to understanding polytypism in III-V nanowires. *ACS Nano*, 6(7):6142–6149.

[75] Johansson, J., Karlsson, L. S., Svensson, C. P. T., Mårtensson, T., Wacaser, B. A., Deppert, K., Samuelson, L., and Seifert, W. (2006). Structural properties of 111 B-oriented III-V nanowires. *Nature Mater.*, 5:574–580.

[76] Johnson, J. C., Choi, H.-J., Knutsen, K. P., Schaller, R. D., Yang, P., and Saykally, R. J. (2002). Single gallium nitride nanowire lasers. *Nat. Mater.*, 1(2):106–110.

[77] Kim, H. and Cho, J. (2008). Superior lithium electroactive mesoporous Si@ carbon core- shell nanowires for lithium battery anode material. *Nano Lett.*, 8(11):3688–3691.

[78] Kim, Y. H., Park, D. W., and Lee, S. J. (2012). Gallium-droplet behaviors of self-catalyzed GaAs nanowires: A transmission electron microscopy study. *Appl. Phys. Lett.*, 100:033117.

[79] Klenov, D. O. and Stemmer, S. (2006). Contributions to the contrast in experimental high-angle annular dark-field images. *Ultramicroscopy*, 106(10):889–901.

[80] Kodambaka, S., Tersoff, J., Reuter, M., and Ross, F. (2007). Germanium nanowire growth below the eutectic temperature. *Science*, 316(5825):729–732.

[81] Kohno, H., Yoshida, H., Ichikawa, S., and Takeda, S. (2009). Statistical and stochastic properties of stacking sequences in SiC nanowires. *J. Phys. Soc. Jpn.*, 78(4):044601.

[82] Krogstrup, P., Popovitz-Biro, R., Johnson, E., Madsen, M. H., Nygård, J., and Shtrikman, H. (2010). Structural phase control in self-catalyzed growth of GaAs nanowires on silicon (111). *Nano Lett.*, 10:4475–4482.

[83] Kuang, Y., Sukrittanon, S., Li, H., and Tu, C. (2012). Growth and photoluminescence of self-catalyzed GaP/GaNP core/shell nanowires on Si (111) by gas source molecular beam epitaxy. *Appl. Phys. Lett.*, 100(5):053108.

[84] Larsson, M. W., Wagner, J. B., Wallin, M., Håkansson, P., Fröberg, L. E., Samuelson, L., and Wallenberg, L. R. (2007). Strain mapping in free-standing heterostructured wurtzite InAs/InP nanowires. *Nanotechnology*, 18:015504.

[85] Li, C., Li, J.-B., Du, Z., Lu, L., and Zhang, W. (2001). A thermodynamic reassessment of the Al-As-Ga system. *J. Phase Equilib.*, 22(1):26–33.

[86] Li, N., Tan, T. Y., and Gösele, U. (2008). Transition region width of nanowire hetero-and pn-junctions grown using vapor–liquid–solid processes. *Appl. Phys. A*, 90(4):591–596.

[87] Limpijumnong, S. and Lambrecht, W. R. (1998). Total energy differences between SiC polytypes revisited. *Phys. Rev. B*, 57(19):12017.

[88] Loitsch, B., Rudolph, D., Morkötter, S., Döblinger, M., Grimaldi, G., Hanschke, L., Matich, S., Parzinger, E., Wurstbauer, U., Abstreiter, G., et al. (2015). Tunable quantum confinement in ultrathin, optically active semiconductor nanowires via reverse-reaction growth. *Adv. Mater.*, 27(13):2195–2202.

[89] Lukas, H. L., Fries, S. G., and Sundman, B. (2007). *Computational thermodynamics: the Calphad method*, volume 131. Cambridge university press Cambridge.

[90] Magri, R., Rosini, M., and Casetta, F. (2010). Structural stability of clean GaAs nanowires grown along the [111] direction. *Phys. Status Solidi C*, 7(2):374–377.

[91] Mandl, B., Dick, K. A., Kriegner, D., Keplinger, M., Bauer, G., Stangl, J., and Deppert, K. (2011). Crystal structure control in Au-free self-seeded InSb wire growth. *Nanotechnology*, 22(14):145603.

[92] Markov, I. V. (2003). *Crystal growth for beginners*. World Scientific, Singapore.

[93] Markov, I. V. (2010). *Nucleation at surfaces*, pages 17–52. Springer Handbook of Crystal Growth. Springer.

[94] Martelli, F., Rubini, S., Piccin, M., Bais, G., Jabeen, F., De Franceschi, S., Grillo, V., Carlino, E., D'Acapito, F., Boscherini, F., et al. (2006). Manganese-induced growth of GaAs nanowires. *Nano Lett.*, 6(9):2130–2134.

[95] Matteini, F., Tütüncüoğlu, G., Potts, H., Jabeen, F., and Fontcuberta i Morral, A. (2015). Wetting of Ga on SiOx and its impact on GaAs nanowire growth. *Cryst. Growth Des.*, 15(7):3105–3109.

[96] Matteini, F., Tütüncüoğlu, G., Rüffer, D., Alarcón-Lladó, E., and i Morral, A. F. (2014). Ga-assisted growth of GaAs nanowires on silicon, comparison of surface SiOx of different nature. *J. Crys. Growth*, 404:246–255.

[97] McLean, D. (1957). *Grain boundaries in metals*. Clarendon Press New York.

[98] Messing, M. E., Hillerich, K., Johansson, J., Deppert, K., and Dick, K. A. (2009). The use of gold for fabrication of nanowire structures. *Gold bulletin*, 42(3):172.

[99] Mohan, P., Motohisa, J., and Fukui, T. (2005). Controlled growth of highly uniform, axial/radial direction-defined, individually addressable InP nanowire arrays. *Nanotechnology*, 16:2903–2907.

[100] Noborisaka, J., Motohisa, J., and Fukui, T. (2005). Catalyst-free growth of GaAs nanowires by selective-area metalorganic vapor-phase epitaxy. *Appl. Phys. Lett.*, 86(21):213102.

[101] Oh, S. H., Chisholm, M. F., Kauffmann, Y., Kaplan, W. D., Luo, W., Rühle, M., and Scheu, C. (2010). Oscillatory mass transport in vapor-liquid-solid growth of sapphire nanowires. *Science*, 330:489.

[102] Ouattara, L., Mikkelsen, A., Sköld, N., Eriksson, J., Knaapen, T., Ćavar, E., Seifert, W., Samuelson, L., and Lundgren, E. (2007). GaAs/AlGaAs nanowire heterostructures studied by scanning tunneling microscopy. *Nano Lett.*, 7:2859–2864.

[103] Paek, J. H., Nishiwaki, T., Yamaguchi, M., and Sawaki, N. (2009). Catalyst free mbe-vls growth of GaAs nanowires on (111)si substrate. *Phys. Status Solidi C*, 6:1436–1440.

[104] Paladugu, M., Zou, J., Guo, Y.-N., Auchterlonie, G. J., Joyce, H. J., Gao, Q., Hoe Tan, H., Jagadish, C., and Kim, Y. (2007). Novel growth phenomena observed in axial InAs/GaAs nanowire heterostructures. *Small*, 3(11):1873–1877.

[105] Paladugu, M., Zou, J., Guo, Y. N., Zhang, X., Joyce, H. J., Gao, Q., Tan, H. H., Jagadish, C., and Kim, Y. (2009). Evolution of wurtzite structured GaAs shells around InAs nanowire cores. *Nanoscale Res. Lett.*, 4:846–849.

[106] Panish, M. and Sumski, S. (1969). Ga-Al-As: phase, thermodynamic and optical properties. *J. Phys. Chem. Solids*, 30(1):129–137.

[107] Pankoke, V., Kratzer, P., and Sakong, S. (2011). Calculation of the diameter-dependent polytypism in GaAs nanowires from an atomic motif expansion of the formation energy. *Phys. Rev. B*, 84(7):075455.

[108] Panse, C., Kriegner, D., and Bechstedt, F. (2011). Polytypism of GaAs, InP, InAs, and InSb: an ab initio study. *Phys. Rev. B*, 84(7):075217.

[109] Pantzas, K., Patriarche, G., Troadec, D., Gautier, S., Moudakir, T., Suresh, S., Largeau, L., Mauguin, O., Voss, P., and Ougazzaden, A. (2012). Nanometer-scale, quantitative composition mappings of InGaN layers from a combination of scanning transmission electron microscopy and energy dispersive x-ray spectroscopy. *Nanotechnology*, 23(45):455707.

[110] Perea, D. E., Li, N., Dickerson, R. M., Misra, A., and Picraux, S. (2011). Controlling heterojunction abruptness in VLS-grown semiconductor nanowires via in situ catalyst alloying. *Nano Lett.*, 11(8):3117–3122.

[111] Periwal, P., Sibirev, N. V., Patriarche, G., Salem, B., Bassani, F., Dubrovskii, V. G., and Baron, T. (2014). Composition-dependent interfacial abruptness in au-catalyzed $Si_{1-x}Ge_x$/Si/$Si_{1-x}Ge_x$ nanowire heterostructures. *Nano Lett.*, 14(9):5140–5147.

[112] Persson, A. I., Larsson, M. W., Stenstrom, S., Ohlsson, B. J., Samuelson, L., and Wallenberg, L. R. (2004). Solid-phase diffusion mechanism for GaAs nanowire growth. *Nature Mater.*, 3:678–681.

[113] Piccin, M., Bais, G., Grillo, V., Jabeen, F., De Franceschi, S., Carlino, E., Lazzarino, M., Romanato, F., Businaro, L., Rubini, S., et al. (2007). Growth by molecular beam epitaxy and electrical characterization of GaAs nanowires. *Physica E Low Dimens. Syst. Nanostruct.*, 37(1):134–137.

[114] Plissard, S., Dick, K. A., Larrieu, G., Godey, S., Addad, A., Wallart, X., and Caroff, P. (2010). Gold-free growth of GaAs nanowires on silicon: arrays and polytypism. *Nanotechnology*, 21(38):385602.

[115] Plissard, S., Larrieu, G., Wallart, X., and Caroff, P. (2011). High yield of self-catalyzed GaAs nanowire arrays grown on silicon via gallium droplet positioning. *Nanotechnology*, 22:275602.

[116] Priante, G., Ambrosini, S., Dubrovskii, V. G., Franciosi, A., and Rubini, S. (2013). Stopping and resuming at will the growth of GaAs nanowires. *Cryst. Growth Des.*, 13(9):3976–3984.

[117] Priante, G., Glas, F., Patriarche, G., Pantzas, K., Oehler, F., and Harmand, J.-C. (2016). Sharpening the interfaces of axial heterostructures in self-catalyzed AlGaAs nanowires: Experiment and theory. *Nano Lett.*, 16(3):1917–1924.

[118] Priante, G., Harmand, J.-C., Patriarche, G., and Glas, F. (2014). Random stacking sequences in III-V nanowires are correlated. *Phys. Rev. B*, 89(24):241301.

[119] Priante, G., Patriarche, G., Oehler, F., Glas, F., and Harmand, J.-C. (2015). Abrupt GaP/GaAs interfaces in self-catalyzed nanowires. *Nano Lett.*, 15(9):6036–6041.

[120] Ramdani, M. R., Harmand, J. C., Glas, F., Patriarche, G., and Travers, L. (2013). Arsenic pathways in self-catalyzed growth of GaAs nanowires. *Cryst. Growth Design*, 13:91–96.

[121] Ramsdell, L. S. (1947). Studies on silicon carbide. *Am. Mineral.*, 32(1-2):64–82.

[122] Rieger, T., Heiderich, S., Lenk, S., Lepsa, M. I., and Grützmacher, D. (2012). Ga-assisted mbe growth of GaAs nanowires using thin hsq layer. *J. Cryst. Growth*, 353:39 – 46.

[123] Rosenauer, A., Mehrtens, T., Müller, K., Gries, K., Schowalter, M., Satyam, P. V., Bley, S., Tessarek, C., Hommel, D., Sebald, K., et al. (2011). Composition mapping in InGaN by scanning transmission electron microscopy. *Ultramicroscopy*, 111(8):1316–1327.

[124] Sartel, C., Dheeraj, D. L., Jabeen, F., and Harmand, J. C. (2010). Effect of arsenic species on the kinetics of GaAs nanowires growth by molecular beam epitaxy. *J. Cryst. Growth*, 312:2073–2077.

[125] Shtrikman, H., Popovitz-Biro, R., Kretinin, A., and Heiblum, M. (2009). Stacking-faults-free zinc blende GaAs nanowires. *Nano Lett.*, 9:215–219.

[126] Somaschini, C., Bietti, S., Trampert, A., Jahn, U., Hauswald, C., Riechert, H., Sanguinetti, S., and Geelhaar, L. (2013). Control over the number density and diameter of GaAs nanowires on Si (111) mediated by droplet epitaxy. *Nano Lett.*, 13(8):3607–3613.

[127] Soshnikov, I., Cirlin, G., Sibirev, N., Dubrovskii, V., Samsonenko, Y. B., Litvinov, D., and Gerthsen, D. (2008). Hexagonal structures in GaAs nanowhiskers. *Tech. Phys. Lett.*, 34(6):538–541.

[128] Soshnikov, I. P., Cirlin, G. E., Tonkikh, A. A., Samsonenko, Y. B., Dubrovskii, V. G., Ustinov, V. M., Gorbenko, O. M., Litvinov, D., and Gerthsen, D. (2005). Atomic structure of MBE-grown GaAs nanowhiskers. *Phys. Sol. State*, 47:2121–2126.

[129] Spirkoska, D., Arbiol, J., Gustafsson, A., Conesa-Boj, S., Glas, F., Zardo, I., Heigoldt, M., Gass, M. H., Bleloch, A. L., Estrade, S., Kaniber, M., Rossler, J., Peiro, F., Morante, J. R., Abstreiter, G., Samuelson, L., and Fontcuberta i Morral, A. (2009). Structural and optical properties of high quality zinc-blende/wurtzite GaAs nanowire heterostructures. *Phys. Rev. B*, 80:245325.

[130] Spirkoska, D., Colombo, C., Heiss, M., Abstreiter, G., and Fontcuberta i Morral, A. (2008). The use of molecular beam epitaxy for the synthesis of high purity III–V nanowires. *J. Phys. Condens. Matter*, 20(45):454225.

[131] Sun, J., Liu, C., and Yang, P. (2011). Surfactant-free, large-scale, solution–liquid–solid growth of gallium phosphide nanowires and their use for visible-light-driven hydrogen production from water reduction. *J. Am. Chem. Soc.*, 133(48):19306–19309.

[132] Tatebayashi, J., Lin, A., Wong, P., Hick, R., and Huffaker, D. (2010a). Visible light emission from self-catalyzed GaInP/GaP core-shell double heterostructure nanowires on silicon. *J. Appl. Phys.*, 108(3):034315.

[133] Tatebayashi, J., Mariani, G., Lin, A., Hicks, R., and Huffaker, D. (2010b). Optical characteristics of GaInP/GaP double-heterostructure core-shell nanowires embedded in polydimethylsiloxane membranes. *Appl. Phys. Lett.*, 96(25):253101.

[134] Tateno, K., Gotoh, H., and Watanabe, Y. (2006). Multi-quantum structures of GaAs/AlGaAs free-standing nanowires. *Jpn. J. Appl. Phys.*, 45(4S):3568.

[135] Tchernycheva, M., Travers, L., Patriarche, G., Glas, F., Harmand, J.-C., Cirlin, G. E., and Dubrovskii, V. G. (2007). Au-assisted molecular beam epitaxy of InAs nanowires: Growth and theoretical analysis. *J. Appl. Phys.*, 102:094313.

[136] Tersoff, J. (2015). Stable self-catalyzed growth of III–V nanowires. *Nano Lett.*, 15(10):6609–6613.

[137] Thelander, C., Caroff, P., Plissard, S., Dey, A. W., and Dick, K. A. (2011). Effects of crystal phase mixing on the electrical properties of InAs nanowires. *Nano Lett.*, 11(6):2424–2429.

[138] Thelander, C., Mårtensson, T., Björk, M., Ohlsson, B., Larsson, M., Wallenberg, L., and Samuelson, L. (2003). Single-electron transistors in heterostructure nanowires. *Appl. Phys. Lett.*, 83(10):2052–2054.

[139] Wagner, R. S. (1970). *Whisker Technology*. Wiley & Sons, New York.

[140] Wagner, R. S. and Ellis, W. C. (1964). Vapor-liquid-solid mechanism of single crystal growth. *Appl. Phys. Lett.*, 4:89–90.

[141] Wan, Q. and Wang, T. (2005). Single-crystalline Sb-doped SnO_2 nanowires: synthesis and gas sensor application. *Chem. Commun.*, (30):3841–3843.

[142] Wang, J., Plissard, S. R., Verheijen, M. A., Feiner, L.-F., Cavalli, A., and Bakkers, E. P. (2013). Reversible switching of InP nanowire growth direction by catalyst engineering. *Nano Lett.*, 13(8):3802–3806.

[143] Wen, C.-Y., Reuter, M. C., Bruley, J., Tersoff, J., Kodambaka, S., Stach, E. A., and Ross, F. M. (2009). Formation of compositionally abrupt axial heterojunctions in silicon-germanium nanowires. *Science*, 326:1247.

[144] Wen, C.-Y., Tersoff, J., Hillerich, K., Reuter, M. C., Park, J. H., Kodambaka, S., Stach, E. A., and Ross, F. M. (2011). Periodically changing morphology of the growth interface in Si, Ge, and GaP nanowires. *Phys. Rev. Lett.*, 107:025503.

[145] Wu, Y., Fan, R., and Yang, P. (2002). Block-by-block growth of single-crystalline Si/SiGe superlattice nanowires. *Nano Lett.*, 2:83–86.

[146] Yeh, C.-Y., Lu, Z. W., Froyen, S., and Zunger, A. (1992). Zinc-blende-wurtzite polytypism in semiconductors. *Phys. Rev. B*, 46:10086.

[147] Yuan, X., Caroff, P., Wong-Leung, J., Fu, L., Tan, H. H., and Jagadish, C. (2015). Tunable polarity in a III-V nanowire by droplet wetting and surface energy engineering. *Adv. Mater.*, 27(40):6096–6103.

[148] Yuan, Z. and Nakano, A. (2013). Self-replicating twins in nanowires. *Nano Lett.*, 13:4925–4930.

[149] Zhang, Y., Aagesen, M., Holm, J. V., Jørgensen, H. I., Wu, J., and Liu, H. (2013). Self-catalyzed GaAsP nanowires grown on silicon substrates by solid-source molecular beam epitaxy. *Nano Lett.*, 13(8):3897–3902.

Appendix A

Computation of phase equilibrium for the Al-Ga-As system

We want to calculate the phase equilibrium of the ternary Al-Ga-As system. Chemical equilibrium between two or more phases is defined by the minimum of the total free energy G (of the entire system). However, finding the global minimum of G in several variables can be computationally tricky, especially when G has multiple local minima. The difficulty is circumvented by re-expressing the problem in terms of chemical potentialsμ, and requiring all chemical potentials to be the same for each species i and phase f. Indeed, at constant pressure p and temperature T the chemical potential is written:

$$\mu_i = \left(\frac{\partial G}{\partial N_i}\right)_{N_j} \tag{A.1}$$

from which we see that the equality of chemical potentials is equivalent to $dG = 0$.

In most practical situations, the characterizing variables are not the absolute number of particles of each species N_i, but rather the relative abundance, expressed by the molar fraction $x_i = N_i/N$, where $N = \sum N_i$. Eq. A.1 becomes:

$$\mu_i = g + \left(\frac{\partial g}{\partial x_i}\right)_{x_k} - \sum_j x_j \left(\frac{\partial g}{\partial x_j}\right)_{x_l}, k \neq i, l \neq j \tag{A.2}$$

where $g = G/N$ is the molar free energy. In our case, we want to find conditions for the liquid-solid equilibrium, which will be given by setting:

$$\begin{cases} \Delta\mu_{\mathrm{AlAs}} = \mu^l_{\mathrm{Al}} + \mu^l_{\mathrm{As}} - \mu^s_{\mathrm{AlAs}} = 0 \\ \Delta\mu_{\mathrm{GaAs}} = \mu^l_{\mathrm{Ga}} + \mu^l_{\mathrm{As}} - \mu^s_{\mathrm{GaAs}} = 0 \end{cases} \tag{A.3}$$

The liquid is fully characterized by the elemental mole fractions y_i (i=Ga, Al, As) and the stoichiometric solid is characterized by the AlAs and GaAs mole fractions $x_{\mathrm{AlAs}} = x$ and $x_{\mathrm{GaAs}} = 1 - x$. The constraints $\sum y_i = 1$ and $x_{\mathrm{AlAs}} + x_{\mathrm{GaAs}} = 1$ apply.

The Gibbs free energy of the liquid can be written as:

$$G^l = \sum_i y_i G_i^{0,l} + RT \sum_i y_i \ln y_i + \sum_{i \neq j} G_{i,j}^{E,l} + G_{\mathrm{Al,As,Ga}}^{E,l} \tag{A.4}$$

where $G_i^{0,l}$ is the standard Gibbs energy of pure element i. Superscript E denotes the exces energies associated with pairs and triplet components which, introducing the appropriate Redlich-Kister coefficients L, write $G_{i,j}^{E,l} = y_i y_j \sum_k L_{i,j}^{k,l} (y_i - y_j)^k$ and $G_{\mathrm{Al,As,Ga}}^{E,l} = y_{\mathrm{Al}} y_{\mathrm{Ga}} y_{\mathrm{As}} L_{\mathrm{Al}}^{l}$. Similarly, for the solid:

$$\begin{aligned} G^s = {} & x_{\mathrm{AlAs}} G_{\mathrm{AlAs}}^{0,s} + x_{\mathrm{GaAs}} G_{\mathrm{GaAs}}^{0,s} + RT (x_{\mathrm{AlAs}} \ln x_{\mathrm{AlAs}} + x_{\mathrm{GaAs}} \ln x_{\mathrm{GaAs}}) \\ & + x_{\mathrm{AlAs}} x_{\mathrm{GaAs}} \sum_k L_{\mathrm{AlAs,\ GaAs}}^{k,s} (x_{\mathrm{AlAs}} - x_{\mathrm{GaAs}})^k \end{aligned} \tag{A.5}$$

all relevant quantities may be found in Ref. [85].

Résumé

Ce travail examine des nanofils III-V synthétisés en mode vapeur-liquide-solide, une goutte liquide catalysant la croissance unidimensionnelle. En conjuguant expériences d'épitaxie par jets moléculaires, caractérisations structurales et analyses théoriques, j'étudie et clarifie plusieurs questions cruciales. L'une d'elles est le contrôle de la phase cristalline, qui s'avère souvent un mélange de segments cubiques et hexagonaux. Au moyen d'une analyse probabiliste de la séquence d'empilement de nanofils d'InP, je montre que la sélection de phase est déterminée non seulement par les conditions de croissance mais aussi par des interactions entre monocouches. Je souligne et discute le rôle de l'énergie de bord du germe qui médie la formation de chaque monocouche. On sait par ailleurs que le caractère abrupt des interfaces dans les hétérostructures axiales est limité par l'accumulation de matière dans la goutte (effet réservoir). J'étudie la formation de telles hétérostructures dans des nanofils de GaAs auto-catalysés en utilisant un second élément des groupes V (P) ou III (Al). Les profils compositionnels des insertions ternaires sont analysés à la résolution atomique. Les interfaces se révèlent soit plus larges (GaAsP) soit plus étroites (AlGaAs) qu'attendu et la morphologie du front de croissance dépend de la supersaturation. Je montre que, dans les deux cas, la largeur d'interface peut être réduite à quelques monocouches et je suggère d'autres améliorations. Enfin, je présente mes tentatives pour réaliser des nanofils ultraminces de GaAs et GaP et je discute du contrôle de la croissance à l'échelle d'une monocouche par réduction du caractère stochastique de la nucléation.

Abstract

This work investigates III-V nanowires synthesized via the vapor-liquid-solid method, whereby a catalyst droplet promotes one-dimensional growth. By combining molecular beam epitaxy experiments, structural characterization and theoretical analyses, I study and clarify several critical issues. One of them is the control of the crystal phase, which is frequently found to be a mix of cubic and hexagonal segments. By performing a probabilistic analysis of the stacking sequence of InP nanowires, I show that phase selection is determined not only by growth conditions but also by interactions between layers. I highlight and discuss the role of the edge energy of the nucleus that mediates the formation of each monolayer. Another important problem is the formation of axial heterostructures, which interface sharpness is severely limited by material accumulation in the droplet ('reservoir effect'). To this end, I study the formation of such heterostructures in Ga-catalyzed GaAs nanowires using either a second group V element (P) or a second group III element (Al). The composition profiles of the ternary insertions are analyzed with monolayer resolution. The interface widths are found to be larger (GaAsP) or narrower (AlGaAs) than expected, and the morphology of the growth front depends on supersaturation. In both cases, I demonstrate that the interface width can be reduced to a few monolayers and suggest further improvements. Attempts to achieve ultrathin GaAs and GaP nanowires that would permit lateral quantum confinement are presented. Finally, I consider the possibility of minimizing the stochastic character of nucleation ultimately to control the growth of single monolayers.